



Norwegian University of  
Science and Technology

# Numerical Investigation of Viscous Flow Around Two Tandem Circular Cylinders Ending on a Flat Plate

**Anette Rognaldsen**

Marine Technology

Submission date: June 2018

Supervisor: Bjørnar Pettersen, IMT

Co-supervisor: Tale E. Aasland, IMT

Norwegian University of Science and Technology  
Department of Marine Technology





## MASTER THESIS IN MARINE HYDRODYNAMICS

SPRING 2018

FOR

**Stud.techn. Anette Rognaldsen**

### **NUMERICAL INVESTIGATION OF VISCOUS FLOW AROUND TWO TANDEM CIRCULAR CYLINDERS ENDING ON A FLAT PLATE.**

The candidate shall investigate the viscous flow around two circular cylinders in a tandem configuration ending on a flat plate. (This is equivalent to a two pipe submerged tunnel ending in a vertical mountain side after the fjord crossing.) The numerical simulation tool to be used is OpenFOAM, at low Reynolds numbers.

Focus of the study shall be on the physical flow field details, especially in the flow zone between the two cylinders. Special emphasis should be on the cylinder/plate area. All the results obtained should be discussed and compared to relevant data available from the literature. Proper visualization of results are important.

The candidate's choice of flow parameters should be argued for. Computational parameters shall be investigated and documented. The proper parameters and detailed settings of the numerical simulations (including pre- and post-processing) should be documented for later use.

In the thesis the candidate shall present his personal contribution to the resolution of the problem within the scope of the thesis work. Theories and conclusions should be based on mathematical derivation and logic reasoning identifying the various steps in the deduction. The original contribution of the candidate and material taken from other sources shall be clearly defined. Work from other sources shall be properly referenced. The candidate should utilize the existing possibilities for obtaining relevant literature.

The thesis should be organized in a rational manner to give a clear exposition of results, assessments and conclusions. The text should be brief and to the point, with a clear language.

The thesis shall contain the following elements: A text defining the scope, preface, list of contents, summary, main body of thesis, conclusions with recommendations for further work, list of symbols and acronyms, references and appendices. All figures, tables and equations shall be numerated.

It is supposed that Department of Marine Technology, NTNU, can use the results freely in its research work by referring to the student's thesis.

The thesis shall be submitted June 11<sup>th</sup>, 2018, in two copies.

  
Bjørnar Pettersen  
Professor/supervisor

Co-supervisor: PhD-student Tale E. Aasland



## Abstract

Flow around cylindrical shapes are frequently seen both within the academics and for applications in ocean and marine engineering. Viscous flow around tandem cylinders fixed to a vertical wall is numerically simulated for a Reynolds number of 500. Direct Numerical Simulations with body-fitted structured hexahedron mesh using OpenFOAM have been performed. Important parameters in the simulations have been chosen based on technical specifications for the Submerged Floating Tube Bridge (SFTB) (Team, 2016) in the E39 Coastal Highway Route-project. This gives a diameter of 1 m, free stream velocity of 1 m/s and a center-to-center spacing between the cylinders of  $S/D = 4$ .

The physics of the flow around the cylinders and in the plate area have been investigated by looking at velocity- and pressure fields. These have been visualized in several ways using different figures, and interesting features have been noted and compared to similar cases wherever feasible. The flow pattern revealed many interesting features along the span of the two cylinders. The gap flow was quite affected by the horseshoe vortex forming in front of the upstream cylinder, and show clear three-dimensional effects. The horseshoe vortex was rolling up behind the upstream cylinder, disturbing the flow onto the downstream cylinder. A horseshoe-like vortex also developed in front of the downstream cylinder, suggesting some of the same characteristics. Despite having some similarities, the difference in the flow onto the two cylinders indicate that this vortex is not a horseshoe vortex. The effect of the wall is observed to be quite prominent by looking in the wake for different locations along the cylinder  $z$ -axis. A cylinder length of  $16D$  is sufficient to capture signs of this, as the wake further away from the wall has similar results as the experiments and simulations for tandem cylinders in free flow.

Viewing the pressure distributions, the effect of the wall is apparent as they are vastly different when comparing the time-averaged pressure at the junction and further out. The Strouhal number was found to be similar for both cylinder, indicating synchronized vortex shedding, which was visualized through streamlines along the span of the cylinders.

The flow picture for the upstream and downstream cylinders are entirely different, and the effect of the wall is evident. Vorticity contours show some similarity in the flow picture around each cylinder, but the streamlines reveal a different flow picture for the upstream and downstream cylinders. Some of the effects of the wall seem to disappear as one moves away from the wall. The study presented in this thesis helps to improve the understanding of flows with wake interference from having two cylinders and a wall present in the simulation. This can be very useful for future investigations of other aspects of such flows.

## Sammendrag

Strømning rundt sylindere er ofte sett i akademia og i teknologiapplikasjoner for havrom og i marin næring. Viskøs strømning rundt tandem sylindre festet på en vertikal vegg er numerisk simulert for et Reynolds tall på 500. Direkte Numeriske Simuleringer (DNS) med et strukturert heksaedersk mesh grid ved hjelp av OpenFOAM har blitt utført. Viktige parametre i simuleringene har blitt valgt basert på tekniske spesifikasjoner for en nedsenket flytende tunnel-bro (SFTB) i veiprojektet Fergefri E39. Dette har gitt en diameter på 1 m, fri innløpshastighet på 1 m/s og en senter-til-senter avstand mellom de to sylindrene på  $S/D = 4$ .

Fysikken for strømning rundt de to sylindrene og i vegg-området har blitt undersøkt ved å se på hastighets- og trykkfelt. Disse har blitt visualisert på flere måter og interessante trekk har blitt observert og sammenlignet med lignende studier. Strømningsbildet avslørte mange interessante trekk langs de to sylindrene, særlig i front av sylindren oppstrøms hvor en hesteko-virvling oppstår. Her vises klare tre-dimensjonale effekter, hvor hesteko-virvelen ruller opp bak sylindren oppstrøms og skaper dermed forstyrrelser på strømmingen mot sylindren nedstrøms. En hesteko-aktig virvel formes også i front av sylindren nedstrøms, som gir antydning av å inneha noen av de samme strømningstrekkene. Til tross for disse likhetene, er innstrømningen til de to sylindrene veldig ulik, noe som indikerer at dette ikke er en hesteko-virvling. Effekten av veggen blir tydelig om en ser på waken i ulike posisjoner langs sylindrene i z-retningen. En sylinder-lengde på  $16D$  er funnet tilstrekkelig for å fange disse effektene, mye grunnet at resultatene lengre ut på sylindrene er sammenlignbare med eksperimenter og numeriske simuleringer for tandem sylindre i fri strømning.

Trykkfordelingen over sylinder-overflatene avslører en tydelig effekt fra veggen, og er svært forskjellige når en ser nærme veggen sammenlignet med lengre ut på sylindrene. Strouhal-tallet var funnet til å være noenlunde likt for både oppstrøms og nedstrøms sylinder. Dette indikerer en parallel og synkronisert virvelavløsning, som er visualisert gjennom strømlinjer i ulike x-y-plan langs sylindrene.

Strømningsbildet for de to sylindrene er ganske ulikt hverandre, og effekten fra veggen er stor. Vortisitets-konturer viser noen likheter i form av hesteko-virvling rundt begge sylindrene, men strømlinjene avslører et helt annet strømningsbilde. Noen av effektene induisert av veggen på sylindrene ser ut til å forsvinne når en beveger seg lenger ut på sylindrene. Arbeidet som er presentert i denne masteroppgaven vil hjelpe med å forstå strømningsbildet der en har forstyrrelser på grunn av to sylindre, samt en vegg tilstede i simuleringen. Dermed kan denne masteroppgaven være nyttig for fremtidige undersøkelser ved andre aspekter av slike strømninger.

## Preface

This report is a result of the final semester of my Master's degree in Marine Technology. The thesis is written at the Institute of Marine Technology at the Norwegian University of Science and Technology in the spring of 2018. It describes the work done during the final semester with numerical simulations in OpenFOAM of tandem cylinders fixed to a wall in the lower Reynolds number regime.

The topic of the thesis was inspired by my supervisor, professor Bjørnar Pettersen, and co-supervisor, PhD. student Tale E. Aasland. The fact that this topic is not well-studied was also very appealing, and being a part of a bigger project made it very motivating as well.

The learning curve during my last year has been steep, given that I had never worked with CFD. This spring I have realized that this is a very useful procedure with many possibilities. The focus during this final year was to learn how use OpenFOAM as an utility for CFD, with both pre- and post-processing. A huge and time consuming part of this was the mesh generation. In addition, investigating the flow around the cylinders when a wall is present has been of major focus.

This work would not have been possible without help from the Marine Hydrodynamics discipline. I would thereby like to thank a few people for their help and motivating words.

Firstly, I would like to thank my supervisor, professor Bjørnar Pettersen. With his motivating words and supportive attitude, he has been an inspiration throughout my final year.

Second, I would like to thank my co-supervisor, PhD. student Tale E. Aasland, for her inspiring words and help with questions I had regarding anything related to the topic of this study.

I would also like to thank PhD. student Håkon Strandenes for his help regarding questions about OpenFOAM and post-processing in *ParaView*.

Lastly, I would like to thank the NTNU HPC Group, as this research was supported in part with computational resources at NTNU provided by NOTUR, <http://www.sigma2.no>. Without this resource, this work wouldn't have been possible.



Anette Rognaldsen

Trondheim, June 11, 2018

# Contents

<b>1</b>	<b>Introduction</b>	<b>1</b>
1.1	Motivation . . . . .	1
1.1.1	Problem at hand . . . . .	1
1.2	Outline/Structure of the thesis . . . . .	3
<b>2</b>	<b>Flow around different cylinder configurations</b>	<b>4</b>
2.1	Assumptions and limitations of the fluid flow . . . . .	4
2.2	Single cylinder in free flow . . . . .	5
2.2.1	Boundary layer . . . . .	5
2.2.2	Flow separation . . . . .	5
2.2.3	Vortex shedding and forces acting on the cylinder . . . . .	7
2.3	Two cylinders in tandem arrangement in free flow . . . . .	10
2.3.1	Classification of flow regimes . . . . .	10
2.3.2	Flow patterns . . . . .	12
2.3.3	Pressure and forces . . . . .	13
2.3.4	Drag and lift coefficients . . . . .	14
2.3.5	Strouhal number . . . . .	14
2.3.6	Three-dimensionality . . . . .	15
2.4	Cylinder fixed to a surface . . . . .	15
2.4.1	Flow patterns . . . . .	15
2.4.2	Pressure and forces . . . . .	18
2.5	Two cylinders fixed to a surface . . . . .	23
<b>3</b>	<b>Computational Fluid Dynamics</b>	<b>25</b>
3.1	Fundamental equations . . . . .	25
3.1.1	Conservation of mass . . . . .	25
3.1.2	Conservation of momentum . . . . .	26
3.2	OpenFOAM . . . . .	26
<b>4</b>	<b>Numerical set-up</b>	<b>27</b>
4.1	Computational domain and grid . . . . .	27
4.2	Boundary conditions . . . . .	28
4.3	Solver settings . . . . .	32
4.4	Visualization . . . . .	33
4.4.1	Identification of vortices . . . . .	33
4.4.2	Streamlines . . . . .	34
<b>5</b>	<b>Results</b>	<b>36</b>
5.1	Vorticity . . . . .	37
5.2	Flow pattern . . . . .	40
5.3	Pressure distribution . . . . .	49
5.4	Forces . . . . .	54



5.5	Strouhal number	56
<b>6</b>	<b>Discussion</b>	<b>60</b>
6.1	Further investigations	61
<b>7</b>	<b>Conclusion</b>	<b>63</b>
	<b>Nomenclature</b>	<b>65</b>
	<b>List of figures</b>	<b>67</b>
	<b>List of tables</b>	<b>69</b>
	<b>Bibliography</b>	<b>70</b>
<b>A</b>	<b>Visualization</b>	<b>I</b>
A.1	Single cylinder fixed to wall	I
A.2	Tandem cylinders fixed to wall	VI
<b>B</b>	<b>OpenFOAM</b>	<b>XIV</b>
B.1	controlDict	XIV
B.2	fvSchemes	XVII
B.3	fvSolution	XVIII
B.4	probes	XX

# Chapter 1

## Introduction

Flow around cylinders have been a topic of study for many decades, both within the academics and for applications in ocean and marine engineering. Cylindrical shapes can be found on offshore platforms, such as a SPAR-platform, or pipelines on the seabed and in bridge piers. The cylinder is still a highly relevant subject for different studies, as the simple shape results in a very complex wake structure, due to the many parameters and configurations possible.

Two cylinders in tandem arrangement is one of the most used configurations, and forms the basic of a case with multiple cylinders, such as risers on a rig, dual pipelines or the legs of a Tension Leg Platform (TLP). The area of application of cylinders in different structures is immense, and the different configurations will, in some way, induce flow on the upstream cylinder that is different to the one for the downstream cylinder.

### 1.1 Motivation

The E39 Coastal Highway Route is a project by the NPRA to improve the route from Kristiansand to Trondheim. Over this route, there are currently seven ferry connections, where the goal is to replace these with different types of bridges to shorten the travel time. One of these types is the so-called submerged floating tube bridge (SFTB), where the two tubes are placed underwater, either having floating pontoons, figure 1.1 or fastened to the sea bottom by tethers, figure 1.2. This type of underwater bridge has never been built before, only suggested, so it's an interesting and complex problem. The bridge tunnels will in practice consist of several sections, due to security, necessary systems and similar. From a hydrodynamic perspective, the SFTB can be simply modelled as two tandem circular cylinders, as seen in this introductory chapter. Hydrodynamic effects around two tandem cylinders in free flow are highly researched, and many results exist. However, the effect close to the vertical wall haven't been studied that well, so this will be the topic for this master's thesis.

#### 1.1.1 Problem at hand

The problem at hand is a very complex structure, and several simplifications have been made for this thesis, due to available time and computational capacity. Given the technical report for the submerged floating tunnel bridge for Bjørnafjorden (Team, 2016), many of the specifications are not followed to the point. The most important feature, is the similarity of flow in reality vs. simulated, resulting in the parameter of Reynolds number. The inflow velocity is thereby set to unity,  $U = 1$  m/s.

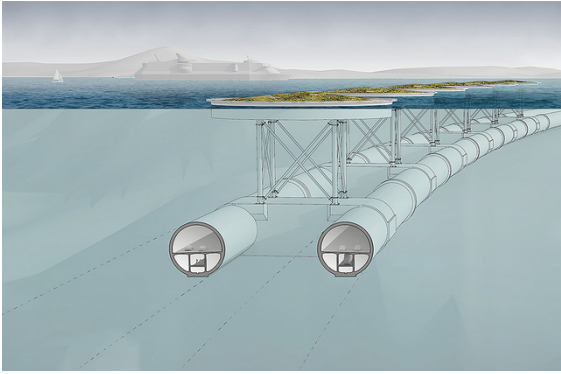


Figure 1.1: SFTB with pontoons. Illustration from Snøhetta/Statens Vegvesen

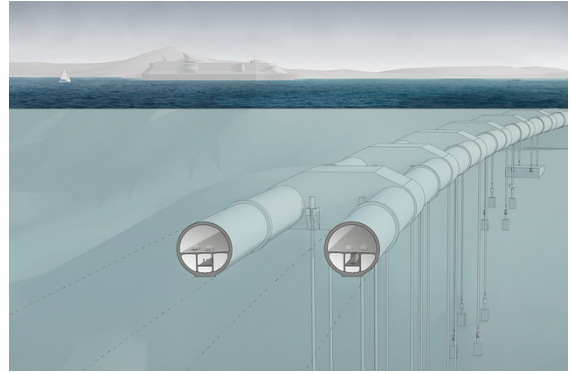


Figure 1.2: SFTB anchored by tethers. Illustration by Snøhetta/Statens Vegvesen

According to the technical report ([Team, 2016](#)), the water density in Bjørnafjord is defined with an average of  $1028 \text{ kg/m}^3$ , but in the problem at hand, the density is simplified to  $1000 \text{ kg/m}^3$ . The two tubes making the bridge structure, consists of two different tunnel profiles of different size, defined as the T9.5 and T12.5. These are placed with a spacing of 400 m in between, where the biggest section, T12.5, includes an emergency stopping lane and an emergency exit in between the two tunnels. A simplification of having two alternating sections, is to assume that there is only one type of section and no middle emergency part. This simplification is the main concern in this thesis, in addition to assuming a unity tunnel diameter of 1 m. This simplifies the simulation, and makes it easier to maintain a Reynolds number-similarity.

The spacing ratio between the two tunnels is set to be 40 m in the technical report for the SFTB. Based on the two different tunnel profiles, the smallest profile has been used as a basis, because this is the main section of the tube bridge. The outer diameter of the tube is  $10.04 \text{ m}$ , giving a spacing ratio,  $S/D$ , of approximately 4. Based on this, the spacing ratio,  $S/D$ , is chosen to be 4 in the current simulation, due to the technical report and findings from [Prsic \(2016\)](#). Wind tunnel testing show that the bridge is unaffected of inline VIV amplitudes for a spacing ratio larger than 2. Thus,  $S/D = 4$  is within the allowable range and similar to the real spacing between the two cylinders.

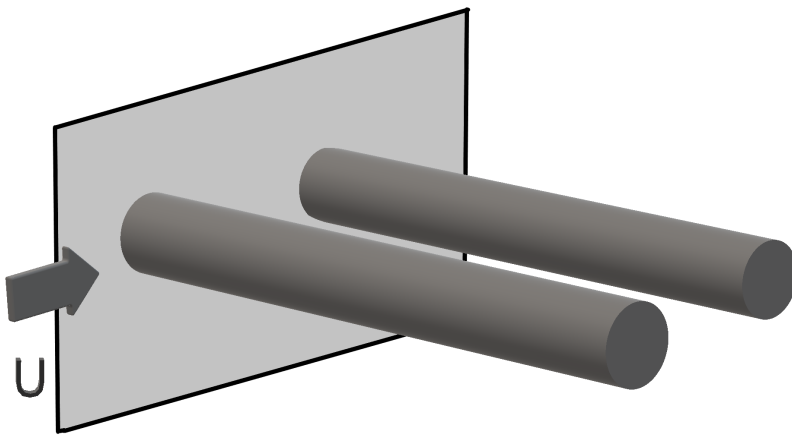


Figure 1.3: Principal sketch of tandem cylinders fixed to a vertical wall

The wall is modelling the connection point between the fjord and the landmass. In practice, the connection point between the submerged bridge and the landmass can have an incline and have quite a rough surface, but in this thesis, it is assumed firstly that the connection point is a smooth,

vertical wall. The two cylinders are also assumed to have a smooth surface, meaning there is no roughness on the surface of the cylinder.

To simplify the problem even further, the anchoring tethers/pontoons are removed. It is thereby assumed that there is no disturbance from the anchoring solution. It is also assumed that the floating tube bridge is placed adequately far away from the free surface and the bottom of the fjord, such that there are no disturbances, and the SFTB is placed in infinite fluid, except for the present wall at the end of the cylinders. A principal sketch of the two tandem cylinders are given in figure 1.3.

## 1.2 Outline/Structure of the thesis

The structure of this thesis is as follows:

**Chapter 2** gives an overview of basic theory regarding flow around a cylinder body, tandem cylinders and a literature review regarding flow past a cylinder fixed to a wall.

In **Chapter 3** some of the most fundamental equations in CFD are provided.

**Chapter 4** describes the numerical set-up of the study, where the domain and boundary conditions will be discussed.

**Chapter 5** presents the results obtained during the simulation of tandem cylinders fixed to a wall at  $Re = 500$ . This includes the vorticity distribution, flow pattern and how the forces and pressure act around the cylinders, and also the Strouhal number variation.

**Chapter 6** contains a discussion of the main results obtained in the present study, compared to literature regarding topics of similar art.

A conclusion is given in **chapter 7**.

## Chapter 2

# Flow around different cylinder configurations

### 2.1 Assumptions and limitations of the fluid flow

A fluid flow is described as a moving fluid. For these problems, assumptions and limitations have to be defined to make the problem easier. First, all body-forces in the domain are neglected, such that gravity is not taken into consideration.

The fluid is also classified as a single-component fluid, which is characterized by being the simplest one-component fluid, and is in equilibrium with its hydrostatic pressure.

The fluid is assumed to be Newtonian, which implies that the fluid can obtain friction and shear stresses when the fluid acts against a solid surface or on another fluid. The shear stress leads to deformation, and if the deformation rate is linearly proportional to the shear stress, the fluid is defined as Newtonian ([Cimbala and Cengel, 2013](#)).

A fluid flow can be described based on the chaos in the fluid, or by the non-dimensional number, Reynolds number. Reynolds number is defined as the ratio of inertial forces to viscous forces, given by the parameters *inflow velocity*, *fluid density* and *viscosity*, see equation 3.1. Laminar flow is described as flow in a stable and well-ordered state. The fluid particles appear to move along each other, in contrast to a turbulent flow where there is no form of stability in the movement of fluid particles. Transient flow is defined as the flow state between laminar and turbulent. The analysis of the fluid dynamic problems are solved while assuming the flow to be laminar.

## 2.2 Single cylinder in free flow

Flow around a bluff body, in this case a circular cylinder, has been an object of study for many years. One of the interesting phenomena occurring is the disturbed region behind the body. Potential theory was developed to describe the flow, assuming that the flow is inviscid, irrotational and incompressible. This simplification is not applicable with the fluid being water, as the viscous forces will cause the fluid particles to rotate, such that the fluid can't be inviscid or irrotational. Near the body, a boundary layer will appear, and at high Reynolds numbers, potential theory can be considered valid, due to small viscous forces. In the regions near the boundary layer, where the velocity gradient is large, potential theory is not applicable. However, with the complexity of the flow around different shapes, the flow cannot be considered irrotational or inviscid to get a realistic view of the flow. The vorticity and the viscous forces have major impact on the flow structure.

### 2.2.1 Boundary layer

The boundary layer is a very important concept within fluid dynamics, and refers to a layer of moving fluid being in close vicinity of a surface. This layer makes it impossible to apply potential theory to such a flow problem, so neither the simplified Euler or Bernoulli equations can be used due to the viscous forces present. They are characterized by high shear with the highest velocities away from the surface. Frictional force, viscous stress, and vorticity occur in the boundary layers. A thin boundary layer should exist for large Reynolds numbers, but the magnitude is dependent on the geometry of the fixed body.

The velocity cannot make sudden changes, and the velocity on the cylinder surface equals the velocity of the cylinder body. This means the change in velocity must be gradual at some distance from the cylinder. The thickness of the boundary layer is defined as the distance from the cylinder surface where the horizontal velocity becomes equal to 99% of the free-stream velocity, such that the boundary layer thickness is referred to as  $\delta_{0.01}$ .

The order of magnitude of the boundary layer thickness is  $O\left(\frac{1}{\sqrt{Re}}\right)$ , and it is roughly calculated as following:

$$\delta = \frac{D}{\sqrt{Re}}. \quad (2.1)$$

As seen in figure 2.1, the velocity profiles in the boundary layer over the cylinder surface is not equal all the way. Four profiles are given at different points on the cylinder surface, and this also means the boundary layer thickness changes over the surface, as can be seen by the red line in figure 2.1. It is clear that the velocity gradient is largest closer to the surface, and by having such a gradient implies that the flow in the boundary layer is viscous (White, 2005).

### 2.2.2 Flow separation

Flow separation can easily be explained as the point where the flow leaves the surface of the body. There are no sharp edges for flow separation like there are for square cylindrical structures. So, for circular cylinders, the separation points can move as the fluid changes.

Pressure is very closely linked to separation, and in potential flow, the pressure gradient is negative and decreasing over the first half of the cylinder, as seen in figure 2.2. This is because the fluid is accelerating to get past the thicker part of the cylinder, while for the second half, the pressure increases and velocity decreases. In real fluid, however, there will be some kinetic energy loss over the first half, while the second half will experience that the kinetic energy of the fluid particles is

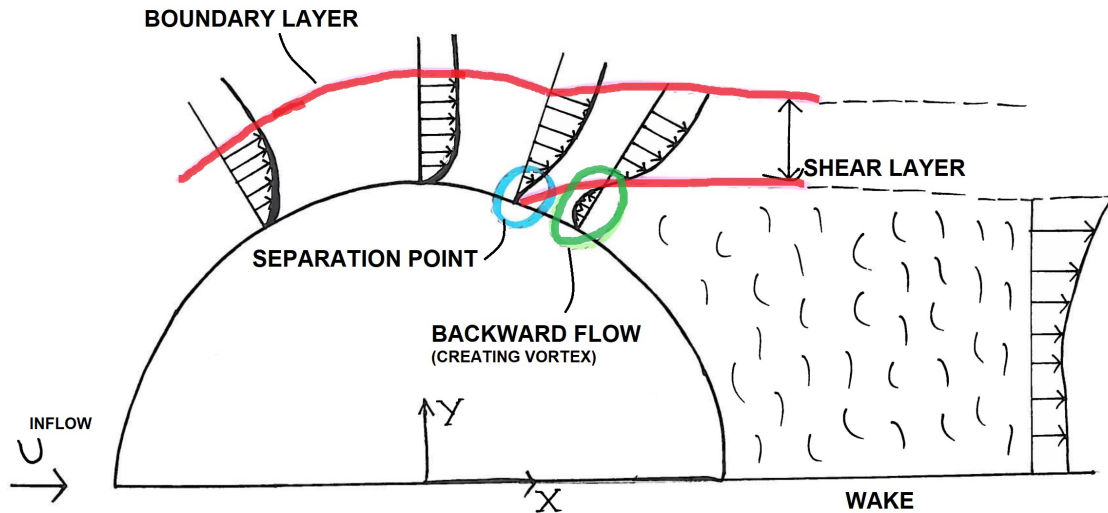


Figure 2.1: Principle sketch of separation of flow around a cylinder.

too small to overcome the pressure increase. The fluid particles thereby stop to move, and this effect is strongest closest to the surface of the cylinder, where the velocity gradient and friction has the largest value. Due to external pressure, the fluid particles will start to move in the opposite direction, causing the phenomenon backflow, as illustrated in figure 2.1 by the green circle. The velocity gradient will be less than zero,  $\frac{\partial u}{\partial y} < 0$ , and vortices start to form behind the cylinder caused by the backflow (Pettersen, 2014).

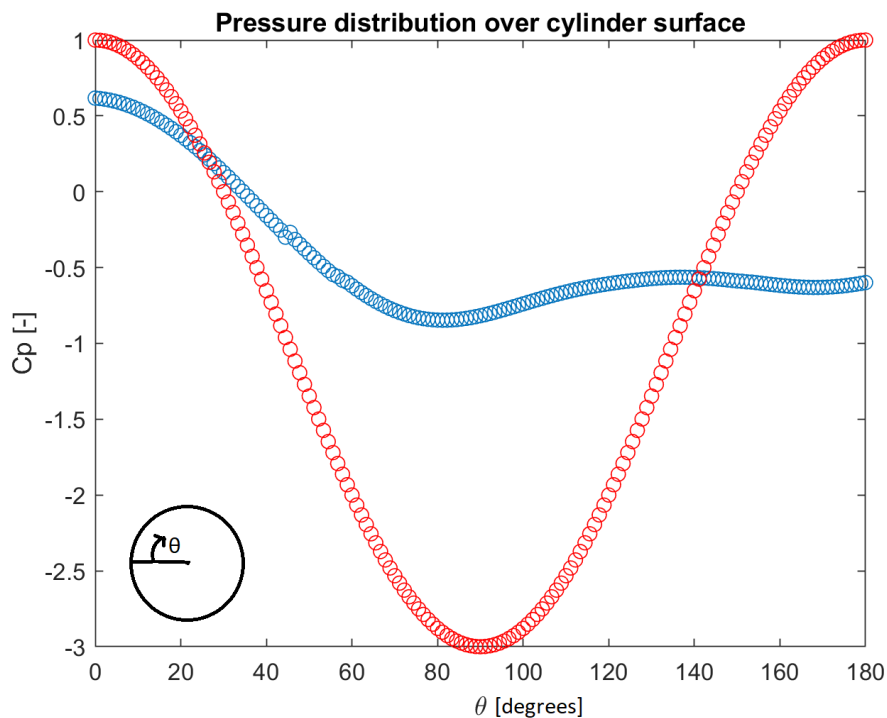


Figure 2.2: Pressure over the cylinder surface for potential and real flow. The real flow has  $Re = 100$ . Blue line: real flow. Red line: potential flow.

As seen by the blue circle in figure 2.1, the separation point is located in front of the backflow

point, where the velocity gradient  $\frac{\partial u}{\partial y} = 0$ , or the shear force  $\tau_w = \mu \frac{\partial u}{\partial y} = 0$ . This point lies where the pressure coefficient flattens out for a real flow, see figure 2.2. The potential flow won't have a separation point due to its symmetric pressure distribution, which is in good agreement with the assumption of irrotational flow and no kinetic energy loss.

If  $\frac{dp}{dx} < 0$ , a negative pressure gradient or favourable pressure gradient is present, meaning that the flow is enabled. The velocity profile representing this state, is presented in figure 2.3 by  $\theta = 60^\circ$ . An adverse pressure gradient is mathematically written as  $\frac{dp}{dx} > 0$ , meaning that the pressure now enforces the breaking of the boundary layer and the separation of flow that occurs when the velocity slows down and starts reversing. Such a pressure gradient is presented by the velocity profile for  $\theta = 130^\circ$  in figure 2.3. This means that between 100 and 130 degrees, a separation point will exist, according to figure 2.1.

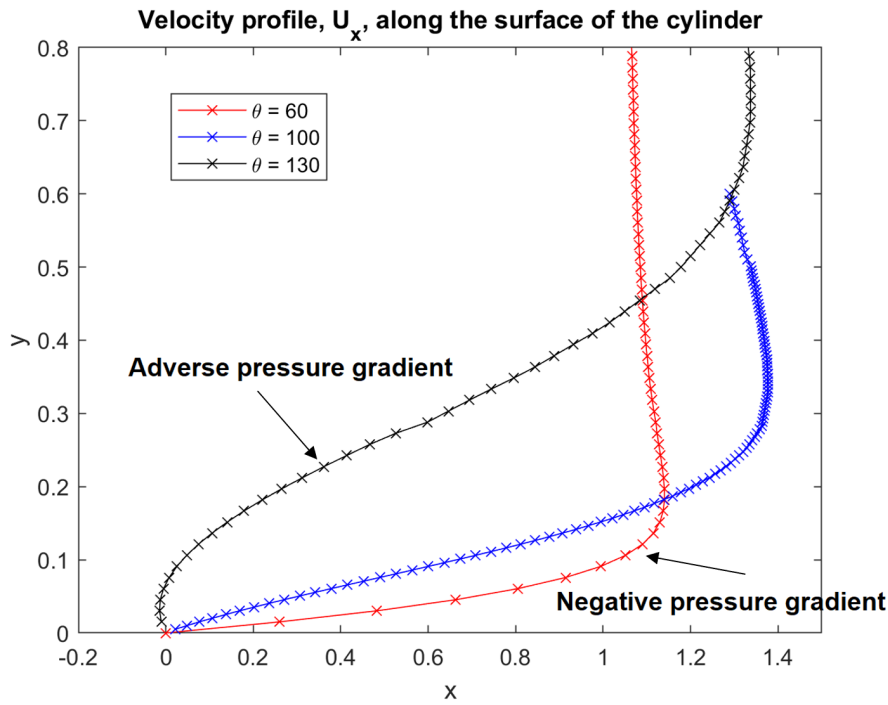


Figure 2.3: Velocity profiles over the cylinder surface, at 3 locations for  $Re = 100$ .  $\theta$  given in degrees.

The location of the separation point, is highly dependent on the Reynolds number. With higher  $Re$  and turbulent flow, the separation point will be located further back than for laminar flow. This causes the wake to be narrower for turbulent flows.

### 2.2.3 Vortex shedding and forces acting on the cylinder

Vortex shedding is a phenomenon that occurs when the Reynolds number is about 48 or higher, and is a common feature for all flow regimes. Figure 2.4 show how a fluid flow will deform when passing a fixed circular cross-section, and it also presents how the flow is disturbed and the dependence on Reynolds number with respect to vortex shedding.

At  $Re \leq 40$  a pair of vortices are formed in the near wake of the cylinder and stays there, see figure 2.4. When the Reynolds number increase, the vortices start to shed alternately from each side of the cylinder as the wake becomes more and more unstable. This instability cause oscillating forces, due to the alternating shedding of vortices from the cylinder. The lift will act in the cross-flow direction and oscillates harmonically through zero. The drag force will act with the flow direction



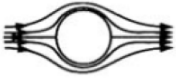



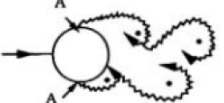
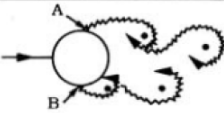
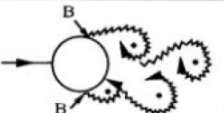
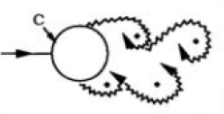
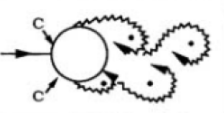
	No separation. Creeping flow	$Re < 5$
	A fixed pair of symmetric vortices	$5 < Re < 40$
	Laminar vortex street	$40 < Re < 200$
	Transition to turbulence in the wake	$200 < Re < 300$
	Wake completely turbulent. A: Laminar boundary layer separation	$300 < Re < 3 \times 10^5$ Subcritical
	A: Laminar boundary layer separation B: Turbulent boundary layer separation; but boundary layer laminar	$3 \times 10^5 < Re < 3.5 \times 10^5$ Critical (Lower transition)
	B: Turbulent boundary layer separation; the boundary layer partly laminar partly turbulent	$3.5 \times 10^5 < Re < 1.5 \times 10^6$ Supercritical
	C: Boundary layer com- pletely turbulent at one side	$1.5 \times 10^6 < Re < 4 \times 10^6$ Upper transition
	C: Boundary layer com- pletely turbulent at two sides	$4 \times 10^6 < Re$ Transcritical

Figure 2.4: Vortex Shedding phenomenon, collected from [Sumer and Fredsøe \(2006\)](#)

and oscillates at twice the frequency, as seen in figure 2.5. The drag and lift forces are obtained by integrating the pressure over the cylinder surface, and because the pressure acts normal to the surface, the force is decomposed into a horizontal (drag) and vertical (lift) component. The two coefficients are defined as:

$$C_D = \frac{F_x}{\frac{1}{2}\rho U^2 A_{ref}}, \quad (2.2)$$

$$C_L = \frac{F_y}{\frac{1}{2}\rho U^2 A_{ref}} \quad (2.3)$$

where  $\rho$  is the density,  $U$  is the inflow velocity,  $A_{ref}$  is a characteristic area (often diameter  $D$  times a length for a circular cylinder),  $F_x$  and  $F_y$  are the forces in drag- and lift-direction, respectively ([Faltinsen, 1998](#)).

The vortex shedding will at a time instant 0, illustrated by *a*) in figure 2.6, have a vortex that is being cut off by a second vortex, i.e. B in the figure. Vortex A will then be free to travel downstream, where a clockwise circulation around the cylinder is created. A third vortex, C, will

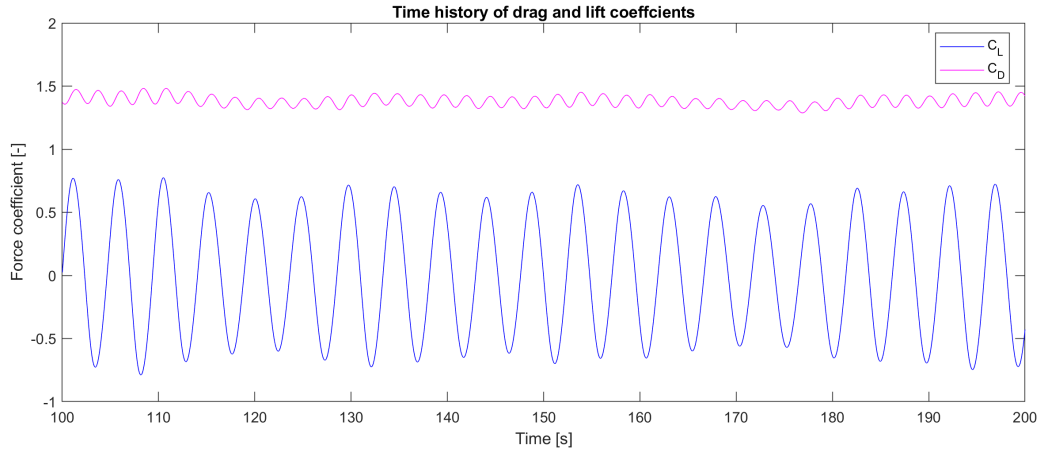


Figure 2.5: Time history of lift and drag coefficients for  $Re = 300$ . Pink line:  $C_D$ . Blue line:  $C_L$ .

form where the first vortex took place, and it will cut off vortex B at a time instant 1, illustrated by *b*) in the figure below. Vortex B will then travel downstream and cause a counter-clockwise circulation. This process will continue in an alternating manner, as mentioned above.

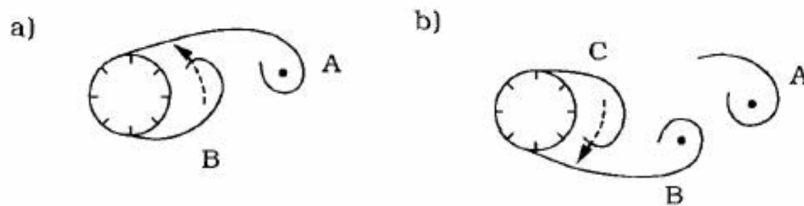


Figure 2.6: Vortex shedding from a cylinder (Sumer and Fredsøe, 2006)

Vortex shedding can be measured in vortex shedding frequency  $f_v$ , which is expressed to be dimensionless with Strouhal number, given in equation 2.4, where also the inflow velocity  $U$  and a characteristic length,  $D$  are variables.

$$St = \frac{L f_v}{U} = \frac{D f_v}{U} \quad (2.4)$$

The wake flow depends on the regime of Reynolds number, where instabilities occur from a fairly low  $Re$ . The development of wake turbulence is starting with the formation of primary Kármán vortices, as mentioned earlier. Further, Williamson (1996) reported two different small-scale streamwise vortex structures in the wake transition regime, where  $Re$  is in the range  $\sim 190 - 260$ . These instabilities are called modes A and B, where mode A represents so-called vortex loops and mode B represents streamwise vortex pairs. Next, large-scale 3D structures appear, known as vortex dislocations, due to vortices sticking to the cylinder over many shedding periods. For higher Reynolds numbers  $> 1000$ , shear-layer instability vortices develops. Aarnes et al. (2018) observed the first three-dimensional effects developing in wake for laminar free-stream flow at critical Reynolds number 190. These three-dimensional effects were recognized as mode A instabilities. In the upper Reynolds number part of the transition-in-wake regime, mode B instability modes are dominant in the wake. For turbulent free-stream flow, the mode A instabilities are stimulated, resulting in a mixed instability of both A and B for  $Re \geq 250$ .

By Floquet stability analysis, Barkley and Henderson (1996) could identify the start of the transition from two-dimensional to three-dimensional instabilities at  $Re_c \approx 189$ . The critical Floquet

mode found in the study, corresponds to the mode A instability. They dominate the flow features in the spanwise direction in the first part of the transition-in-wake regime, in addition to spot-like vortex dislocations. These dislocations were observed by [Aarnes et al. \(2018\)](#) for a laminar free-stream flow at  $Re = 350$ .

In the Reynolds number range from 100 to 300, the vortex shedding of a cylinder changes from a laminar 2D regime ( $Re < 190$ ), to a 3D wake transition regime ( $Re > 190$ ) with two different vortex shedding modes mentioned by [Williamson \(1996\)](#). Mode B is shown at  $Re = 300$  in [figure 2.7](#).

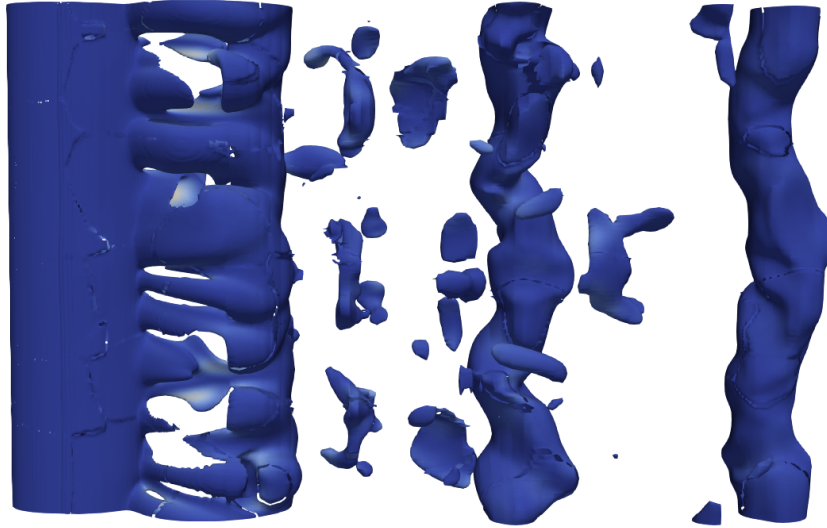


Figure 2.7: Iso-surfaces of z-vorticity ( $\omega_z$ ) at  $Re = 300$

## 2.3 Two cylinders in tandem arrangement in free flow

The tandem configuration of two cylinders has been of huge relevance for the study of flow around different bodies, such as bridge piers, pipelines, and now flow around a submerged tunnel bridge. When a cylinder is placed in the vicinity of another cylinder, it causes great effects on the flow, depending on the gap spacing, Reynolds number, and so on. The interference in the flow between these two cylinders can cause significant changes in flow patterns, vortex shedding and how the forces are acting on each of the cylinders ([Zdravkovich, 2003](#)).

### 2.3.1 Classification of flow regimes

In connection with the three main configurations of two cylinders, these can also be associated with different interference flow regions. [Zdravkovich \(2003\)](#) gives the following basic interference regions for tandem cylinders below, which is also illustrated in a more general manner for all configurations in [figure 2.8](#), where the lower, right region is valid for tandem arrangement. Hence, tandem cylinders are located in the wake interference region (W) and the combined proximity and wake interference region (P+W), see [figure 2.8](#). There are basically two kinds of wake interference: with and without eddy shedding behind the upstream cylinder, but there are some subdivisions according to [Zdravkovich \(2003\)](#):

- W-T1: There is no reattachment in the spacing ratio range of  $1 < S/D < 1.1 - 1.3$ . The free shear layer that separate from the upstream cylinder does not reattach to the downstream one. The eddies will separate as the two cylinders were one body.

- W-T2: This region contains of three different reattachment regimes in the range of  $1.1 - 1.3 < S/D < 3.5 - 3.8$ . The free shear layer may now reattach either *alternately*, *permanently*, or *intermittently*, where the eddy shedding only happens behind the downstream cylinder, in the (P+W)-region.
- W-T(1 or 2): This is the bistable regime (B1), with the range of  $3.0 < S/D < 4.0$ . Here, an intermittent change-over takes place with or without eddy shedding from the upstream cylinder.
- W-T(1+2): This is called the coupled eddy shedding regime, with a range of  $3.8 < S/D < 5 - 6$ . Two eddy streets are synchronized in both frequency and phase, which means that the eddies upstream pairs with the downstream ones and form a so called binary eddy street.
- W-T(1,2): The uncoupled eddy shedding regime behind both cylinders is valid for  $S/D > 5 - 6$ .

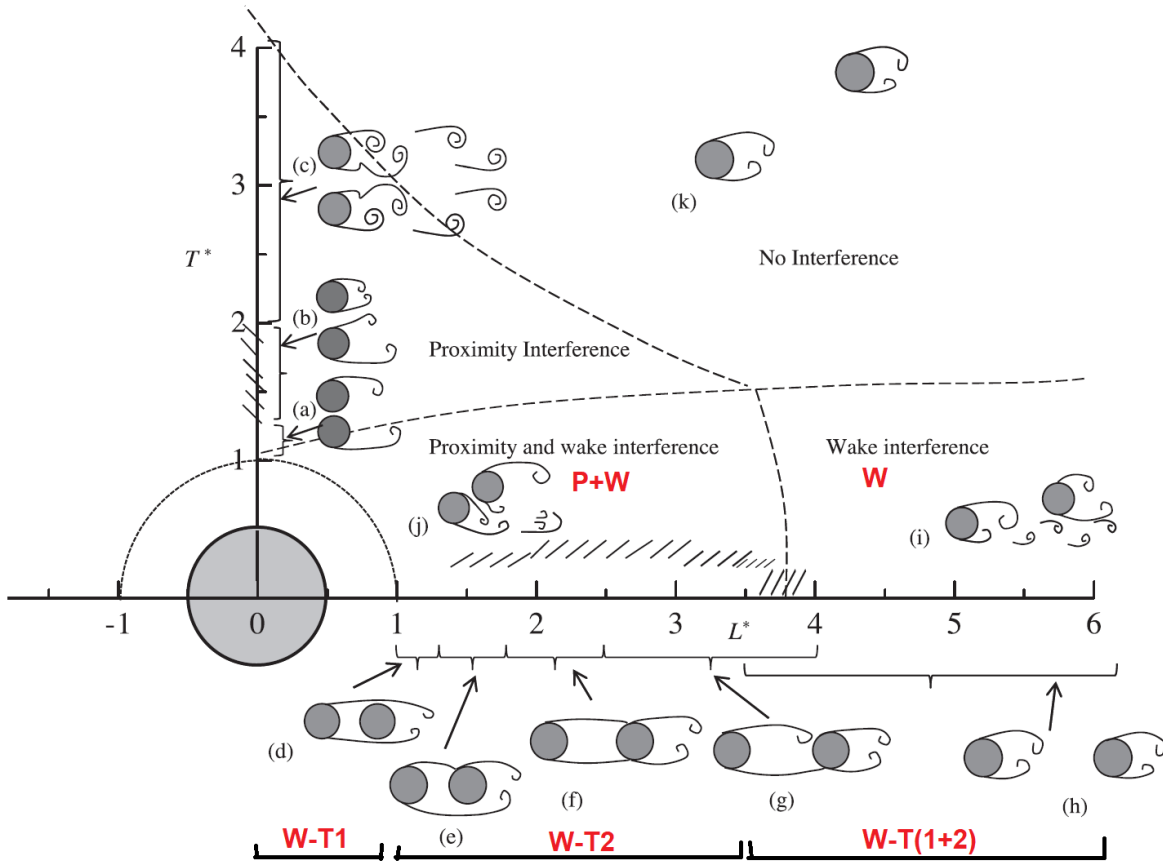


Figure 2.8: Interference of flow regions based on Zdravkovich (2003), where  $L^*$ ,  $T^*$  denotes the streamwise ( $L/D$ ) and transverse ( $T/D$ ) separations between the cylinders. Modified and collected from Zhou and Mahbub Alam (2016)

### 2.3.2 Flow patterns

The flow around two cylinders is very sensitive with respect to Reynolds number, but also the spacing between them, denoted by the spacing ratio  $L/D$  or  $S/D$ . One of the first to study the tandem configuration with regard to flow patterns was Igarashi (1981), where eight different patterns were identified, as shown in figures 2.9 and 2.10.

The flow patterns are defined as following;

(A): Separated shear layer doesn't reattach, acts as a single body,

(B): Vortex formation of the shear layer and vortex shedding in the near wake of the downstream cylinder, and reattachment of the other shear layer onto the downstream cylinder is synchronized.

(C): Quasi-stationary vortices are formed between the cylinders,

(D): The quasi-stationary vortices become unstable and the vortex shedding is detected intermittently,

(E): The separated shear layer from the upstream cylinder rolls up intermittently for a moment in front of the downstream cylinder. This is a bistable flow between D and F,

(E'): A bistable flow whose one pattern continues for a long time is predominant,

(F): The separated shear layer from the upstream cylinder rolls up in front of the downstream cylinder, and

(G): An unstable flow in the transition region, with a pattern in between the patterns A, B and C in figure 2.10 (Igarashi, 1981).

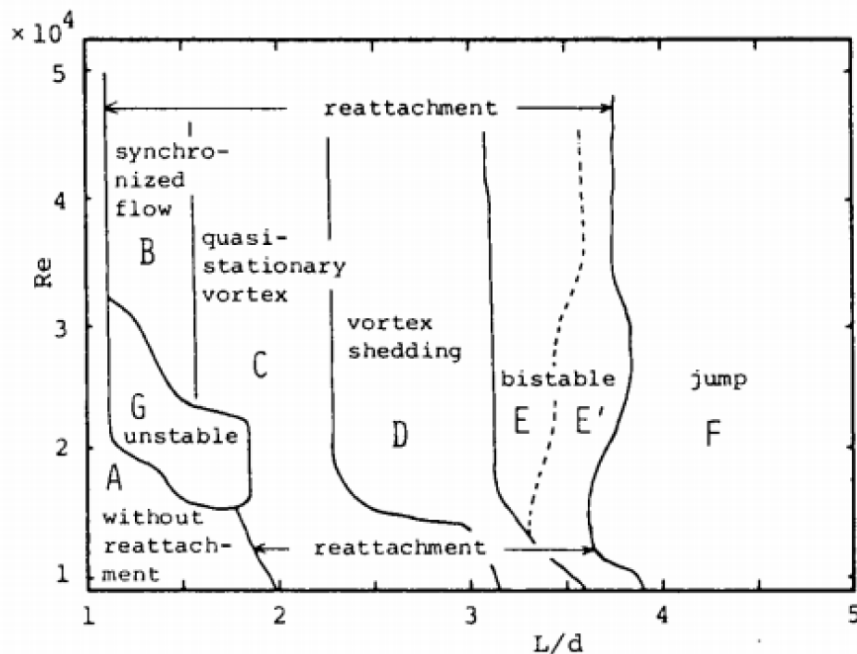


Figure 2.9: Classification of flow patterns, collected from Igarashi (1981).

Cao and Wan (2010) observed that for  $Re < 190$ , there is a laminar vortex regime and thereby no three-dimensional structures. The streamwise spacing ratio, the distance between the two cylinders, have a significant role in how the vortex shedding develops. It is observed that for streamwise spacings,  $T \geq 3$ , three-dimensional structures starts to appear as the Reynolds number increase from  $Re = 190$ . For the lower range of spacings,  $T = 3 - 3.5$ , mode A vortex shedding is observed for  $240 < Re < 300$ . Mode B can be observed at a spacing of  $T = 5$ , while at  $T = 4$  both mode A and B can be observed.

The wake flow is the main concern in the review article by Zhou and Mahbub Alam (2016), where

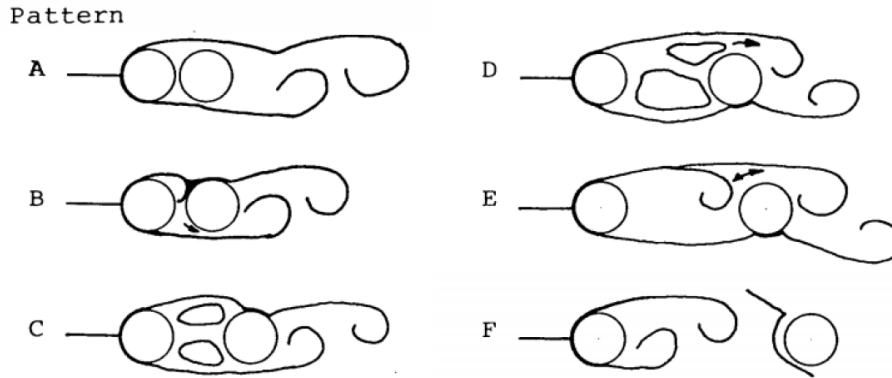


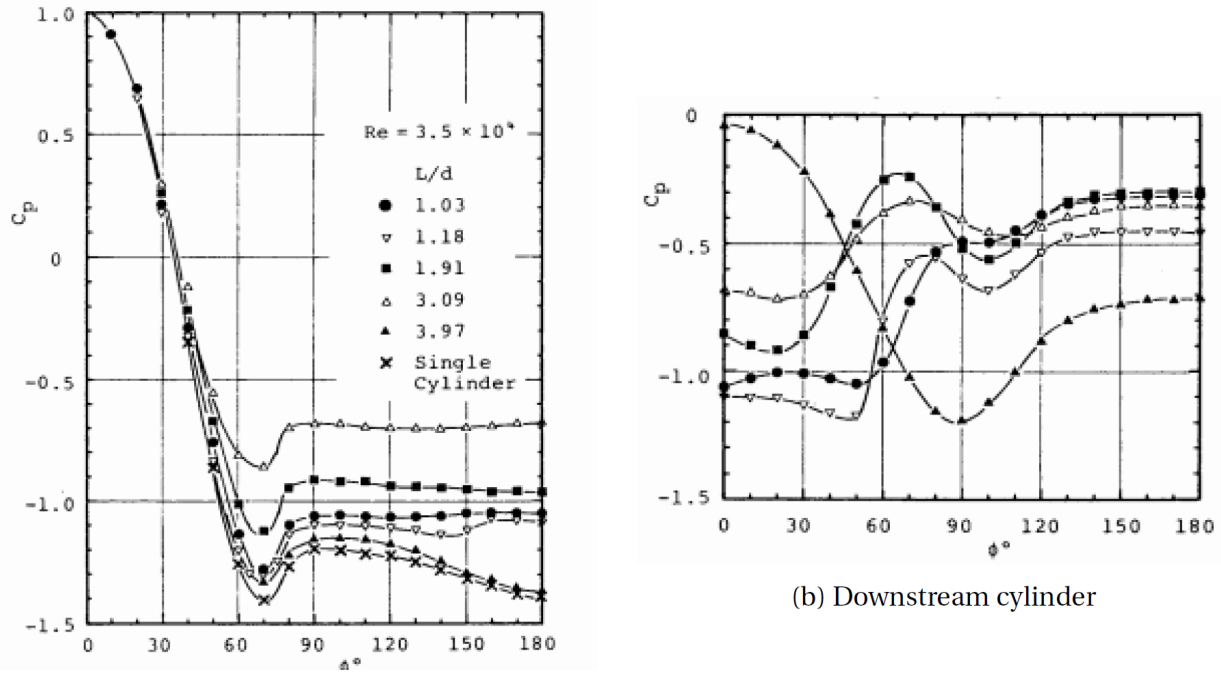
Figure 2.10: Sketches of flow patterns. First published by [Igarashi \(1981\)](#), here collected from [Summer \(2010\)](#).

an extensive review over articles concerning wake flow has been conducted. The wake behind two cylinders is highly complicated and the flow pattern highly depend on the gap spacing, according to [Igarashi \(1981\)](#). The wake flow has been investigated by many, i.e. [Kondo and Matsukuma \(2005\)](#), [Zhang and Melbourne \(1992\)](#), [Kitagawa and Ohta \(2008\)](#) and [Vakil and Green \(2013\)](#). The main findings coincides well with [Igarashi \(1981\)](#) classification from 1981, where [Vakil and Green \(2013\)](#) observed that the separation of flow increases with increasing  $Re$ , and occurs in the gap between the two cylinders. At higher  $Re$ , the cylinders will act as a single cylinder, but at lower Reynolds number, the flow remains attached at the rear of the downstream cylinder. The spacing ratio is, as mentioned, very important, and [Kitagawa and Ohta \(2008\)](#) observed that vortices were shed only from the downstream cylinder for a spacing ratio of less than 3.25, which agrees well with regime (A)-(B) in figure 2.10, where the shear layers on both sides of the upstream cylinder reattach alternately to the downstream cylinder. At larger spacings, the vortex shedding occurs in the wake of both cylinders, in good agreement with the classification of flow patterns from earlier. For more turbulent flows and with increasing turbulence intensity, [Zhang and Melbourne \(1992\)](#) observed that the vortex shedding in the wake was weakened and disorganized.

### 2.3.3 Pressure and forces

The pressure distributions around the two tandem cylinders reveal a lot of information about the flow picture, and will differ from the single cylinder as both dependence on Reynolds number and spacing between the cylinders will have a significant effect. [Igarashi \(1981\)](#) did an extensive research regarding the pressure distribution for different spacings around tandem cylinders. Figure 2.11 show the pressure distributions for the upstream and downstream cylinder in the tandem configuration. From the upstream cylinder, it is clear that the stagnation point (at  $0^\circ$ ) show a positive  $C_p$ . The trend show further a favourable pressure gradient, which changes to an adverse pressure gradient at about  $70^\circ$ . Small spacings results in a more flat curve, while the base pressures are equivalent to the gap pressure coefficient for the downstream cylinder. For the downstream cylinder, it is seen that for spacing's up to the critical one of 3.5,  $C_p$  has a negative value, while the maximas are placed at the reattachment and the separation points. The smallest spacing ratio show no reattachment peak, so in this case, the two cylinders act as a single body. The trends mentioned here are in good agreement with [Zdravkovich \(2003\)](#) findings for different types of pressure coefficient distributions.

Although investing a tandem arrangement with lower  $Re$ , the results for pressure coefficients found by [Vu et al. \(2016\)](#) suits well with the distributions described by [Igarashi \(1981\)](#).



(a) Upstream cylinder

(b) Downstream cylinder

Figure 2.11: Distribution of pressure from Igarashi (1981)

### 2.3.4 Drag and lift coefficients

Both Vakil and Green (2013) and Kondo and Matsukuma (2005) found their results to be consistent with the experimental data from Igarashi (1981) in figure 2.11. The drag force of the downstream cylinder was observed to respond slowly to the change of gap distance, compared to the upstream cylinder, and it is also seen that for two-dimensional analysis, a spacing ratio  $S/D \geq 2.5$ , the vortex shedding has a strong influence on the amplitudes of the lift and drag coefficients.

For spacings larger than the critical spacing of 3.25, Kitagawa and Ohta (2008) observed that the fluctuating lift and drag, as well as the pressure, were larger than the experimental data used to compare with. These differences were explained by the difference in aspect ratio.

Comparing the drag coefficients of the cylinders with the drag coefficients of a single cylinder at  $Re$  60-1000, Vu et al. (2016) states that the upstream cylinder become an isolated single cylinder at  $L/D = 14$ . The downstream cylinder needs a larger spacing ratio to avoid the influence of the upstream cylinder. At a certain distance between the cylinders, the drag coefficients of both change suddenly, while for other distances, a linear variation between the drag and distance is observed.

### 2.3.5 Strouhal number

The variation of Strouhal number found by Carmo and Meneghini (2006), show the effect of the wake interference. For all tested cases the Strouhal number for the upstream and downstream cylinder were the same. Kitagawa and Ohta (2008) on the other hand, as well as Igarashi (1981), observed two different peaks in the power spectrum of  $C_L$  at Strouhal number 0.155 and 0.165, for a spacing  $L/D = 3$ . For lower spacings, the  $St$  value decreases gradually as the  $L/D$  value is increased, while for increasing  $L/D$ -ratio, the Strouhal number also increases to a value of 0.189. This is in good agreement with the observations done by Igarashi (1981). Igarashi (1981) mention

that the Strouhal number is dependent of Reynolds number in a certain range of  $L/D$ -ratio. Up to the critical spacing the Strouhal number was found to be constant at 0.15, while in the range  $3.09 \leq L/D \leq 3.53$ , two different Strouhal numbers exist. This is due to the intermittent jump phenomenon and the vortex shedding from the upstream cylinder. [Kalvig \(2015\)](#) reported a Strouhal number of the lift-coefficient for the upstream and downstream cylinders of 0.195 and 0.1928, respectively, supporting the theory regarding the co-shedding regime.

### 2.3.6 Three-dimensionality

When the flow has a Reynolds number of over 190 for a single cylinder, three-dimensional effects are present. [Papaioannou et al. \(2006\)](#) argues that for tandem cylinders, the flow picture is visualized in a satisfactory way in 2D, but it over-predicts the drag coefficient of the upstream cylinder, while it under-predicts at the downward cylinder. There were observed large errors in the predicting of the forces and vortex shedding frequency. Hence, it is important to take the 3D effect into account, as the flow varies over the length of the cylinder. [Kondo and Matsukuma \(2005\)](#) found that the critical spacing ratio for two circular cylinders were quite different, with  $S/D = 3.5 - 4$  for 3D, and  $S/D = 2 - 2.5$  for 2D. To achieve a more accurate computation, the three-dimensional effect are very important to consider. Also [Carmo and Meneghini \(2006\)](#) argues that for  $Re > 190$ , the three-dimensional effects are significant and the forces acting on the cylinder are altered in two-dimensional computations. A three-dimensional simulation is necessary to calculate these forces accurately. They also argue that it is not sufficient to run 2D analyses, as the prediction of the  $(Re, l_{cc})$  pair of drag inversion becomes incorrect.

## 2.4 Cylinder fixed to a surface

The flow around a circular cylinder fixed to a vertical wall has not been extensively studied over the years. Similar studies, where the cylinder is fixed to a horizontal surface, are more thoroughly researched, and if the free surface effect of a submerged cylinder is disregarded, the two problems can be considered equal. However, the problem differs from a cylinder in free flow, and extra considerations need to be made. The flow behaviour is depending on a number of variables, but when introducing a wall, additional parameters governing the fluid are the cylinder aspect ratio and the properties of the boundary layer on the plate ([Sumner, 2010](#)).

Over the last decade or so, more and more articles have been published, both experimental and numerical, regarding finite height cylinders ([Fröhlich and Rodi, 2004](#)), bridge piers ([Roulund et al., 2005](#)), end-wall effects ([Huang et al., 2011](#)), and even junction flow around a NACA wing-profile ([Paciocchi et al., 2005](#)). This shows how important it is to investigate the flow near a cylinder fixed to a wall.

### 2.4.1 Flow patterns

Introducing a surface, in which the cylinder is mounted to, will have some effects on the flow pattern. This obviously depends on a range of parameters, where the Reynolds number is the most important in this thesis. When introducing a wall at the end of a cylinder, a boundary layer will be present, as well as along the surface of the cylinder.

Flow around an obstacle, such as a cylinder, will produce a pressure distribution, as mentioned in chapter 2.2.2. These pressure gradients that appear around an obstacle or cylinder in this case, produce a 3D separation with horseshoe vortices that wrap around the obstacle ([Simpson, 2001](#)). The horseshoe vortex system is the most significant effect on the flow pattern when introducing a fixed surface to the problem. Instead of having alternating von Kármán vortices, a horseshoe



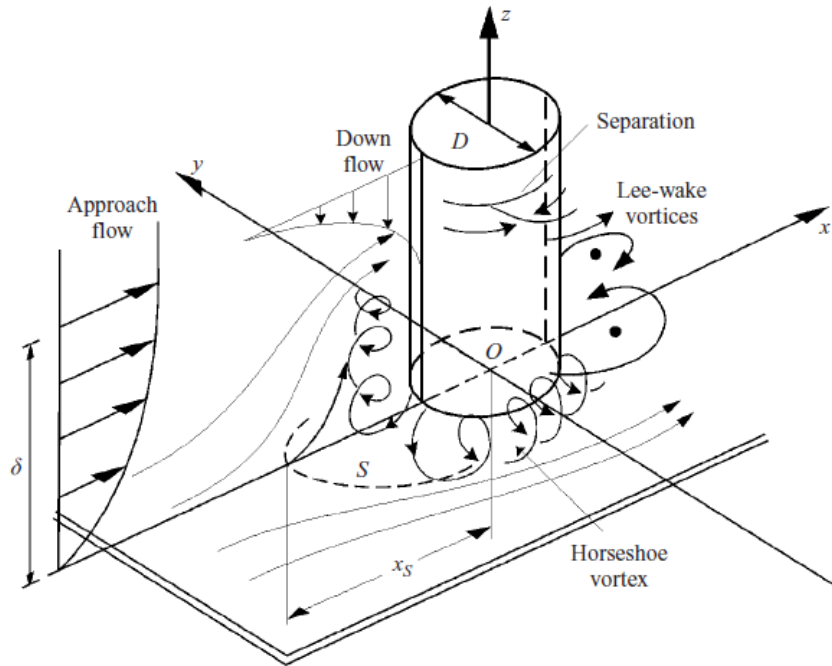


Figure 2.12: Definition of flow around a circular cylinder placed on a bed in steady current. Collected from [Roulund et al. \(2005\)](#).

vortex is formed in front of the cylinder, and vortex shedding is formed downstream, at the leeward side. Figure 2.12 shows how the flow will change when a vertical circular pile is placed on a flat plate in steady current. The horseshoe vortex system is the result from a boundary layer interacting with the flow past a body fixed to a flat surface, where the body induces a separation of the upstream flow, and the trailing vortex that forms in the wake has a similar shape as a horseshoe. [Marakkos and Turner \(2006\)](#) argues that the streamlines migrate towards the end-wall junction due to the low static pressure at the junction. In turn, this also illustrates how the circulation associated with the horseshoe vortex system originates, where the flow first turns towards the wall before it reverses and moves upstream. It can also be seen in figure 2.12 that the streamlines contract at the sides, and thereby have a smaller range to get past the cylinder. This figure is also similar to figure 1 in the article written by [Satpathy et al. \(2011\)](#), where a trailing vortex is formed at the top due to the cylinder being of finite height, and hence, it is not clear if the unsteady wake characteristics is able to stabilize the flow at low  $Re$ . 3D streamlines at different heights of a cylinder with high aspect ratio are present in the article by [Satpathy et al. \(2011\)](#), and seems to be in good agreement with the theory presented by [Roulund et al. \(2005\)](#) in figure 2.12. [Visbal \(1991\)](#) only looked at one symmetric half of the juncture in his numerical analysis, meaning that no asymmetric instabilities would be present. Up to three different primary, steady vortices were calculated for low Reynolds numbers, where a single primary vortex was present at  $Re = 500$ , two steady primary vortices at  $Re = 1500$  and lastly, three steady primary vortices for  $Re = 2600$ . For higher Reynolds numbers the computed flow topology evolved to multiple unsteady and periodic horseshoe vortices.

Figure 2.13 shows the instantaneous iso-surfaces for  $\lambda_2 = 1$  at a Reynolds number of 500. As an illustration, it shows the location of the horseshoe vortex (HSV) in front of the cylinder, which wraps around the cylinder. In the wake, an upflow is present, and the shear layer separating from the cylinder rolls up into a vortical structure (VS), before turning into a vortex street in the wake.

Figure 2.14 shows  $\omega_z$  for a cylinder with length  $16D$  at Reynolds number 500. Comparing figures 2.14a and 2.14b, it is clear that the vortices become more and more suppressed closer to the wall, compared to further out. From simulations with different lengths of the cylinder, it was seen that for small cylinder lengths, interference at the end of the cylinder was present. This is discussed

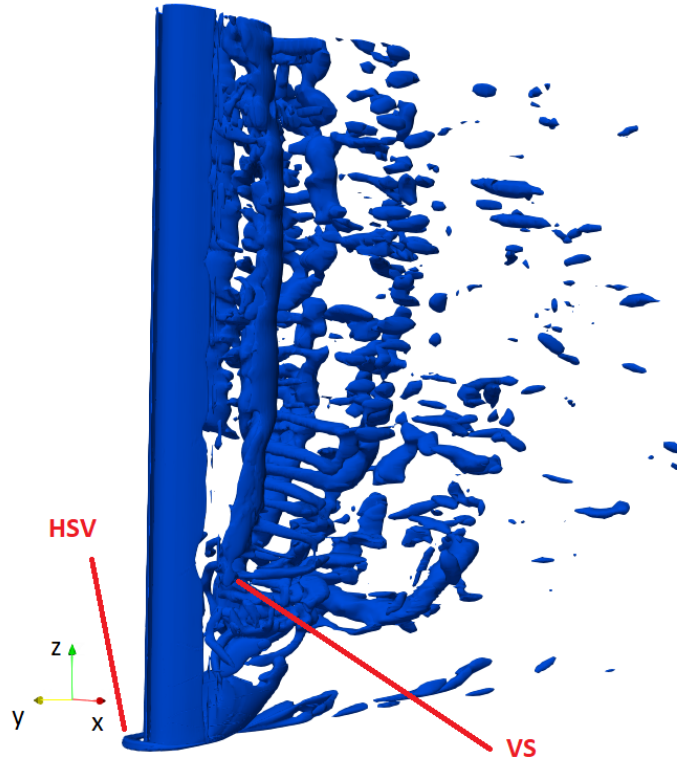
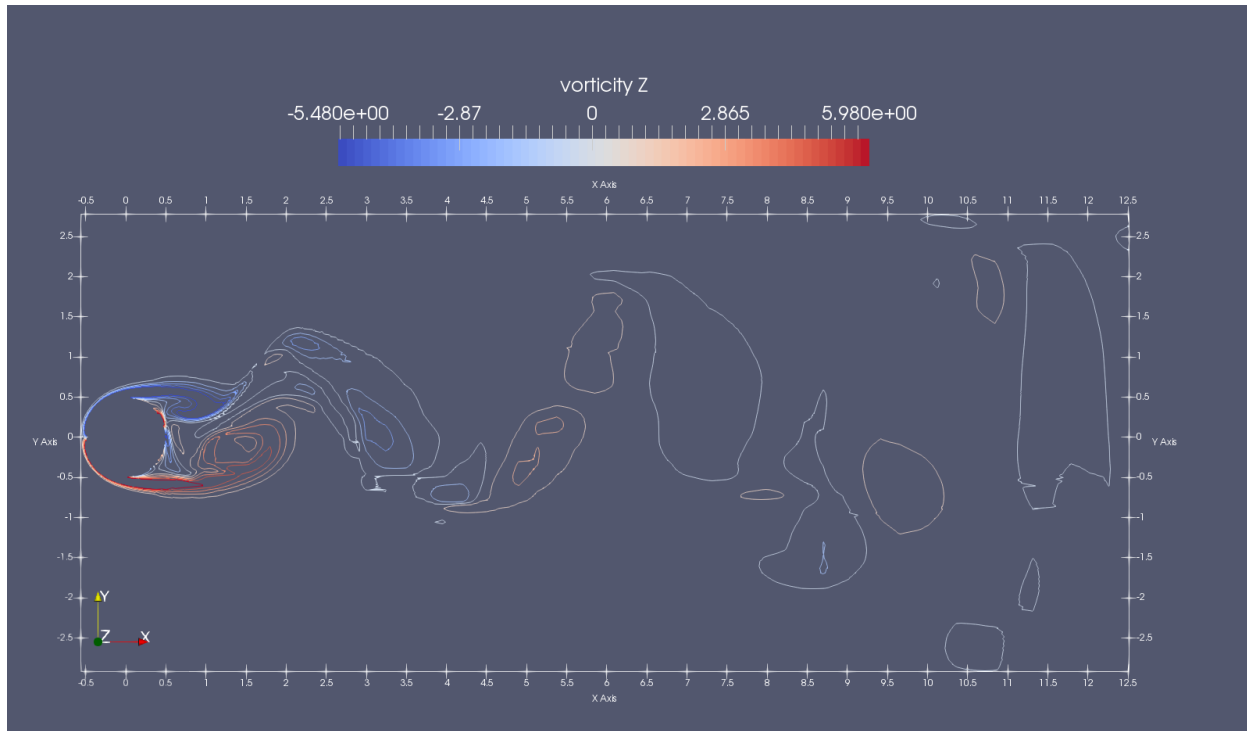


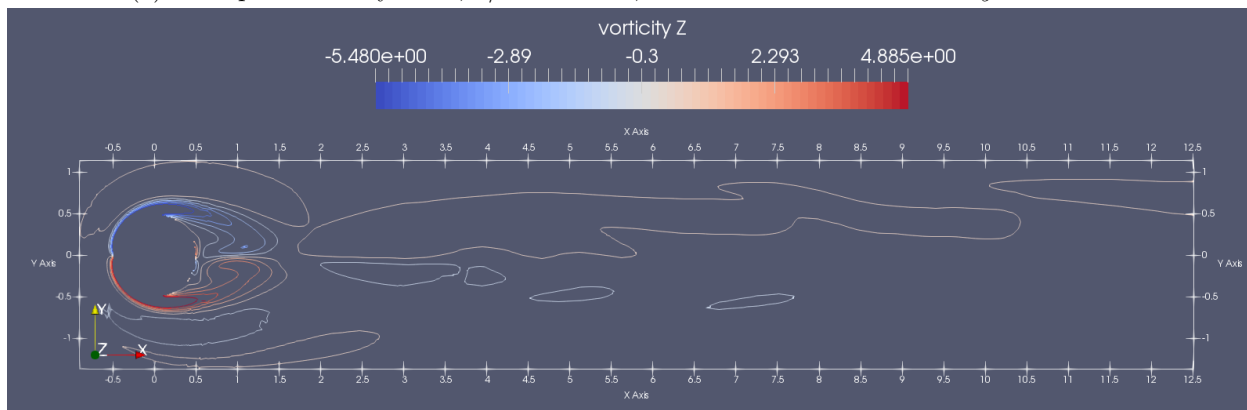
Figure 2.13: Vortex structures visualized by instantaneous iso-surfaces of the  $\lambda_2$ -criterion for  $Re = 500$

in chapter 4.2. The closer the slice of the contour plot is to the wall, i.e.  $z/D = 0.0515$ , the more suppressed the vortex shedding is. At  $z/D \approx 16$ , there is a clear vortex shedding pattern, in comparison. This is comparable to the results by Huang et al. (2011) and Satpathy et al. (2011), who observed that the vortex shedding close to the wall was suppressed, and that the shedding pattern was affected up to the mid-span of the cylinder, which in this case is seen by the vorticity contours of  $z/D = 8$  in figure A.2 in the Appendix. At this location, the vorticity contours show primary vortex shedding as for  $z/D \approx 16$ , but there are some disturbances indicating an effect from the present wall.

Depending on the Reynolds number, the flow experience some kind of horseshoe vortex system. For lower  $Re$ , the junction flow is steady and laminar, and a quite organized and periodic horseshoe vortex system exist. With more turbulent flow, the vortices become unsteady and can cause high turbulence intensity and pressure fluctuations (Simpson, 2001). Both Sahin et al. (2007) and Ataie-Ashtiani and Aslani-Kordkandi (2013) reported a region with reversed flow and strong rollers behind the single cylinder pier. Sahin et al. (2007), on the other hand, observed stagnation points in the upstream base of the cylinder, indicating the mentioned region of reversed flow.



(a) Mid-span of the cylinder,  $z/D = 15.868$ , where  $x = -0.5$  to  $12.5$  and  $y = -3$  to  $3$ .



(b) Close to the wall of the cylinder, at  $z/D = 0.0515$ , where  $x = -1$  to  $12.5$  and  $y = -1.5$  to  $1.5$ .

Figure 2.14: 2D vorticity contours of  $\omega_z$  for  $Re = 500$

## 2.4.2 Pressure and forces

The main focus of many recent articles have been on the flow pattern, and not the complete hydrodynamic analysis, including pressure. The distribution of forces in the article by [Satpathy et al. \(2011\)](#) show a fairly good agreement with the force coefficients for a single cylinder. The pressure distribution have been plotted for three different positions along the cylinder, showing how the pressure is influenced by the presence of a surface. The distribution becomes more flattened out for lower  $z/D$ , than for higher values, meaning that close to the bed, friction is present, and contributes to the development of the horseshoe vortex system.

Figure 2.15 show how the pressure distribution varies for different spanwise locations along the  $z$ -axis of the cylinder. The shape of the curves for  $z/D = 0.0515, 8$  and  $\sim 16$  is in good agreement with [Satpathy et al. \(2011\)](#), as the pressure near the wall is lower compared to further away from the wall. This is due to the bed friction effects, as mentioned above, and leads to fluid flow along the spanwise length of the cylinder to move towards the junction. However, it must be taken

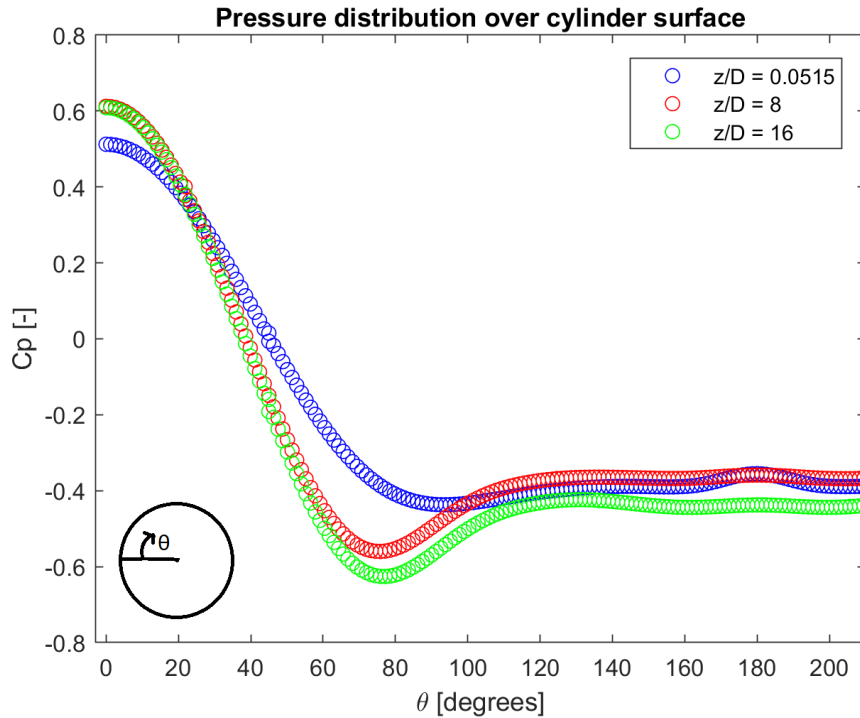


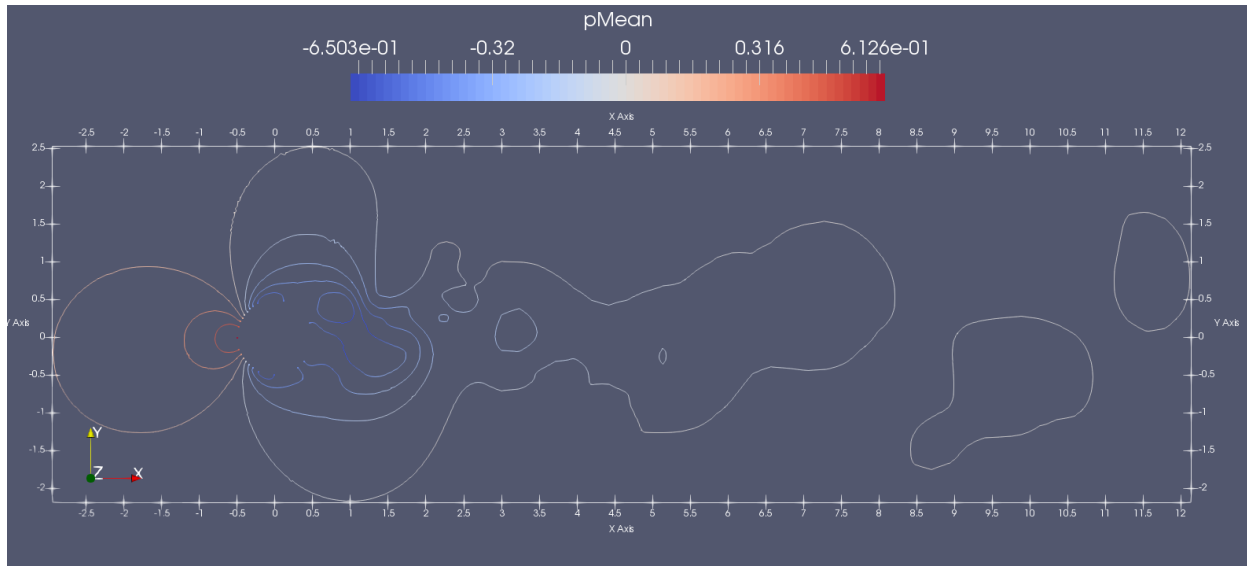
Figure 2.15: Mean pressure coefficient at three different spanwise locations,  $z/D = 0.0515, 8$  and  $\approx 16$ , for a cylinder of length  $16D$  with  $Re = 500$

into account that the figure below is a simulation of  $Re = 500$ , while [Satpathy et al. \(2011\)](#) had simulations of  $Re = 200$ . They also used different spanwise locations, and had a much lower aspect ratio,  $H/D$  or  $L/D$ , than in this current simulation in figure 2.15.

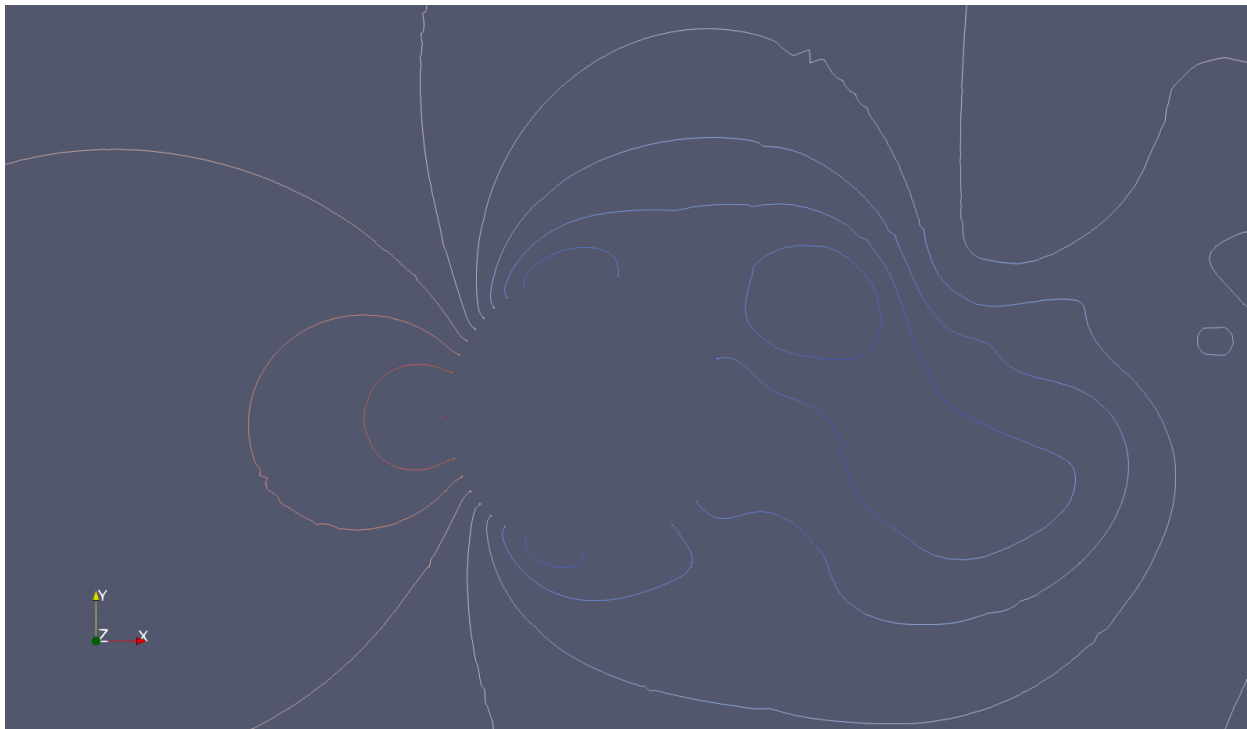
The pressure contours in figure 2.16 show some disturbance in the contour lines. This is because the contours are plotted for  $z/D \approx 16$ , at the end of the cylinder where the mesh is coarser and less refined compared to contours closer to the wall. Figure 2.17 however, show the pressure contours close to the wall, where some disturbance is present in the contour lines. These are mainly present near grid lines, and in the wake of the cylinder. Within the boundary layer, the resolution is good, and there are no visible disturbances in the contour lines. For both spanwise locations, the contour lines show good symmetry in the close vicinity of the cylinder. For  $z/D \approx 16$ , there is a small offset in the lines in front of the cylinder.

The Strouhal number was found by [Ataie-Ashtiani and Aslani-Kordkandi \(2013\)](#) of 0.186 at Reynolds number of approximately  $10^5$ . [Sahin and Ozturk \(2009\)](#) also found the natural vortex shedding frequency, corresponding to a Strouhal number of 0.193, but for a lower Reynolds number of 9600. In this study, a decrease of Strouhal numbers were shown for an increasing number of Reynolds number. This is somewhat in coherence with the result from [Ataie-Ashtiani and Aslani-Kordkandi \(2013\)](#), but needs further investigation. [Fröhlich and Rodi \(2004\)](#), on the other hand, found a dominant vortex shedding frequency with Strouhal number of approximately  $St = fD/U_\infty = 0.16$ , which was recognized from the lift coefficient. The lift do however show a very irregularly changing amplitude and show an average different from zero over a certain number of shedding periods. This can affect the Strouhal number, as the value is a bit lower than what are found for [Ataie-Ashtiani and Aslani-Kordkandi \(2013\)](#) and [Sahin and Ozturk \(2009\)](#).

Figure 2.18 show the FFT-spectrum of Strouhal number for a single cylinder with  $Re = 500$ . This is done using a probe in the vortex shedding region, and a FFT-analysis is carried out for the v-component of the velocity. This resulted in a Strouhal number of 0.11, when the flow was unaffected by the wall at  $z/D \approx 16$ . It was seen that the FFT-analysis was affected by the wall,



(a) Full contours, , where  $x = -3$  to  $12.1$  and  $y = -2.2$  to  $2.5$ .

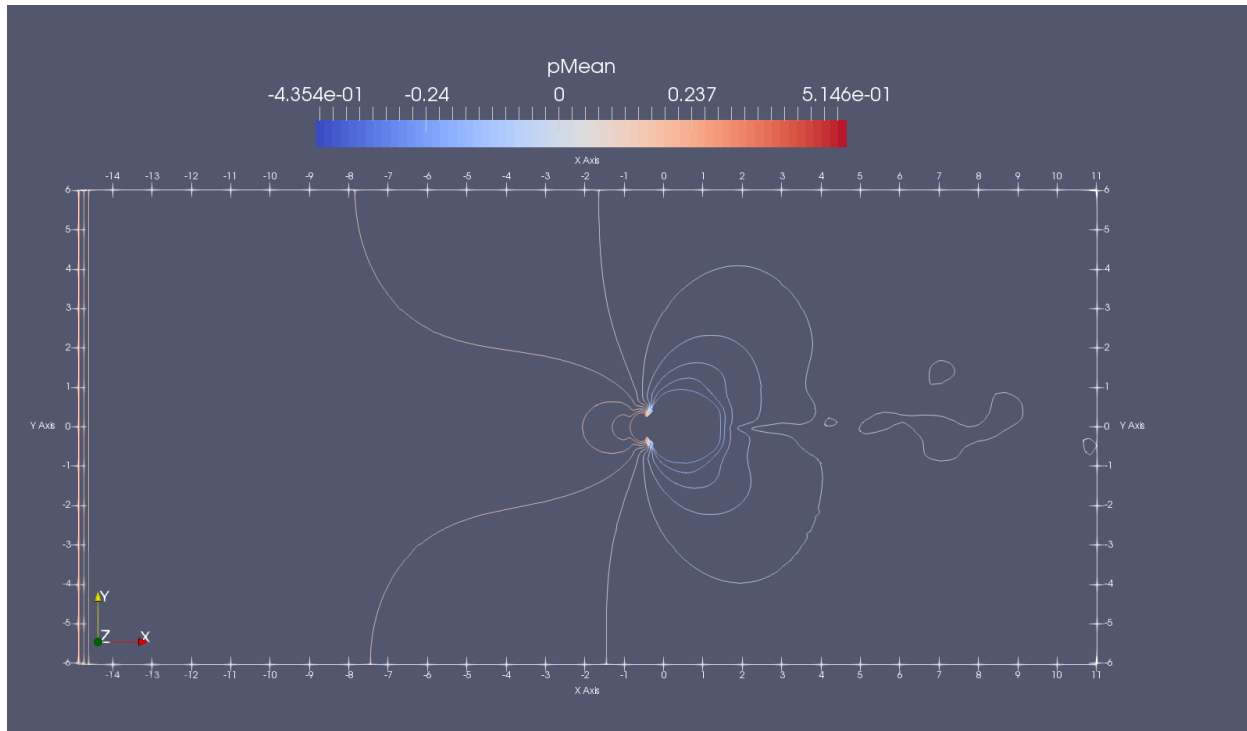


(b) Zoomed in

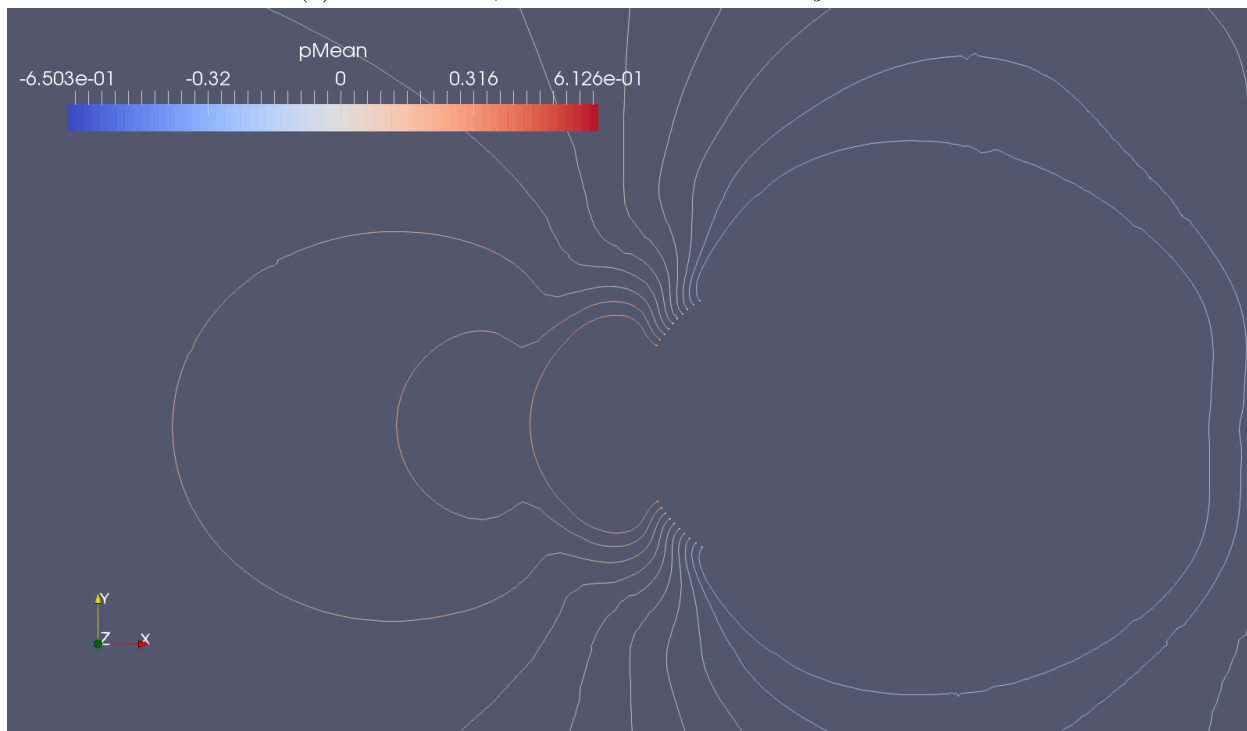
Figure 2.16: Mean pressure contours at spanwise location,  $z/D = 15.868$ , for a cylinder of length  $16D$  with  $Re = 500$

as the amplitude of the highest peak got smaller, the closer to the wall the probe was placed. Only for  $z/D > 4$ , the peak was visible in the plots. However, a larger range of spanwise locations should be considered before concluding with how the Strouhal number vary along the cylinder.

The vortex suppression is further vindicated by the FFT-analysis for different spanwise locations,  $z/D$ , along the cylinder, presented in figure 2.18. At the midspan,  $z/D = 8$ , and at the free end  $z/D = 16$ , a single dominant peak is present, while for lower spanwise locations, the peaks are only notional. For  $z/D = 4$  two peaks are closer to each other, indicating that the vortex shedding is influenced by the friction of the wall. Figure A.5 in the Appendix confirms this, as the streamlines rolls up behind the cylinder. The length of the cylinder is discussed in chapter 4.2. This is in



(a) Full contours, where  $x = -15$  to  $11$  and  $y = -6$  to  $6$ .



(b) Zoomed in

Figure 2.17: Mean pressure coefficient at spanwise location,  $z/D = 0.0515$ , for a cylinder of length  $16D$  with  $Re = 500$

agreement with the observations by [Satpathy et al. \(2011\)](#) for  $H/D = 10$ .

Figure 2.18 show the energy spectra for different spanwise locations along the cylinder axis. It is observed that closer towards the wall, the amplitudes are very small, indicating that the vortex shedding is suppressed. Separate plots of the different Strouhal numbers are shown in figure A.6 in the Appendix.

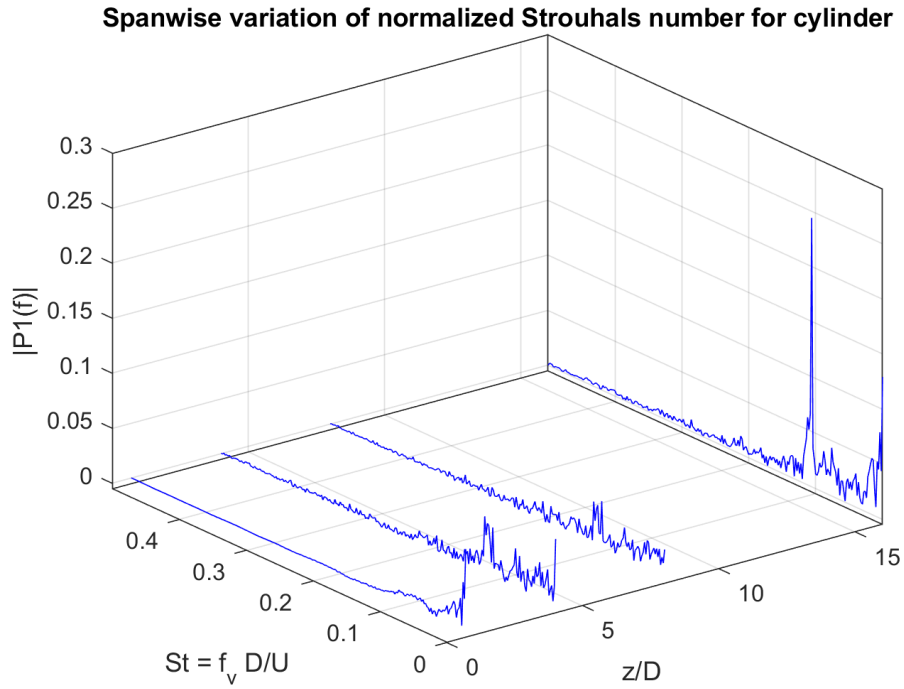


Figure 2.18: FFT-spectrum for different spanwise locations for a case with  $Re = 500$

Table 2.1: Strouhal number for different single cylinder studies

Study	Re	St
<a href="#">Ataie-Ashtiani and Aslani-Kordkandi (2013)</a>	$10^5$	0.186
<a href="#">Sahin and Ozturk (2009)</a>	9600	0.193
<a href="#">Fröhlich and Rodi (2004)</a>	43000	0.16
<a href="#">Satpathy et al. (2011)</a>	200	0.2
<a href="#">Aarnes et al. (2018)</a>	350	0.224
<a href="#">Huang et al. (2011)</a>	100	0.168
Present study for single wall-mounted cylinder	500	0.11

The time history of the drag and lift coefficient are shown in figure 2.19 for a Reynolds number of 500. It shows that the drag oscillates periodically around a mean value of 1.178, while the lift oscillates around 0. The amplitude of the lift coefficient through RMS is 0.1841, while the amplitude of the drag coefficient is 0.0248.

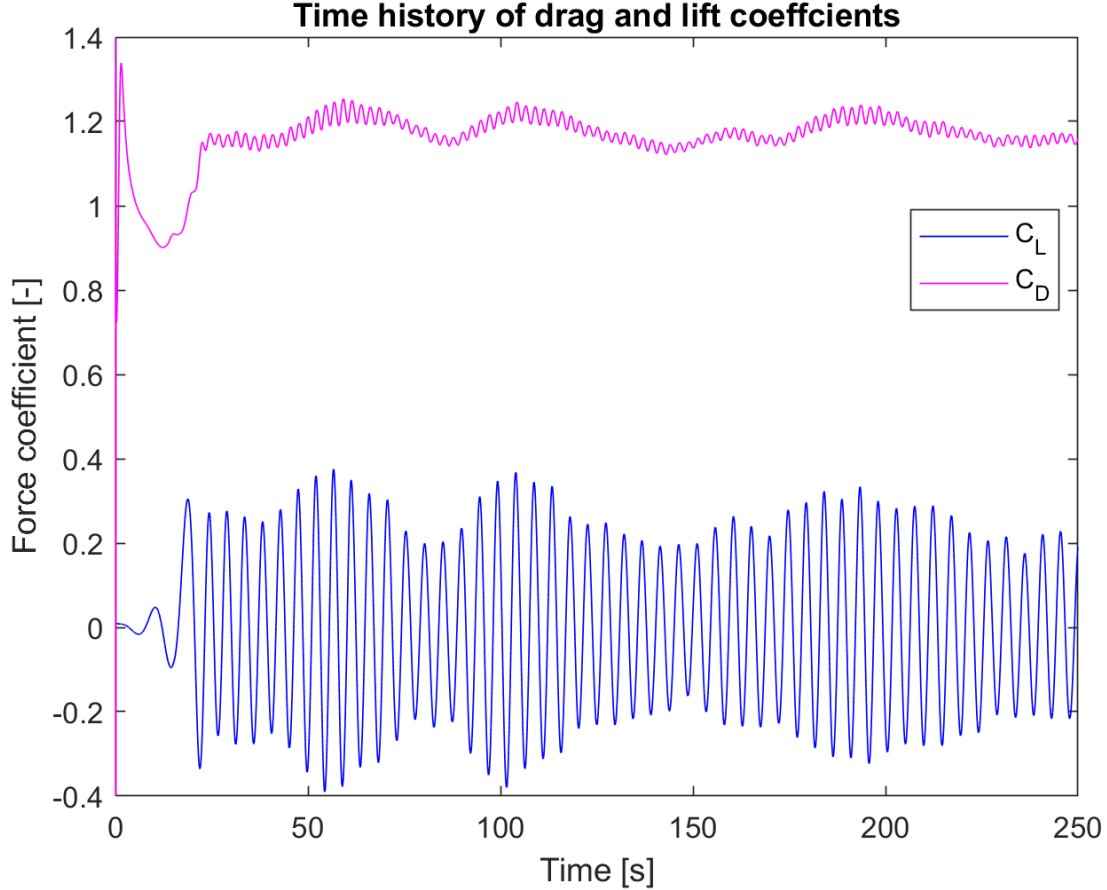


Figure 2.19: Time history of drag and lift coefficient for a single wall-mounted cylinder, at  $Re = 500$

## 2.5 Two cylinders fixed to a surface

Palau-Salvador et al. (2008) investigated the flow around two tandem cylinders mounted to a horizontal surface using LES at  $Re = 1500$ . At this Reynolds number and a spacing ratio of  $S/D = 2.5$ , there is no vortex shedding occurring in the gap between the cylinders, due to the presence of the second cylinder who disintegrates the vortices into small-scale hairpin-type vortex structures. The mean flow is quite complex, and also occurs behind the downstream cylinder.

Ataie-Ashtiani and Aslani-Kordkandi (2013) investigated the flow field around tandem piers using an ADV at quite high Reynolds numbers and a spacing of  $S/D = 3$ . They argue that the flow upstream of two piers is similar to the upstream flow in the single-pier case. However, this similarity will not extend to the downstream flow of both cylinders, due to the presence of the second cylinder. This is in good agreement with observations done by Zdravkovich (2003) and Igarashi (1981) regarding flow around two tandem cylinders. The reverse flow is seen throughout the gap between the piers and near the bed, and it shows a stronger magnitude behind the downstream pier. In this case, partial vortex shedding occurs. In the gap between the cylinders, a binary vortex street is formed, known as the co-shedding regime. At a higher  $z/D$  level on the cylinder, no vortex shedding occurs in the gap. This is due to the shear layers separating from the upstream cylinder move so far downstream that they reattach to the downstream one. This is known as the reattachment regime. The transverse velocity changes inside the gap between the two piers and downstream, as the shear layers that separate from the piers curve towards each other. At the upper level of the cylinders, no such deflection is seen, because the shear layers at this level don't



reach each other, compared to the lower levels near the junction of the bed and the cylinders.

Figure 2.20 illustrate the coherent vortex structure that occurs for flow past two circular tandem cylinders at Reynolds number 500. This is in coherence with the figure provided by [Palau-Salvador et al. \(2008\)](#), where a horseshoe vortex (HSV) is present in front of the upstream cylinder, a vortex structure (VS) is present in the wake, and hair-pin vortices (HPV) occur further down the wake, up to approximately the mid-span of the cylinders.

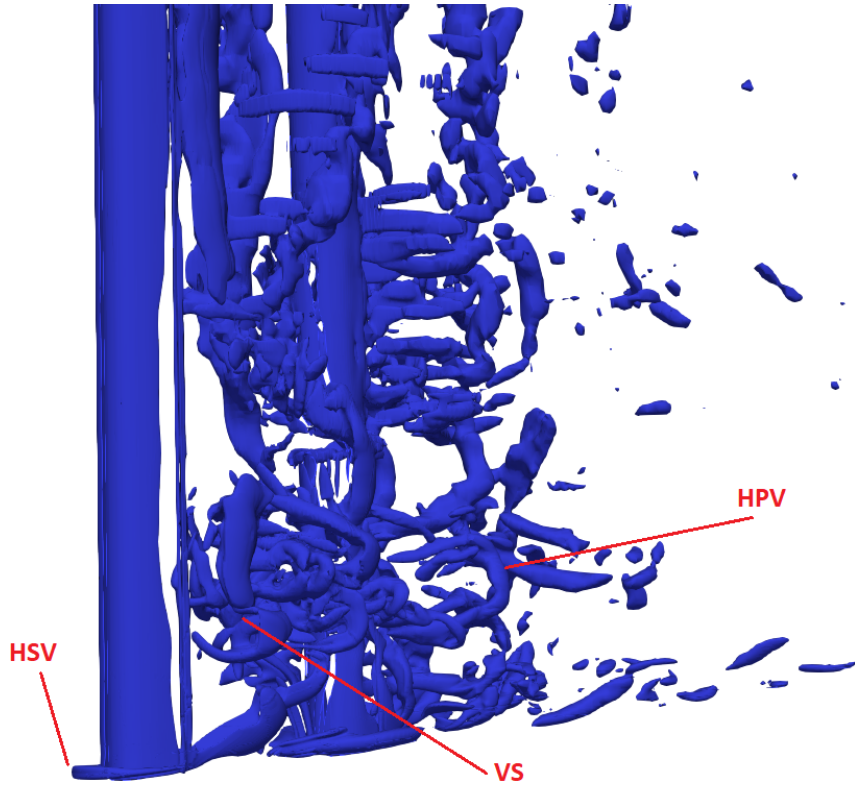


Figure 2.20: Vortex structures visualized by iso-surfaces of the  $\lambda_2$ -criterion, for  $Re = 500$

## Chapter 3

# Computational Fluid Dynamics

### 3.1 Fundamental equations

This section introduces some of the most fundamental equations when using CFD. Some fluid properties are involved, defining some of the most important assumptions of the analysis.

The Reynolds number is one of the most important parameters within flow problems, named after Osborne Reynolds. He found that the fluid flow mainly depended on the ratio of inertia to viscous forces (Cimbala and Cengel, 2013). It can be calculated by equation 3.1, where  $U$  is the fluid velocity and  $L$  is a characteristic length, often the diameter for a cylinder, and  $\nu$  is the kinematic viscosity. The last is described by both the dynamic viscosity and the density of a fluid,  $\nu = \frac{\mu}{\rho} \left[ \frac{m^2}{s} \right]$ . Density describes the amount of mass per unit volume, and having a constant density implies that the fluid is incompressible, while a change in density indicates a compressible fluid. In this thesis, a constant density is assumed, and thereby an incompressible flow. The kinematic and the dynamic viscosity are measurements of friction force, and appears due to internal resistance of a moving fluid.

$$Re = \frac{\rho UL}{\mu} = \frac{UD}{\nu} \quad (3.1)$$

#### 3.1.1 Conservation of mass

A fundamental principle in nature is the conservation of mass. In fluid flow problems conservation of mass describes how the mass flow enters and leaves a control volume during some time interval  $\Delta t$ . It is assumed no change in net mass flow, and it is further assumed that mass flow into a control volume is equal to the outflow of mass.

The conservation of mass can be expressed by the continuity equation, which can be modified to fit a fluid with different properties. Equation 3.2 describe the mass conservation for a 2D steady and incompressible flow problem of a Newtonian fluid. Being incompressible means that the fluid density,  $\rho = 0$ , and this property describes the amount of mass per unit volume (Cimbala and Cengel, 2013).

$$\left( \frac{\partial u}{\partial x} + \frac{\partial v}{\partial y} \right) = 0 \quad (3.2)$$

### 3.1.2 Conservation of momentum

The second fundamental equation is the conservation of momentum, where Newton's 2<sup>nd</sup> law, also known as the linear momentum equation (Cimbala and Cengel, 2013), is taken into account. The general equation for conservation of momentum is given in equation 3.3 (White, 2005).

$$\rho \frac{Du_i}{Dt} = -\frac{\partial p}{\partial x_i} + \frac{\partial}{\partial x_j} \left( \mu \frac{\partial u_i}{\partial x_j} + \frac{\partial u_j}{\partial x_i} \right) + \rho f_i \quad (3.3)$$

The conservation of the fluid momentum can be described in x-, y-direction for  $i = 1, 2$  and  $j = 1, 2$  for a 2D problem. On the left hand side we have a time-dependant component, which describes the change in velocity and the fluid velocity in x-direction and y-direction. On the right hand side of the momentum equation, we find both pressure term, and the dynamic viscosity term with the second derivative for x-and-y-direction, directions i, j, respectively.

The momentum equation can now be rewritten as equation 3.4, which is well known as the Navier-Stokes equation (Cimbala and Cengel, 2013). The Navier-Stokes equations describes the motion of the fluid, but currently it is impossible to solve them analytically for complex flow fields. The equations contains four unknowns, but there are only three equations, one for each dimension (x-, y- and z-direction). Thus, the continuity equation, equation 3.2, can be reckoned as the fourth equation, and the Navier-Stokes equations can be solved numerically.

$$\rho \frac{Du_i}{Dt} = -\nabla p + \mu \nabla^2 u_i + \rho f_i \quad (3.4)$$

## 3.2 OpenFOAM

OpenFOAM is short for Open Field Operator And Manipulation, and is an open source code for a range of engineering and science problems. This can include Computational Fluid Dynamics for i.e. incompressible flow as used in this work. The code is run in a Linux-environment and is based on C++. OpenFOAM does not have a generic solver applicable to all cases, so instead, users must choose a specific solver for a class of problems to solve, meaning that the user may inspect and modify the open source code to coincide with the problem at hand.

OpenFOAM uses the finite volume method (FVM) with cell-centered discretization (Greenshields, 2017), which is used to solve partial differential equations (PDEs) by dividing the computational domain into a finite number of subdomains or control volumes (CV). The "finite volume" refers to the small volume that surrounds each node in the mesh (Moukalled et al., 2016), which is where the unknown variables are to be computed.

# Chapter 4

## Numerical set-up

This chapter describes the numerical setup used in the simulations. When doing CFD, three stages are necessary to get a good analysis, pre-processing, solving the problem and post-processing. The first and most important stage of a CFD-analysis, is the pre-processing, where the geometry of the computational domain and a mesh is generated. Boundary conditions and initial conditions are defined in order to solve the governing equations for the physical problem. The software, in this case OpenFOAM, solves the governing equations and the output is stored in the case-folder for different time steps. Lastly, the post-processing stage takes the results obtained in the analysis and presents them in various ways using data processing and visualization.

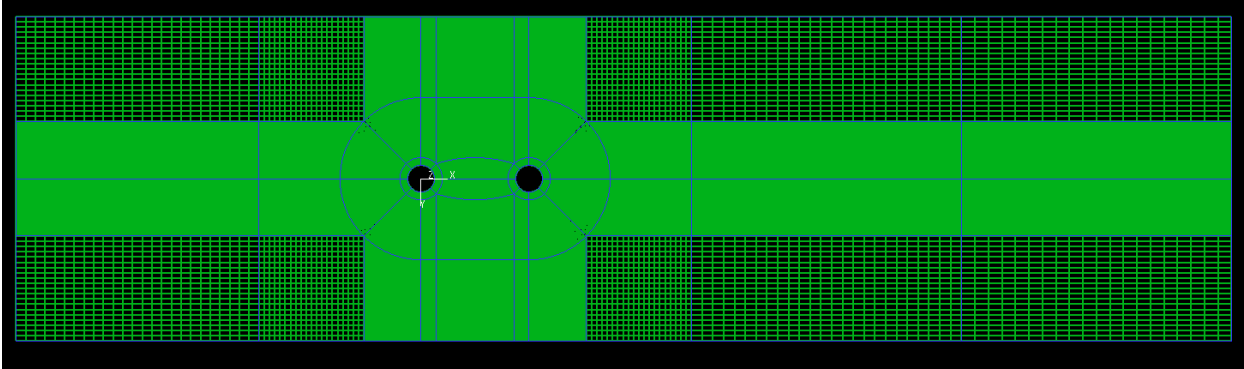
### 4.1 Computational domain and grid

The computational domain used in this case is a three-dimensional rectangular shape, consisting of two cylinders in tandem arrangement. Figure 4.1a show a 2D, non-scaled version of the domain, where the streamwise (x) direction reads  $45D$  and the transverse (y) direction reads  $12D$ . The length of the domain in the spanwise direction (z) is set to be  $16D$ , which is found to be sufficient to capture the 3D effects of the flow and being long enough to avoid finite length effects. Each of the cylinders are given a diameter of  $D = 1m$ , and the spacing-to-diameter ratio between the two cylinders is set to be 4, based on the technical report regarding the SFTB (Team, 2016), which is mentioned in chapter 1.1.1.

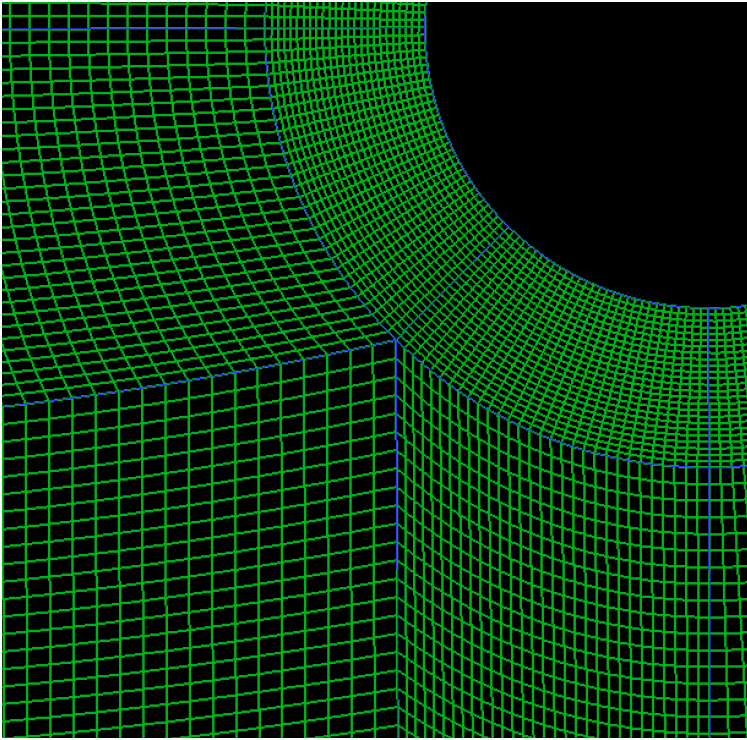
Both the shape and size of the computational domain are based on previous research regarding flow past tandem cylinders and flow past a cylinder fixed to a wall. The computational domain is discretized into a structured grid, and near the cylinders, an O-mesh is created. This zone is held constant with 300 elements around the cylinder circumference. The next zone consists of an ellipsoid, that encloses both cylinders and the wake behind the upstream cylinder. The outer parts of the domain consists of a structured H-mesh with a rectangle surrounding the ellipsoid with the cylinders, and also a zone for the far end of the domain and zone for the development of the boundary layer of the domain.

The inner O-mesh and first zone, closest to the cylinder surface, has a width of  $0.2D$ . This gives good control of the grid cells close to the cylinders. The most critical regions of the domain is close to the cylinder surfaces, the gap region and close to the wall, and these areas require a fine mesh in order to capture all the changes in the flow. This is shown in figure 4.1b, where the left lower quadrant have a lower density of cells. This may look a bit alarming, and could be refined even more, but due to computational time and capacity, it was concluded to be satisfactory in the present study. This conclusion was drawn according to the pressure contours that are discussed further in chapter 5.3.

In the z-direction, 360 elements are distributed with a higher density of cells close to the wall, rather than at the free end. The focus of this thesis is the effects near the wall, hence the refinement of elements in z-direction. Having described the different mesh zones in the computational domain, it results in a total of 25.2 million elements, which is divided into 240 processors for parallel run using the supercomputer *Vilje*.



(a) 2D slice of the mesh showing the blocks and the grid refinement



(b) Mesh details around the cylinder

Figure 4.1: 2D illustration of the mesh in the x-y-plane

## 4.2 Boundary conditions

The boundary conditions applied to the domain boundaries are essential for the solution of the analysis. Ideally, it is desired that the computational domain is infinitely large and is not affected by imposed boundary conditions. In practice, there are limitations to the simulation, in form of computational time and memory. These depend highly on the computer available, but in order to make the simulation as cheap and efficient as possible, a small domain with few elements is preferred.

At the inlet, the velocity vector,  $U = (u, v, w)$ , is given a fixed value of  $U = (1, 0, 0)$ . Physically this means that there is only a uniform flow in the x-direction of the domain. The pressure on the other hand is a scalar, and thereby have no specific direction. The pressure is set with zero gradient at the inlet, meaning that the pressure does not change in value in any direction or in magnitude close to the inlet.

At the outlet, the pressure is set to a fixed value of 0, which physically means that the outlet pressure is equal to the pressure of the undisturbed fluid. There are however some difficulties regarding this condition, since the wake flow behind a bluff body is affected by the vortices shed from the cylinder at a very long distance from the body. To some extent, these vortices die out, but there might be irregularities. It is therefore assumed, by using this condition, that the outlet is so far away from the body, that the boundary condition will not effect any of the flow parameters on the body.

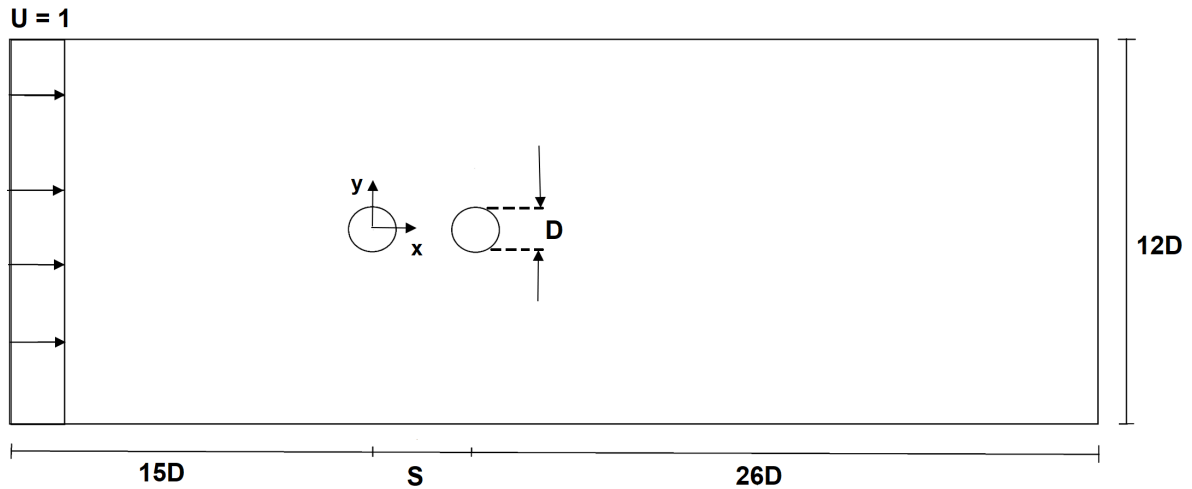


Figure 4.2: Computational domain definition sketch for tandem cylinders fixed to a wall. Uniform inflow velocity profile. For the present study,  $D=1$ ,  $S=4D$

The two cylinders and the vertical wall, or back side of the domain, have a no-slip condition, meaning that all the three velocity components are zero and the boundaries are treated as walls. According to [Cimbala and Cengel \(2013\)](#), the no-slip condition here coincides with how the water particles act near a solid body. The pressure is set to have a zero gradient, and this condition is widely used for a no-slip condition, i.e. [Prsic \(2016\)](#) and [Kalvig \(2015\)](#).

The top and bottom of the computational domain have a slip boundary condition. This means that the velocity have to meet two conditions, normal and parallel to the patch. Since the top and bottom of the domain are adequately far away from the cylinders, not influencing the induced fluid velocity in planes parallel and close to the nearest wall, the normal components have a fixed value, while the tangential components have zero gradients. The pressure is a scalar, and the slip condition sets the scalar parameters to have a zero gradient condition. The slip condition is numerically the same as the symmetry condition, as it represents no flow through the top and bottom of the domain by setting  $v = 0$ , while x- and z-components of the velocity are more free and allowed to flow along the boundaries due to the zero gradient.

At the free end of the cylinder, the front of the domain, a free slip condition is imposed. In practice, a friction free wall is implemented here, which is similar to what [Huang et al. \(2011\)](#) did. It is important to have a long enough cylinder to avoid the effects from a finite height cylinder, where the flow will act differently. [Palau-Salvador et al. \(2008\)](#) also used a slip-condition at the so-called free surface of the cylinder, to act as a friction-less rigid lid.

Table 4.1: Overview of different boundary conditions applied in the domain

Patch	Velocity (U) BC	Pressure (p) BC
topAndBottom	$\frac{\partial U}{\partial z}, \frac{\partial U}{\partial x}, v = 0$	$\frac{\partial p}{\partial x_j} = 0$
cylinder	$U = 0$	$\frac{\partial p}{\partial x_j} = 0$
inlet	$v = w = 0, u = 1.0$	$\frac{\partial p}{\partial x_j} = 0$
outlet	$\frac{\partial U}{\partial x_j} = 0$	$p = 0$
front	$\frac{\partial U}{\partial z}, \frac{\partial U}{\partial x}, v = 0$	$\frac{\partial p}{\partial x_j} = 0$
back	$U = 0$	$\frac{\partial p}{\partial x_j} = 0$

### Length of domain - cylinder length

The length of the cylinder is chosen based on previous work during the semester and similar articles. During this work, simulations for a single cylinder fixed to a wall with lengths of  $4D$ ,  $8D$ ,  $12D$  and  $16D$  were investigated. To avoid the free end effects, see chapter 2.4, the final simulations had a cylinder length of  $16D$ . By looking at figures A.3, A.4 and A.5 in the Appendix, it is clear that the effects for a length of both  $4D$  and  $8D$  are highly present. For a length of  $12D$ , the streamlines from the *ParaView* StreamTracer, moves quite far along the cylinder, and by adding a second cylinder, the flow might be interact with the wall even further than  $12D$ . Hence, a cylinder of length of  $16D$  is a better choice, especially with adding another cylinder to the domain in mind.

Comparing with previous research, Huang et al. (2014) used a length-to-diameter ratio of 11 for an experiment in a rectangular water tank, while Marakkos and Turner (2006) had an aspect ratio yielding 10.66 in their PIV experiment. Ataie-Ashtiani and Aslani-Kordkandi (2013) on the other hand, through a laboratory flume experiment, had a length-to-diameter ratio of only  $\sim 3$ , while Huang et al. (2011) used  $L/D = 6$ . In the range of articles used as a basis for this thesis, the length-to-diameter ratio varies a lot. Due to the discoveries in the streamlines mentioned above, a longer cylinder is needed to make sure the vortex structure in the wake is not interfering at the end of the cylinder. The cylinder in this case is meant to be infinitely long, and is simulated in such matter with a length of  $16D$ .

### Grid verification

The grid used for the simulations is evaluated in this section. A convergence study is beyond the scope of this thesis and will not be performed. The shape of the grid is based on previous research from i.e. Prsic (2016), Kalvig (2015), Palau-Salvador et al. (2008) and Fröhlich and Rodi (2004), and the criteria set by the OpenFOAM software with regards to non-orthogonal elements and the element aspect ratio's. The mesh grid was developed over time using trial and error. Figure 5.1a shown the resolution along the span of the cylinders in the x-z-plane. Grid generation has been a huge part of this work, and could probably be improved even further, especially in the upper region in figure 5.1a, where the transition is quite brutal. All in all, the aforementioned articles inspired the shape of the grid, while the criterias set and checked by OpenFOAM served as guidelines to produce a acceptable mesh grid.

The boundary layer is a crucial part of the grid, and it needs to have a fine resolution with many elements to be able to capture the flow aspects. With a wall present in the domain, the boundary

layer is not only present at the cylinders, but also at the wall. To check whether the boundary layer is resolved in a satisfactory way, the velocity profiles are plotted. The velocity gradient require a smooth velocity profile, as the calculation of vorticity depends on this parameter. Three different locations along the cylinder surface have been chosen, shown in figure 4.3.

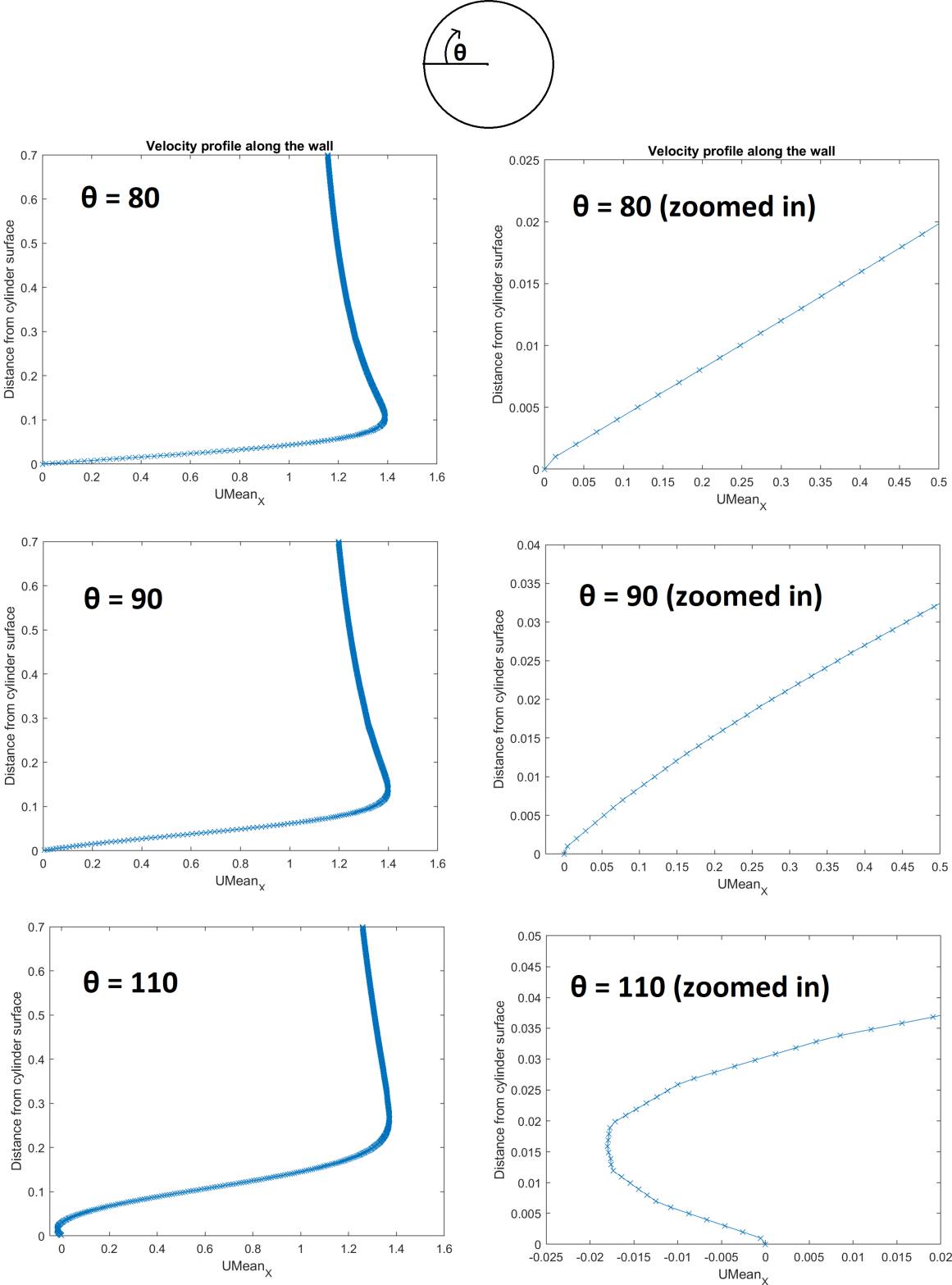


Figure 4.3: Velocity profiles at three different locations along the cylinder surface

The locations of the three velocity profiles are chosen based on chapter 2.2.2. For  $\theta = 80^\circ$ , a



smooth profile is seen close to the cylinder, as well as for  $\theta = 90^\circ$ . However, some disturbance is present for  $\theta = 110^\circ$ , where straight lines between points are observed. This is not a desirable feature, but the velocity profile have preserved the details and is sufficiently refined close to the cylinder surface.

### Inlet length

The inlet length of the computational domain is very important in order to have a fully developed boundary layer along the wall in front of a cylinder. In order to find a sufficient inlet length, a simple 3D simulation with uniform flow along a flat plate was carried out. Along the length of the domain, one boundary was set to a no-slip condition. At several locations along the x-axis, velocity profiles were plotted. The boundary layer was found to be fully developed at an inlet length of about  $15D$ . This seems to be in agreement with previous research by i.e. [Huang et al. \(2011\)](#) where an inlet length upstream of the cylinder is set to  $15D$  as well. [Sahin and Ozturk \(2009\)](#) on the other hand, used an inlet length of  $40D$  to avoid any disturbances that may occur in the experimental test chamber, and [Satpathy et al. \(2011\)](#) used only an inlet length of  $4D$  for a Reynolds number of 200. There is quite a variation of the inlet lengths in literature, but based on the simulation conducted for finding the correct inlet length in this case, an inlet length of  $15D$  was chosen and verified below.

To the left in figure 4.4, two velocity profiles along the wall in front of the cylinder are shown. In order to determine if the velocity profile has fully developed in the wall boundary layer, the plot to the right in figure 4.4 show the same profiles only zoomed in. This shows that the profiles are smooth and the details are preserved. The red line, for  $x = -1.25$ , show signs of backflow, indicating that the separation of flow starts around here and a horseshoe vortex system can be formed. The blue line, however, show that the boundary layer has fully developed in front of the cylinder.

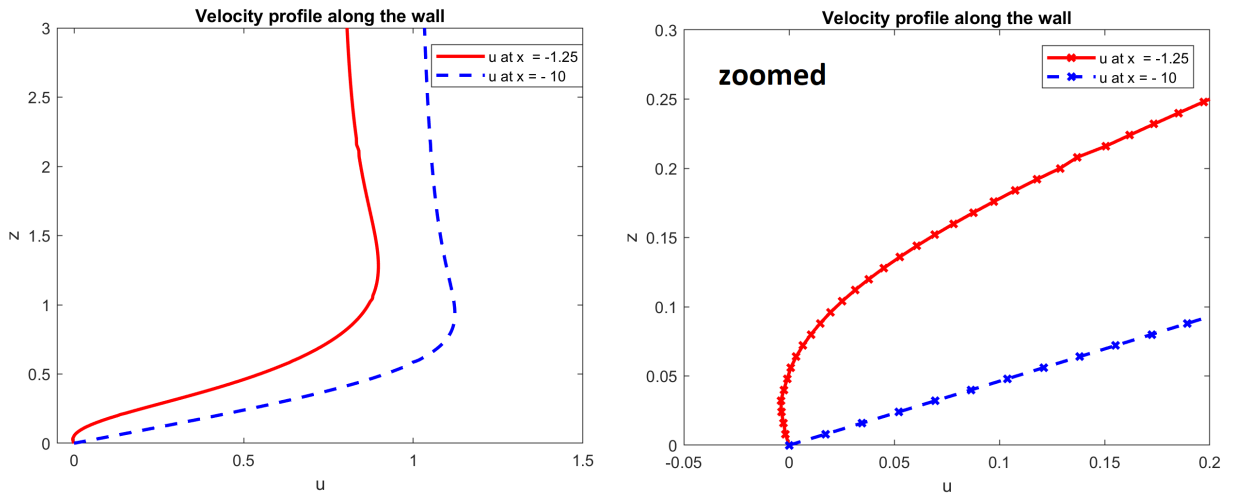


Figure 4.4: Velocity profiles along the wall of  $U_x$ , in front of the upstream cylinder

### 4.3 Solver settings

In this study, Direct Numerical Simulations (DNS) was carried out for all simulations using OpenFOAM. Using the direct solver means using no approximations and that the error is controllable, originating from the numerical discretization only. The use of DNS is possible due to the low range of Reynolds numbers, as this tool comes with a certain cost: a large number of degrees of freedom.

In the present study, a body-fitted structured hexahedron mesh is used for all cases. The details of the mesh, such as refinement, is given above in chapter 4.1.

The PISO-algorithm (Pressure Implicit with Splitting of Operators) is an iterative procedure for coupling equations for momentum and mass conservation for transient problems, and involves one predictor step and two corrector steps. First, the pressure field is set to  $p^*$ , which give the velocity fields  $u^*$  and  $v^*$ . If the pressure field is not correct, the velocity components will not satisfy the continuity equation. Next, new velocity fields are given by the first corrector step who satisfy the discretized continuity equation. As this is an iterative procedure, the corrected values will be substituted into the discretized continuity equation. This yields the pressure correction equation, giving the velocity components  $u^{**}$  and  $v^{**}$ . The second corrector step results in a twice-corrected velocity field, and a new pressure correction is found. The twice-corrected pressure,  $p^{***}$ , is now found using substitution into the discretized continuity equation and this process is repeated until convergence.

The solver can have many different settings for different problems, making it very important to have the correct ones for an effective simulation. The tolerance for the iteration process is described in the fvSolution-script, located in the system-folder, and is set to  $10^{-6}$  for pressure and  $10^{-5}$  for velocity. The scripts can be found in Appendix B.

Discretizing equations is the process of converting PDEs into a set of algebraic equations. These can be written in either matrix or vector form, and then be integrated over the cell volumes. The fvSchemes-script contains the methods used, which in this thesis is the Crank Nicolson-method for time integration and Gauss linear for the gradient terms. Both schemes are of second order accuracy (Greenshields, 2017).

## 4.4 Visualization

Visualization is a very important part of the post-processing, and it is carried out using the open-source visualization application *ParaView*. As a visualization tool, the user have to be aware of how the tool manipulates the results obtained during the simulation. *ParaView* offers both cell-based or point-based representation, where the first assumes that the value is constant throughout the cell. Point-based representation, on the other hand, interpolates the values in the points, such that the field is smooth. It is also important to be aware that *ParaView* gives the parameter values at the cell corners, while OpenFOAM stores the values in the center. This difference might cause interference when visualizing.

### 4.4.1 Identification of vortices

Vortex identification has been widely discussed within visualization, and Jeong and Hussain (1995) presented some definitions that are used to identify vortices. They defined two requirements for having a vortex present,

- a net vorticity, hence circulation, about the vortex core must be present, and
- the geometry of the identified vortex core should be Galilean invariant.

How the vortex identification is done in OpenFOAM and *ParaView*, is briefly discussed in this section.

## Vorticity

As the flow separates from a cylinder, a shear layer is formed. In this layer, there is something called vorticity, which is describing how much a small fluid element is rotating. During a small time step  $dt$ , the fluid element has moved, and the degree of the rotation can be measured by an angular velocity  $\omega$ . The vorticity is then equal to twice the angular velocity of the fluid particle (Cimbala and Cengel, 2013).

The vorticity in 3D can be defined as the following in equation 4.1 (Cimbala and Cengel, 2013).

$$\vec{\zeta} = \nabla \times \vec{V} = \left( \frac{\partial w}{\partial y} - \frac{\partial v}{\partial z} \right) \vec{i} + \left( \frac{\partial u}{\partial z} - \frac{\partial w}{\partial x} \right) \vec{j} + \left( \frac{\partial v}{\partial x} - \frac{\partial u}{\partial y} \right) \vec{k} \quad (4.1)$$

Jeong and Hussain (1995) reports that  $|\omega|$ , the vorticity magnitude, is not sufficient for the identification of vortices in a boundary layer, since it doesn't identify vortex cores in a shear flow. To be able to identify vortices more properly in shear flow, other criterion's are proposed. Among these are the Q-criterion and  $\lambda_2$ -criterion, both based on the velocity gradient tensor,  $\nabla \mathbf{u}$ . The eigenvalues of  $\nabla \mathbf{u}$  satisfy the characteristic equation  $\sigma^3 - P\sigma^2 + Q\sigma - R = 0$ . P, Q and R are all invariants of  $\nabla \mathbf{u}$ .

The second invariant, Q, is defined as:

$$Q = \frac{1}{2} \left( u_{i,j}^2 - u_{i,j}u_{j,i} \right) = -\frac{1}{2}u_{i,j}u_{j,i} = \frac{1}{2} \left( \|\mathbf{\Omega}\|^2 - \|\mathbf{S}\|^2 \right) \quad (4.2)$$

where  $\mathbf{\Omega}$  and  $\mathbf{S}$  are the symmetric and anti-symmetric components of  $\nabla \mathbf{u}$ . Physically, this invariant represent a balance between shear strain and vorticity magnitude at a certain point. The Q-criterion is based on  $Q > 0$ , where the vorticity magnitude is larger than the shear strain, and hence a vortex can appear. Jeong and Hussain (1995) proposed a new definition, as a pressure-minimum criterion as equation 4.2 is not sufficient for capturing the effects at both high and low Reynolds numbers.

The vorticity transport equation, equation 4.3, is a good starting point for the new definition, where only  $\mathbf{S}^2 + \mathbf{\Omega}^2$  is considered. If  $\lambda_1 \geq \lambda_2 \geq \lambda_3$  are the real eigenvalues, the new definition is said to be equivalent to  $\lambda_2 < 0$  within the core of the vortex.

$$\frac{DS_{i,j}}{Dt} - \nu S_{ij,kk} + \Omega_{ik}\Omega_{kj} + S_{ik}S_{kj} = -\frac{1}{\rho}p_{i,j} \quad (4.3)$$

The  $\lambda_2$ -criterion is argued to be a better choice as it can easily identify idealized vortices at lower Reynolds number, as illustrated by Jeong and Hussain (1995). This definition captures the minimum pressure in a perpendicular plane to the vortex at high Reynolds numbers, and also accurately defines the vortex cores at low Reynolds numbers. Figure A.7 in the Appendix show instantaneous iso-surfaces for both the  $\lambda_2$ - and Q-criterion for a specific level. Both criterion's show a very similar coherent structure for a low threshold, and this seems to hold for a low Reynolds number as in this study.

### 4.4.2 Streamlines

The streamlines are an important part of the visualization of the current problem. According to Cimbala and Cengel (2013) the streamlines are curves that are instantaneously tangent to the flow velocity vector. This indicates that streamlines are field lines showing the direction of the fluid

flow. For circular cylinders, streamlines are often used to find separation points. Mathematically, streamlines are written as:

$$\frac{dr}{V} = \frac{dx}{u} = \frac{dy}{v} = \frac{dz}{w}. \quad (4.4)$$

In experiments, streamlines cannot be seen, but they are often implemented by visualization programs in order to indicate flow direction. Streaklines, however, are the lines seen in experiments where dye or smoke is injected at a certain point, while pathlines is a trajectory that is followed by individual fluid particles. These must not be confused with each other, as only in steady flow pathlines, streaklines and streamlines are the same. Streamlines give the instantaneous picture and must be used with special care. The mean velocity field is thus utilized to create streamlines, giving a more accurate picture.

SurfaceLIC is an application in *ParaView*, used to visualize a vector field such as streamlines. The technique applied is called Line Integral Convolution (LIC) and it convolves noise with a vector field to produce a streaking pattern that follows the vector field tangents ([Ayachit, 2016](#)).

# Chapter 5

## Results

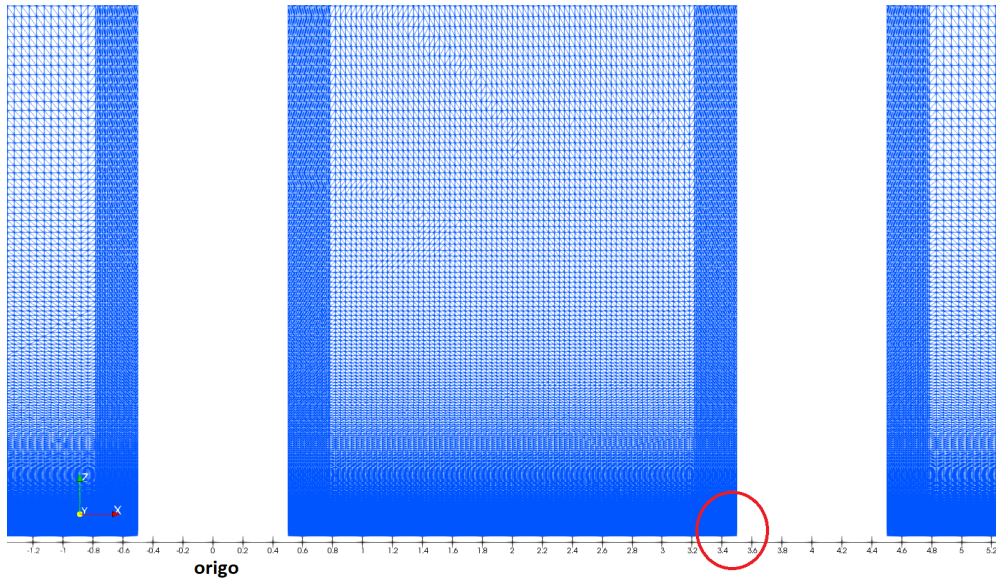
This chapter presents the results obtained during the simulations and some discussion of these. Table 5.1 show some summarized details from the final simulation, including the size of the grid and time step used. The final simulation was run for 250 s in order to have a stabilized solution and enough vortex shedding periods to get proper statistics for relevant attributes, e.g. the Strouhal number and time-averaged results. In this chapter, figures have been essential for presenting results, hence why many have been enlarged for this chapter.

Table 5.1: Details of simulation

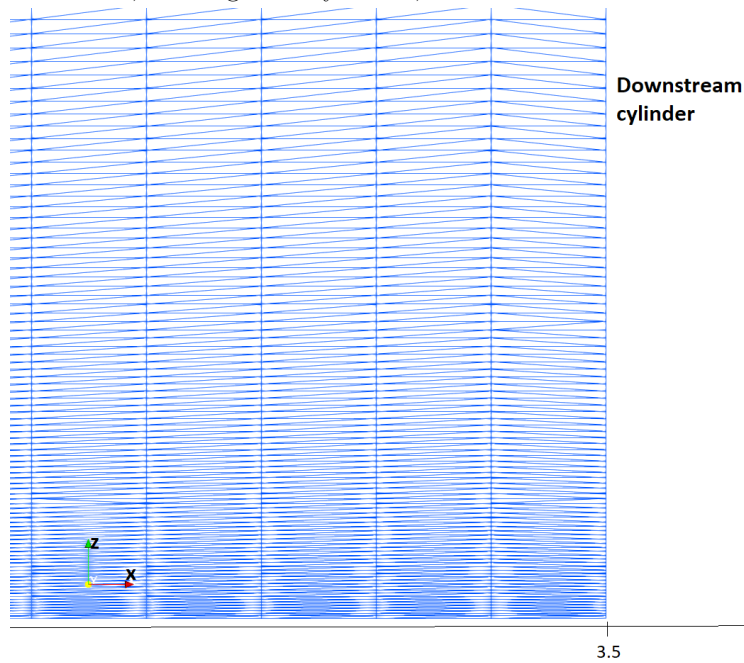
Number of elements	25.2 million
Elements around cylinder circumference	300
Elements in boundary layer	30
$\Delta t$	0.004
Spacing between cylinders, S/D	4
Length of cylinder, L/D	16
Reynolds number, Re	500

Section 5.1 describes the vorticity distribution along the cylinders using instantaneous iso-surfaces. The flow pattern around the two circular tandem cylinders is described in section 5.2, where streamlines, velocity vectors and normalized velocity-plots are used to describe the characteristics of the flow. Further, section 5.3 contains contour plots and pressure distributions over the cylinder surfaces, and a discussion of the quality of the solution. The forces acting on the two cylinders are described in section 5.4, where the time histories of the drag and lift coefficients are plotted and compared to existing results in literature. Lastly, section 5.5 takes care of the Strouhal number and how it varies along the span of the cylinders.

Figure 5.1a show the refinement of the of the grid in the x-z-plane. The results obtained during the simulations have a high level of detail in this region, and the refinement is essential for accurately capturing the different flow features occurring near the junction.



(a) Close to the wall, showing both cylinders, where  $x = -1.4$  to  $5.3$  and  $z = 0$  to  $2$ .



(b) Zoomed in, red circle in the figure above

Figure 5.1: The resolution of the mesh grid in the x-z-plane

## 5.1 Vorticity

Figure 5.2 show the instantaneous iso-surface for  $\lambda_2 = 1$  viewed along the span of the cylinders. The flow direction is along the x-axis. Behind the upstream cylinder, a clear vortex structure is forming, impinging upon the downstream cylinder. A single primary vortex is observed in front of the upstream cylinder as stated by Visbal (1991) for a junction flow for a Reynolds number of 500.

Around the downstream cylinder, a more chaotic flow is observed, compared to the upstream cylinder. This is due to the vortex shedding from the upstream cylinder that influence the wake flow and thereby incoming flow to the downstream cylinder, which is seen in figure 5.4. At the end of the cylinders in figure 5.2, opposite from the junction, the flow is considered to be almost

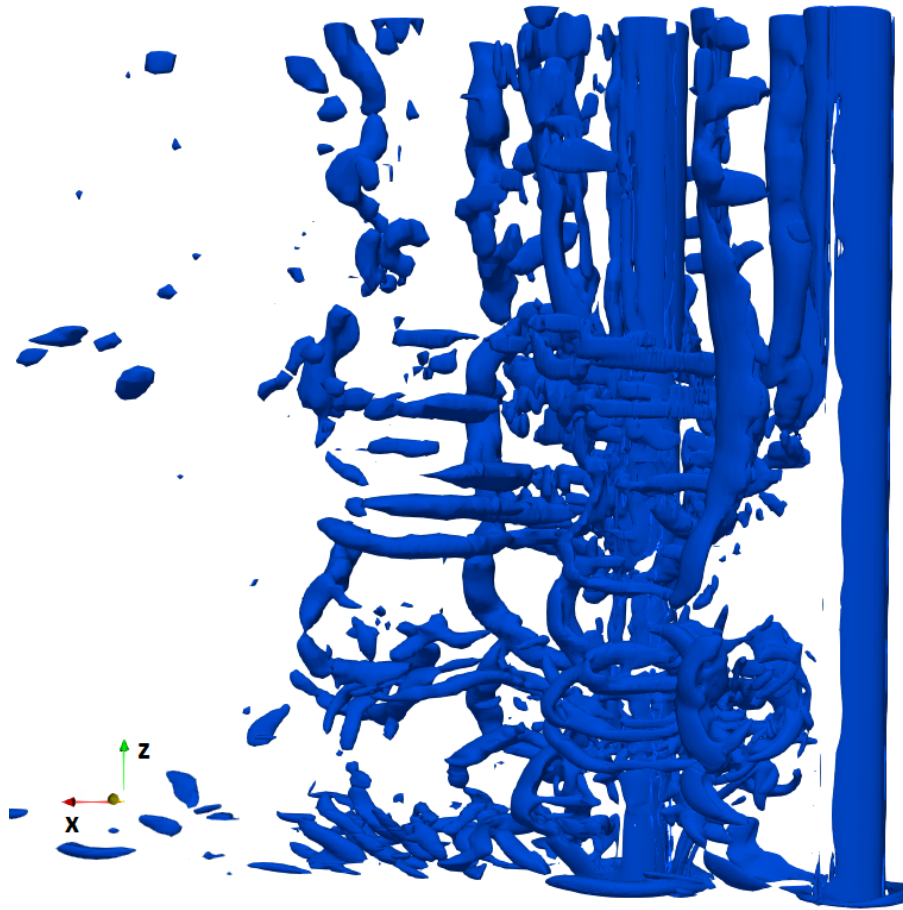
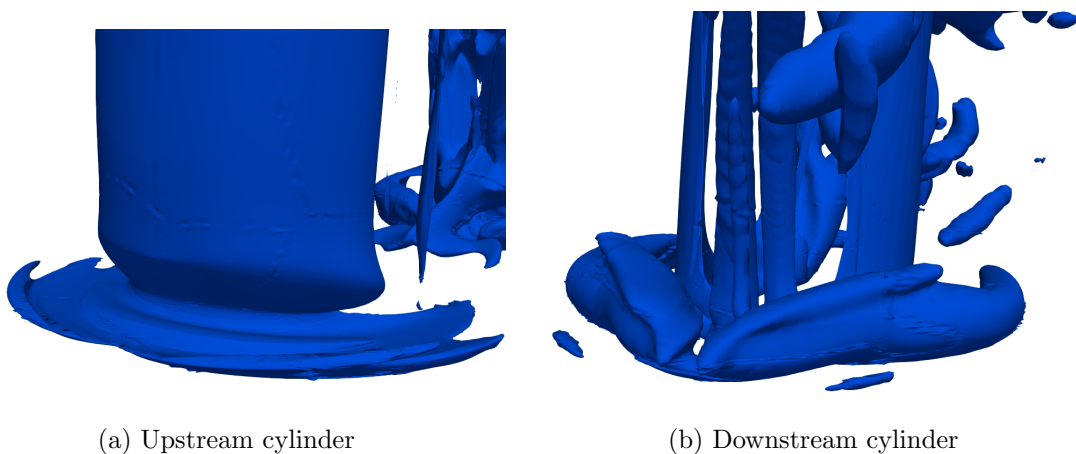


Figure 5.2: Instantaneous  $\lambda_2 = 1$  iso-surfaces, viewed from above

free of effects from the upflow created by the horseshoe vortex. Here, synchronized or parallel vortex shedding can be seen, as observed by [Zdravkovich \(1996\)](#). This, and the impingement of the vortices from the upstream cylinder, cause the large forces acting on the downstream cylinder, which is further discussed in chapter 5.4.



(a) Upstream cylinder

(b) Downstream cylinder

Figure 5.3: Instantaneous iso-surfaces for  $\lambda_2 = 2$  in upstream of each cylinder

Figure 5.3 show the instantaneous iso-surfaces in front of both the upstream and downstream cylinders for  $\lambda_2 = 2$ . In front of the upstream cylinder, the main coherent structure clearly comprise the horseshoe vortex system. At this Reynolds number, a clear horseshoe vortex is formed, moving around the cylinder, before rolling upwards in the wake. The horseshoe vortex

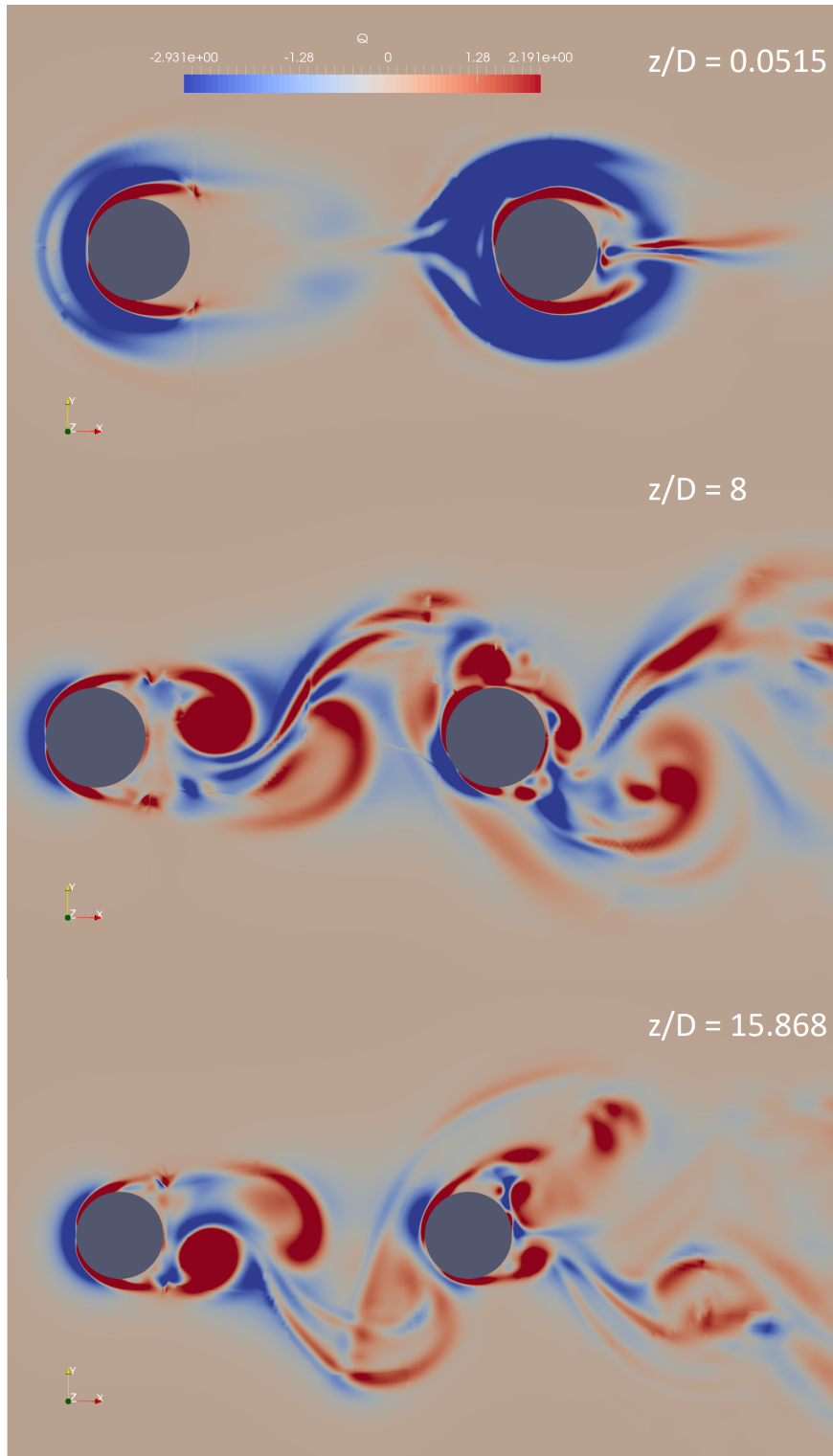


Figure 5.4: Instantaneous vorticity distribution along the span of the cylinders, at the same time instant, visualized by the Q-criterion

in front of the upstream cylinder is also visible in figure 5.4 for  $z/D = 0.0515$ . The downstream cylinder experience a whole other flow picture, which will be shown later, and the instantaneous iso-surfaces show a horseshoe-like vortex structure forming in the front in figure 5.3b. Comparing the two cylinders reveal two distinct structures forming around the cylinders close to the wall. The vortex structure on the downstream cylinder seem to roll up at once, giving it a thicker split horseshoe-like shape.



Looking at figure 5.2, it may seem that hairpin vortices occurs in the wake of the downstream cylinder close to the wall and roughly up to mid-span. This was suggested by Palau-Salvador et al. (2008), as no vortex street develops and no large-scale vortex structures are forming behind the cylinder in this region. This also implies that there are can be no mode A or mode B instabilities in the wake of the downstream cylinder from the junction to its mid-span. Investigating further up, the vortices shed at the end of the cylinders in figure 5.2 can be argued to be similar to mode B instabilities. This is based on the definition by Williamson (1996) and the study on tandem cylinders in free flow by Cao and Wan (2010).

## 5.2 Flow pattern

The flow pattern for two tandem circular cylinders attached to an end-wall develops strong three-dimensional features and coherent vortex structures close to the wall. Seen from figure 4.4, an adverse pressure gradient is present along the wall right in front of the upstream cylinder. This pressure gradient is induced by the surface-mounted cylinder, and causes the flow to separate and hence, create a horseshoe vortex system in the junction of the wall and the upstream cylinder. The Reynolds number of the flow is one of the most important parameters that control the rich coherent dynamics of the vortex (Escalauiaza and Sotiropoulos, 2011). For low Reynolds numbers, the junction flow remain steady and up to three different horseshoe vortices take place (Simpson, 2001). In the calculations by Visbal (1991), one single primary vortex was present for a Reynolds number of 500.

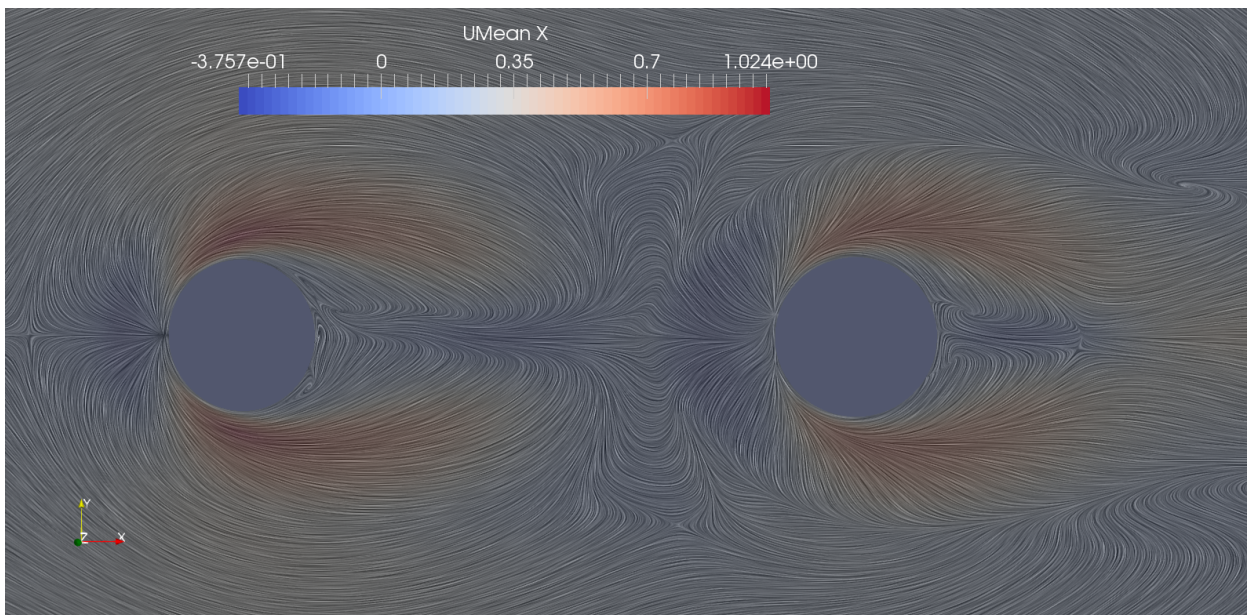


Figure 5.5: Streamlines of mean  $u$ , by SurfaceLIC in x-y-plane for  $z/D = 0.0515$

From the streamlines in figures 5.5, 5.6 and 5.7, and from the vorticity in figure 5.3, it is observed that a vortex is wrapping around each cylinder for  $z/D = 0.0515$ . The w-velocity by UMean Z, indicate an upflow in the near wake, behind both cylinders, which is also seen by the streamlines in the x-z-plane in figure 5.13. This close to the wall, it is also observed that the downstream cylinder experience the flow at a higher magnitude than the upstream one, vindicating the fact that the flow from the upstream cylinder give a more chaotic flow picture on the downstream cylinder.

In figures 5.8, 5.9 and 5.10 at the other end of the cylinder, where  $z/D = 15.868$ , the vortices now shed in a synchronized or parallel matter, which was observed by Zdravkovich (1996) for tandem cylinders in free flow. Seen from figure 2.8, the two circular cylinders in tandem arrangement at

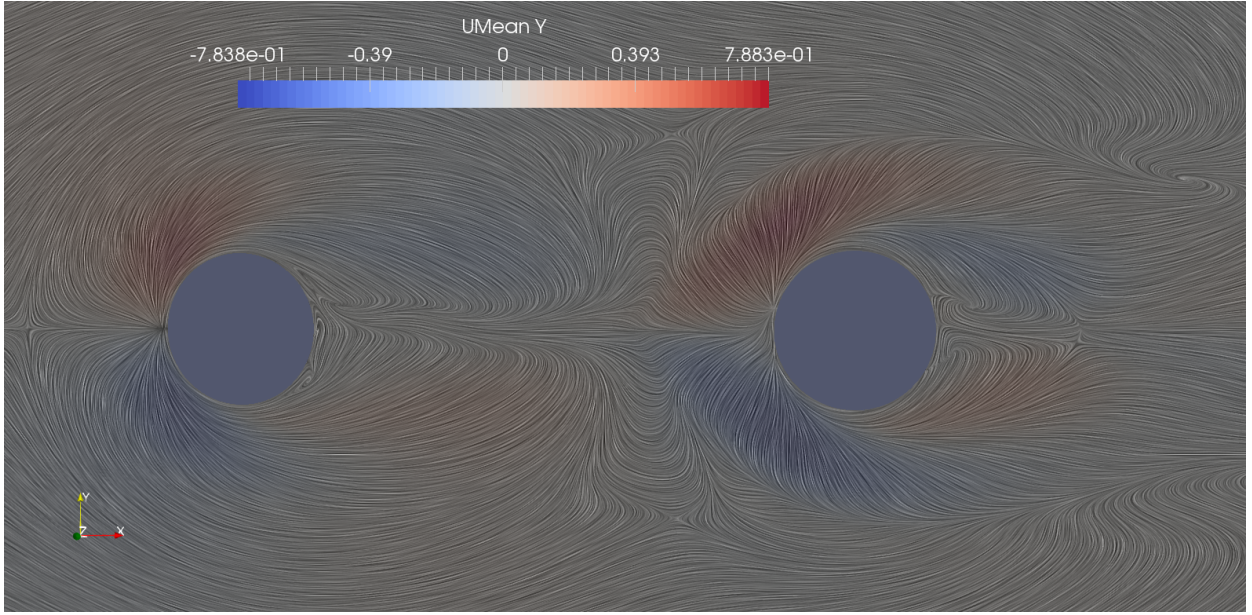


Figure 5.6: Streamlines of mean  $v$  by SurfaceLIC in x-y-plane for  $z/D = 0.0515$

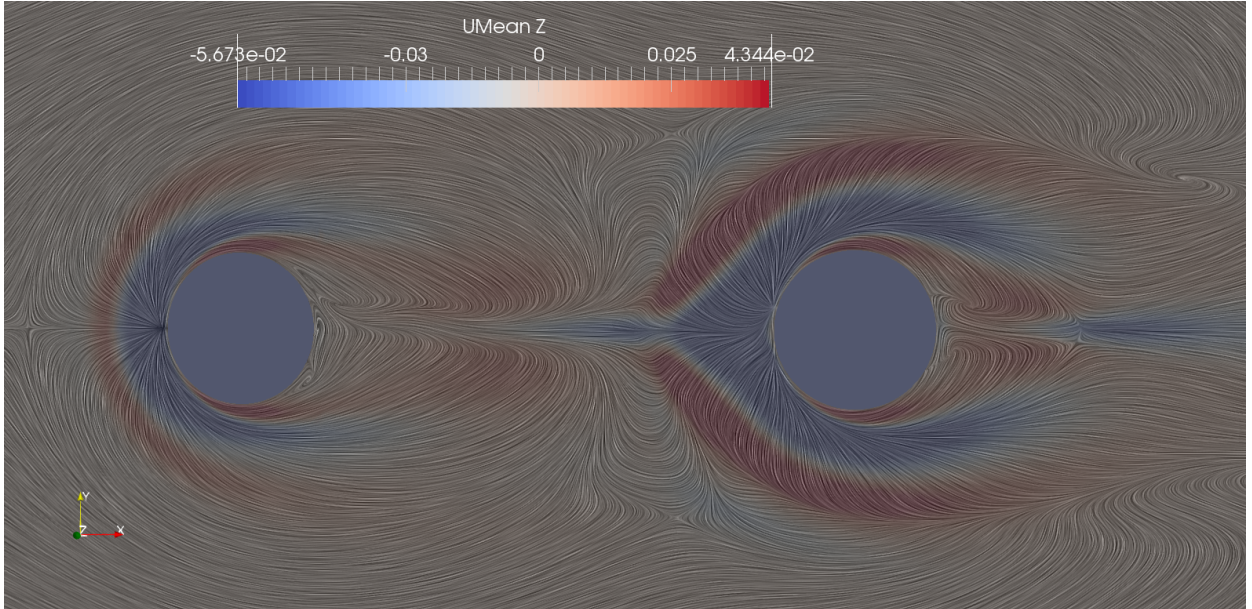


Figure 5.7: Streamlines of mean  $w$  by SurfaceLIC in x-y-plane for  $z/D = 0.0515$

this location, belongs to the coupled eddy shedding regime, W-T(1 + 2). This is where two eddy streets are synchronized in both frequency and phase, which means that the eddies upstream pairs with the downstream ones and form a so called binary eddy street for the co-shedding regime. [Ataie-Ashtiani and Aslani-Kordkandi \(2013\)](#) on the other hand, observed the flow having a co-shedding regime close to the bed, while further up along the cylinder, the reattachment regime was present for a center-to-center spacing of  $S/D = 3$ , as there were no vortex shedding in the gap. It was also observed, that near the bed and within the gap, a reverse flow extended almost to the downstream pier. This is not the case in the present study, as the reverse flow only extends to about half the gap spacing. In this region, the vortex shedding is quite suppressed. Further down the cylinder, near the end at  $z/D = 15.868$ , pattern  $F$  from [Igarashi \(1981\)](#) classification can be recognized, based on the center-to-center spacing in this study  $S/D = 4$ . The shear layers rolls up in front of the downstream cylinder in an alternating way, making the gap flow very significant.

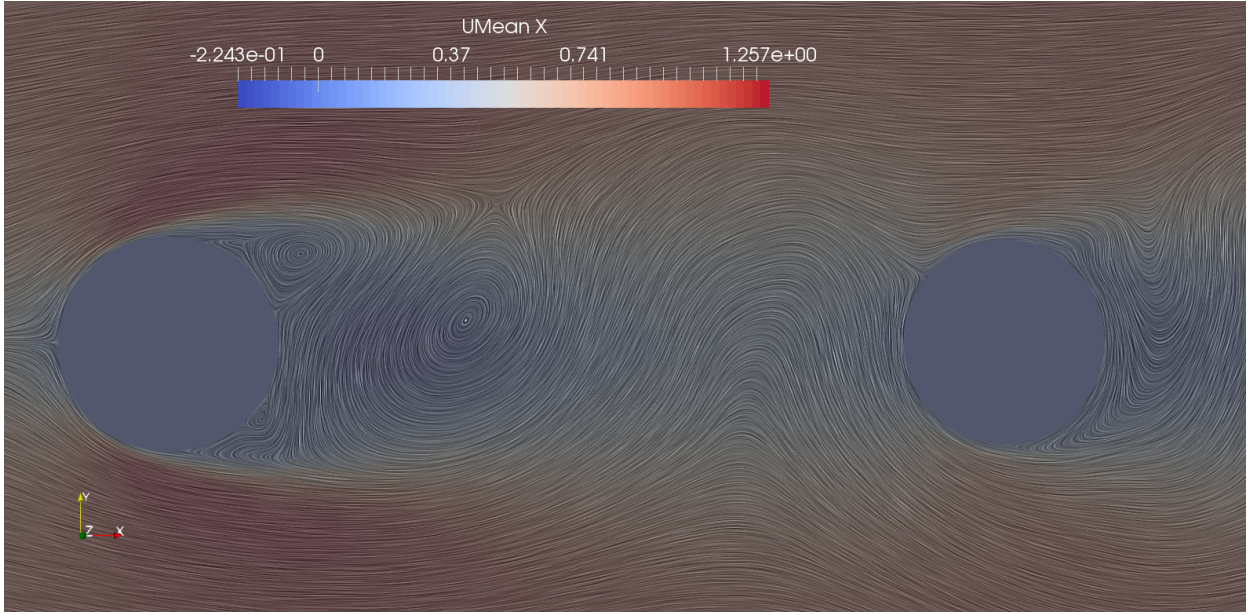


Figure 5.8: Streamlines of mean  $u$  by SurfaceLIC in x-y-plane for  $z/D = 15.868$

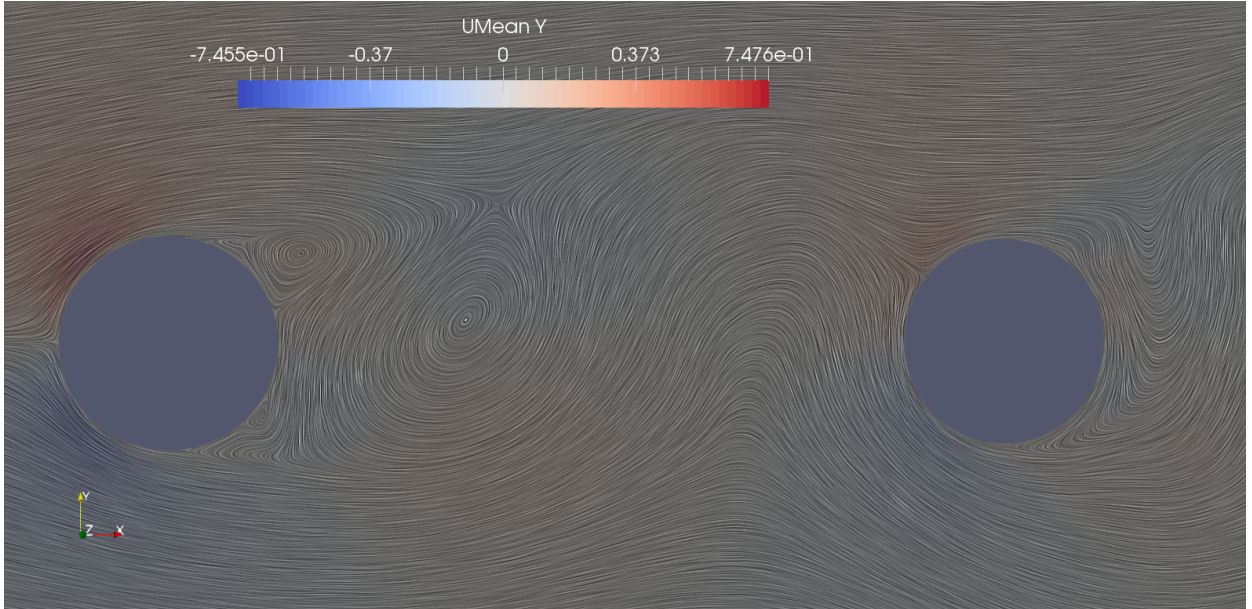


Figure 5.9: Streamlines of mean  $v$  by SurfaceLIC in x-y-plane for  $z/D = 15.868$

From the spanwise location  $z/D = 8$ , shown in figures A.13, A.14 and A.15 in the Appendix, a similar flow pattern to pattern  $E$  in chapter 2.3 is observed. The separated shear layer from the upstream cylinder rolls up intermittently in front of the downstream cylinder, and the flow is bi-stable between patterns  $D$  and  $F$  (Igarashi, 1981).

According to the streamlines in front of the upstream cylinder in figure 5.14a, a downward and reverse flow is present. This is the horseshoe vortex at the base of the upstream cylinder, which is formed in a small region near the wall just upstream of the cylinder. According to Dargahi (1989), the point that is located at the end of the small horseshoe vortex region, is the primary separation point near the wall. This is also seen from the iso-surfaces for  $\lambda_2 = 2$  in figure 5.3a.

Behind the upstream cylinder, an upflow is present all through the gap, influencing the incoming flow on the downstream cylinder. This effect seems to be stronger in the downstream half of the gap compared to the upstream one, which is revealed by figure 5.13 and by the velocity vectors in

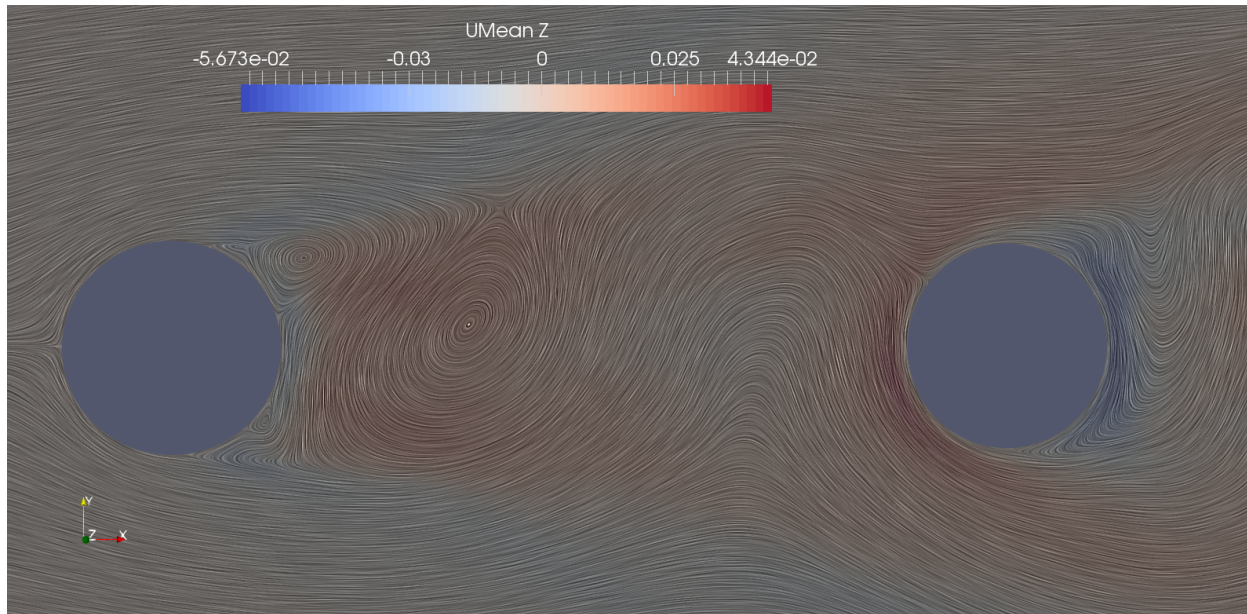


Figure 5.10: Streamlines of mean  $w$  by SurfaceLIC in  $x$ - $y$ -plane for  $z/D = 15.868$

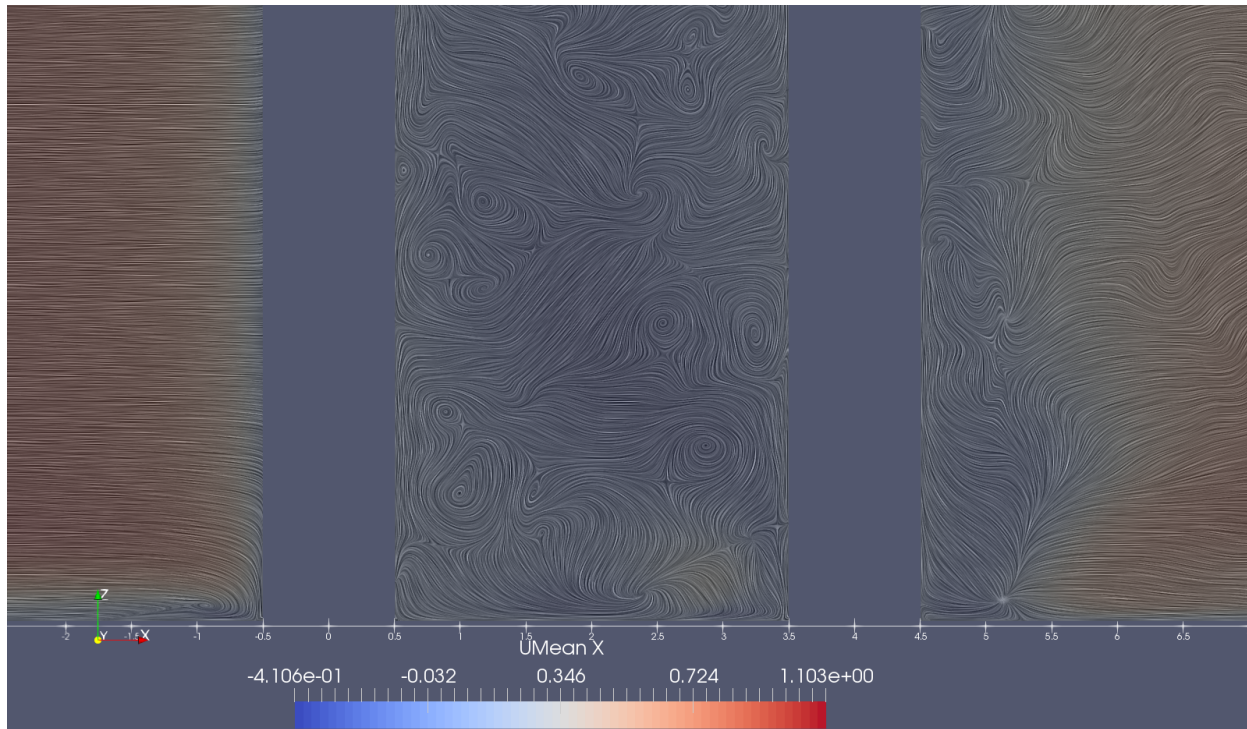


Figure 5.11: Streamlines by mean  $u$  in the  $x$ - $z$ -plane, zoomed in on the junction

figure A.16 in the Appendix.

Figure 5.14b show the streamlines in front of the downstream cylinder, where a small recirculation zone is present. The velocity contours along the  $x$ - $z$ -plane, further illustrates this zone, shown in the Appendix, figure A.12. However, a downflow by the  $w$ -component of the UMean-velocity in figure 5.13 is observed in front of the downstream cylinder, indicating a similar flow picture as in the front of the upstream cylinder. According to [Ataie-Ashtiani and Aslani-Kordkandi \(2013\)](#), this recirculation zone is associated with the change from the co-shedding regime to the reattachment regime. Hence, the flow structure in front of the downstream cylinder can't be a horseshoe vortex. In this area, the downflow is suppressed due to the formation of the reattachment regime. In the

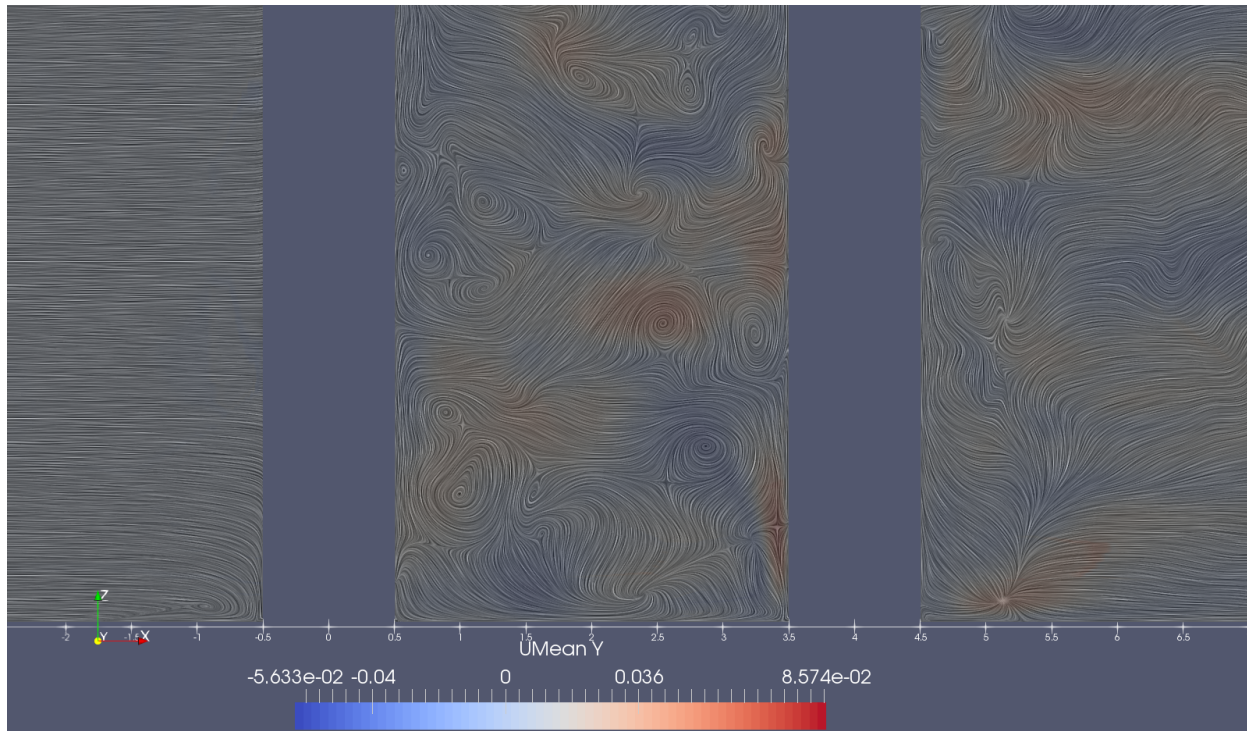


Figure 5.12: Streamlines by mean  $v$  in the  $x$ - $z$ -plane, zoomed in on the junction

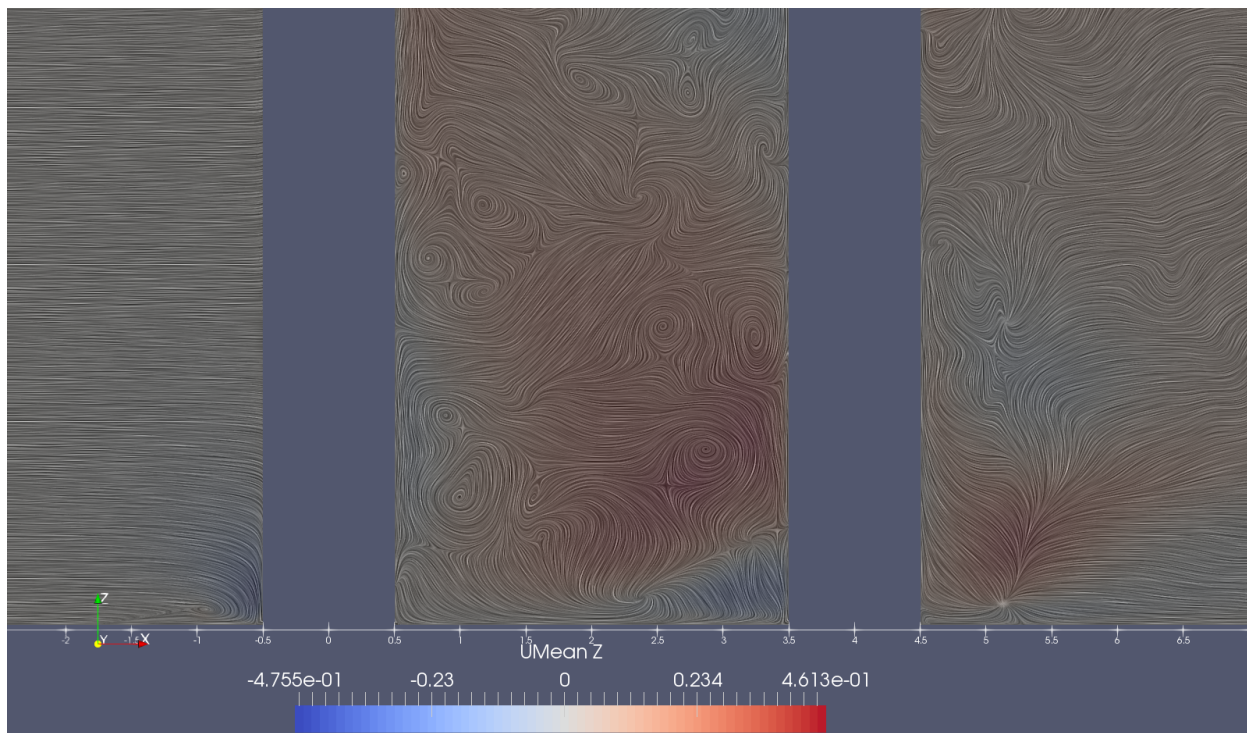


Figure 5.13: Streamlines by  $w$  in the  $x$ - $z$ -plane, zoomed in on the junction

present study, however, a horseshoe-like vortex forms in front of the downstream cylinder and the spacing ratio between the cylinders indicate a co-shedding regime. This means the gap flow is significant for the flow around the downstream cylinder, which is not the case for [Ataie-Ashtiani and Aslani-Kordkandi \(2013\)](#).

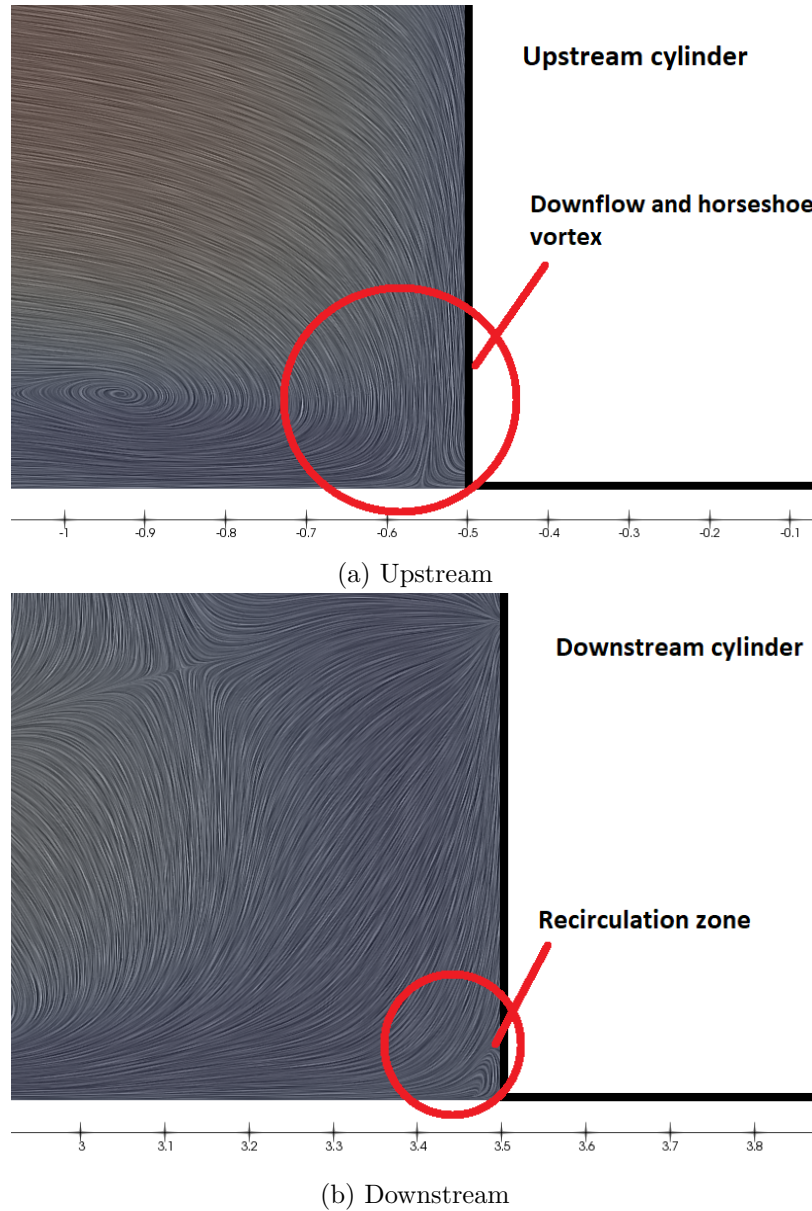


Figure 5.14: Magnification of the flow feature upstream of each cylinder, coloured by mean  $u$ -component of  $U$

### Wake flow

The wake is very important to investigate, as the influence of two cylinders and a wall will have prominent effects. Figure 5.15 and 5.16 shows the time- and space averaged  $u$ -component velocity in the wake behind each cylinder, compared to the case of a single wall-mounted cylinder. The  $x$ -axis represents the distance from the center of the upstream and downstream cylinders, respectively. The  $y$ -axis represents the normalized velocity  $u/U$ , where  $U$  is the free stream velocity with value 1.0.

First, by looking at figure 5.15 for  $z/D \approx 16$ , the upstream cylinder have a huge effect on the  $u$ -velocity on the downstream cylinder. At this spanwise location, the effect from the wall on the flow is considered negligible, which is briefly discussed in chapter 4. Figure 5.15 show that the velocity of the upstream cylinder quickly decrease towards 0, right in front of the downstream cylinder at  $x/D = 3.5$ . A single cylinder however, will increase further and have a stabilized  $u$ -velocity of around  $u/U = 0.8$ . Discrepancy between the single and upstream cylinder is thereby likely to

occur in the gap region, due to the lower u-velocity.

The downstream cylinder, however, develops a similar profile as the single cylinder. From figure 5.15, it is observed that the downstream cylinder develops this profile at a different pace, at it seems to use a longer distance behind the cylinder to stabilize. After a distance of approximately  $10D$ , the single cylinder converges, while the downstream cylinder takes more than  $20D$ . There will be some discrepancies between the results of the downstream cylinder compared to the single one, especially in terms of values.

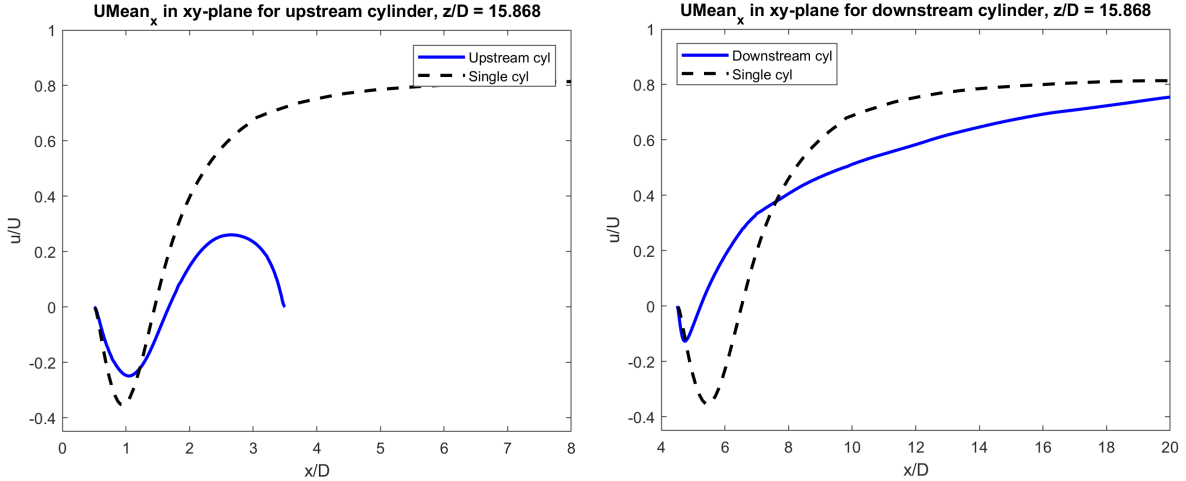


Figure 5.15: Normalized velocity profiles of mean  $u$  at  $z/D \approx 16$

Figure 5.16 show the same mean  $u$ -velocity distribution as in figure 5.15, but for a different spanwise location,  $z/D = 0.0515$ . The normalized velocity  $u/U$  seems to oscillate in the wake behind the upstream cylinder, having a non-positive velocity throughout the gap between the cylinders. This will slow down the flow velocity in  $x$ -direction, influencing the incoming flow on the downstream cylinder.

The downstream cylinder experience a similar mean  $u$ -velocity distribution as for the single cylinder, but at a lower magnitude. It experience a small drop before increasing and stabilizing close to a value of  $u/U = 0.2$ , while the single cylinder experience a stabilizing velocity in the wake of  $u/U \approx 0.4$ . This means the downstream cylinder experience a  $u$ -velocity magnitude half of what the single cylinder does. This is mainly caused by the tandem configuration, where the gap flow decrease the incoming velocity on the downstream cylinder.

Comparing the two wakes occurring after the upstream cylinder at  $z/D = 0.0515$  and for  $z/D \approx 16$  in figures 5.15 and 5.16, there are some major differences. In the immediate wake, the  $u$ -velocity is negative and have a somewhat similar curve as the single cylinder. Closer to the downstream cylinder, the difference between the two curves become apparent. For both locations,  $u/U$  for the upstream cylinder goes towards zero, which indicate a stagnation point in front of the downstream cylinder. However, near the wall, at  $z/D = 0.0515$ , there is a non-positive  $u$ -velocity in the whole gap, while at the other end of the cylinder, a positive velocity is present. This difference may be attributed to the horseshoe-like vortex occurring in front of the downstream cylinder, close to the wall.

The wake of the downstream cylinder is clearly affected at both locations, as seen in figures 5.15 and 5.16. Comparing the wakes of the downstream cylinder at  $z/D = 0.0515$  and  $z/D \sim 16$ , it is observed that the stabilizing behaviour is different. For the downstream cylinder in figure 5.15, at  $z/D \approx 16$ , the  $u$ -velocity seems to converge slowly towards the same level as for a single cylinder, but for  $z/D = 0.0515$  the velocity quickly stabilizes at 0.2, half of  $u/U$  for the single cylinder. This effect may also be due to the aforementioned horseshoe-like vortex, as the incoming flow to

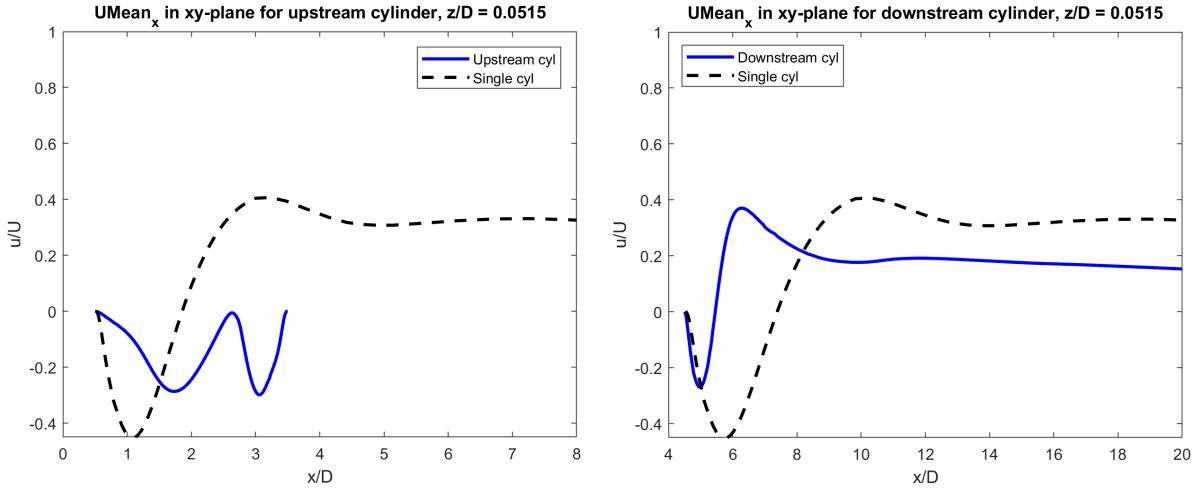


Figure 5.16: Normalized velocity profiles of mean  $u$  at  $z/D = 0.0515$

the downstream cylinder from the upstream one has a negative or almost stagnant velocity  $u/U$ .

The normalized velocity profiles for mean  $u/U$  are plotted along the  $y$ -axis at a distance  $0.6D$  behind the cylinder centers in figures 5.17 and 5.18. The  $x$ -axis now describes the distance in  $y$ -direction of where the line sampling have been performed. The lines are shown in figure 5.19. There is a noticeable difference in the profiles between the upstream and downstream cylinder, at both spanwise locations,  $z/D = 0.05$  and  $z/D = 16$ .

From figure 5.17, it is observed that the downstream cylinder have less of a decrease in velocity than the upstream one. This is due to the more chaotic flow present in the gap in front of the downstream cylinder, causing the flow to spread over a larger transverse span in  $y$ -direction. The upstream cylinder experience a higher peak value than the downstream cylinder, which could be explained by the vortices diminishing after being shed from the upstream cylinder. For  $z/D \approx 16$ , this phenomenon is illustrated by figure 5.19a.

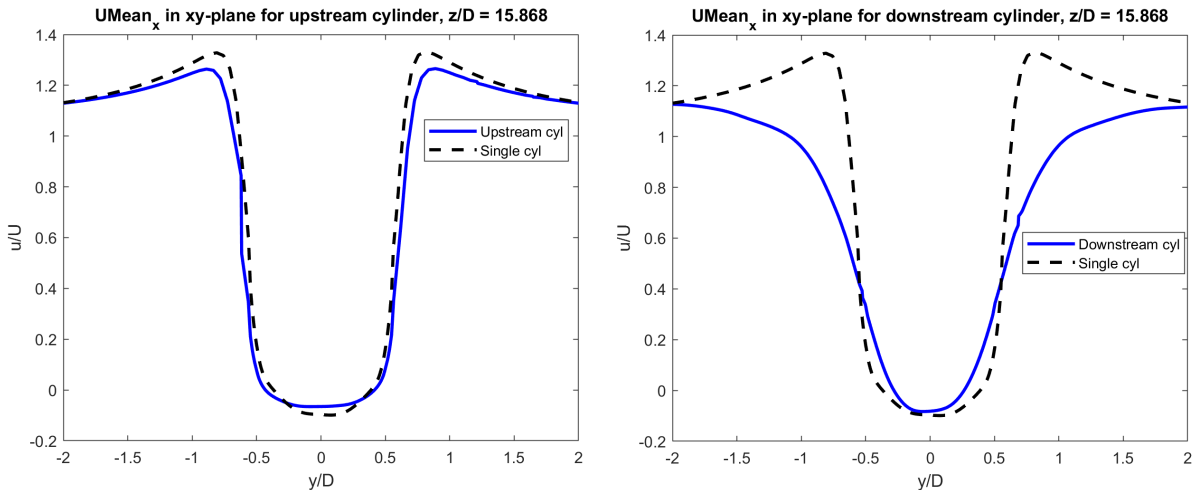


Figure 5.17: Normalized velocity profiles of mean  $u$  in the wake behind the cylinders for  $z/D \approx 16$

Figure 5.18 represents the mean  $u$ -velocity distribution along the  $y$ -axis for  $z/D \approx 0.05$ . From the velocity distribution, the upstream cylinder seems to have a slightly higher peak in the gap than the downstream cylinder. It can also be seen that the downstream cylinder experience a small negative value in the wake at the center line, which coincides nicely with the single cylinder case.



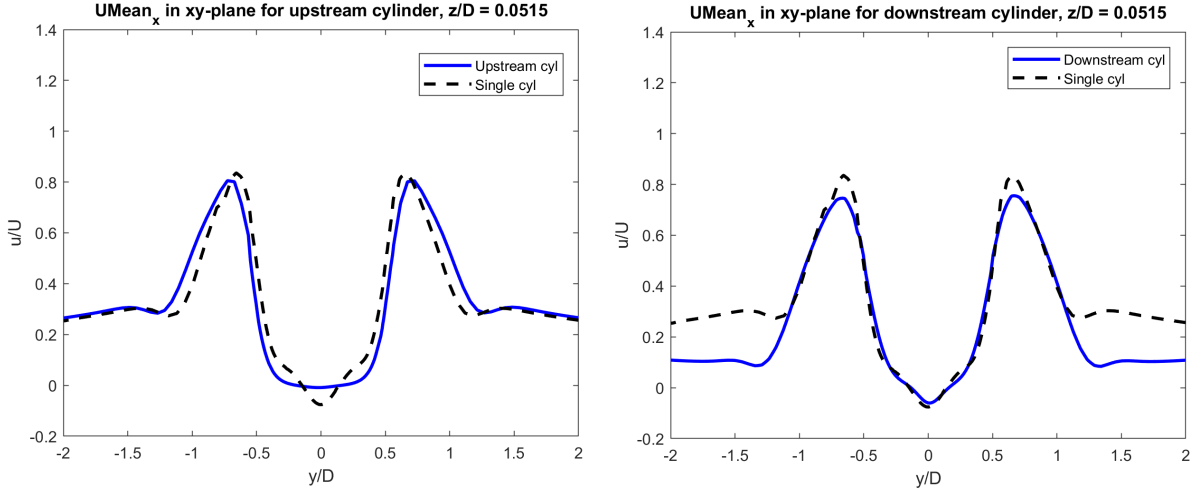


Figure 5.18: Normalized velocity profiles of mean  $u$  in the wake behind the cylinders for  $z/D = 0.0515$

The major difference is the magnitude of the  $u$ -velocity, as it is lower for the downstream cylinder. The downstream cylinder is influenced by the wake of the upstream cylinder, and the incoming velocity is thereby lower, as mentioned earlier. Both the upstream and downstream cylinder in these plots seems to coincide with the contours of the  $U_{mean}$ -illustration for  $z/D = 0.0515$  in figure 5.19b.

Figures A.9 and A.10 in the Appendix show the time- and space-averaged  $v$ -component of the velocity in the wake behind each cylinder. At  $z/D \approx 16$ , the velocity distribution show a similar shape to the single cylinder velocity distribution for both upstream and downstream cylinders. The major difference is that the upstream cylinder have a slightly lower value near the mid-wake, and higher elsewhere. The downstream cylinder seems to experience a flow with a more smooth, oscillating  $v$ -velocity compared to the single cylinder close to the mid-wake.

The mean  $v$ -velocity distributions at  $z/D = 0.0515$  is quite different. Both the upstream and downstream show similarities with the shape of the single cylinder distributions. The upstream cylinder seem to have a lower valued distribution while the downstream cylinder experience a much higher mean  $v$ -component, giving it a higher drop and a higher amplitude at the top and bottom of the sample line, compared to the single cylinder.

For both  $z/D$ , the mean  $v$ -velocity distributions seem to follow the same overall trend as the single cylinder. The extreme values have almost the same locations, but different amplitudes compared to the single cylinder.

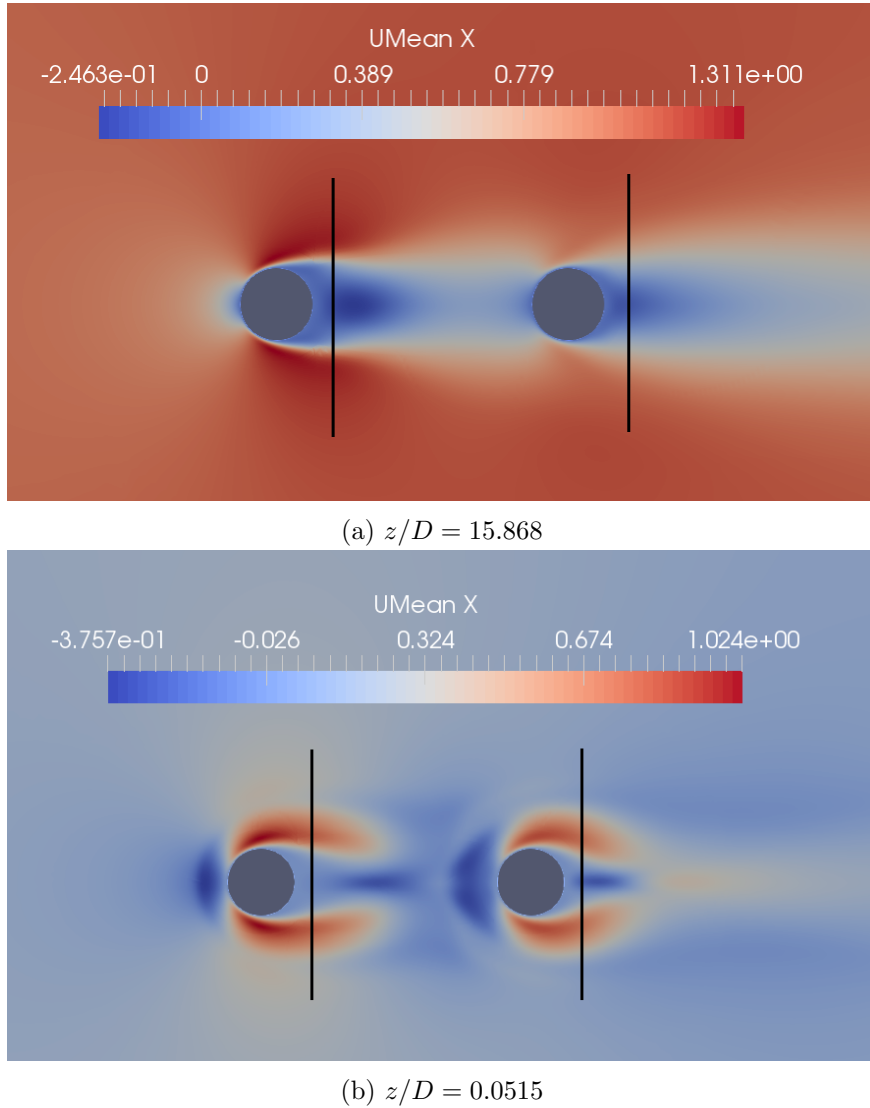
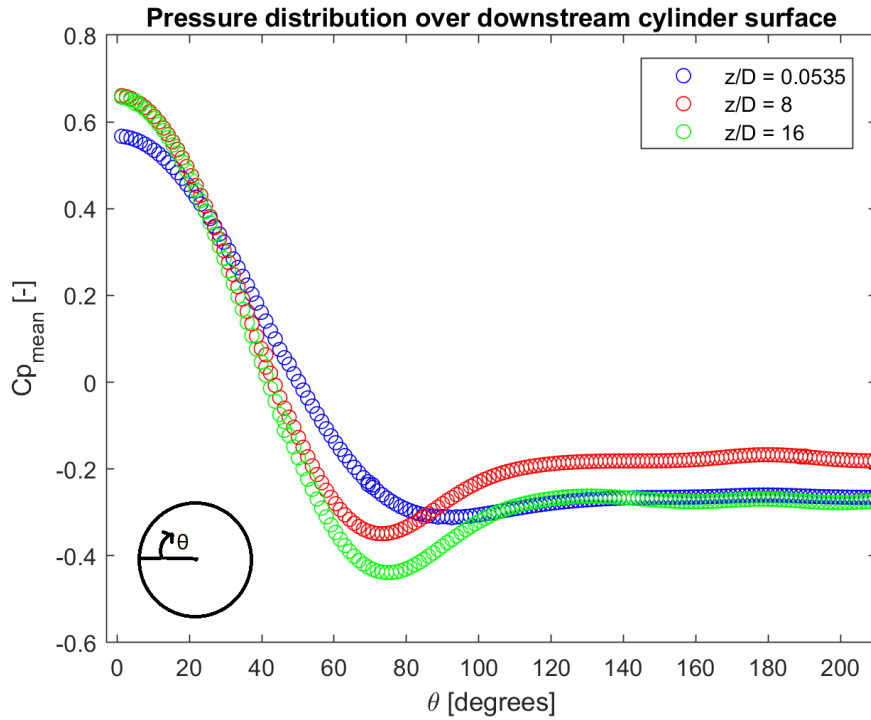


Figure 5.19: Illustration of the location of the sampling lines for the mean velocity in x-y-plane,  $0.6D$  from the cylinder center

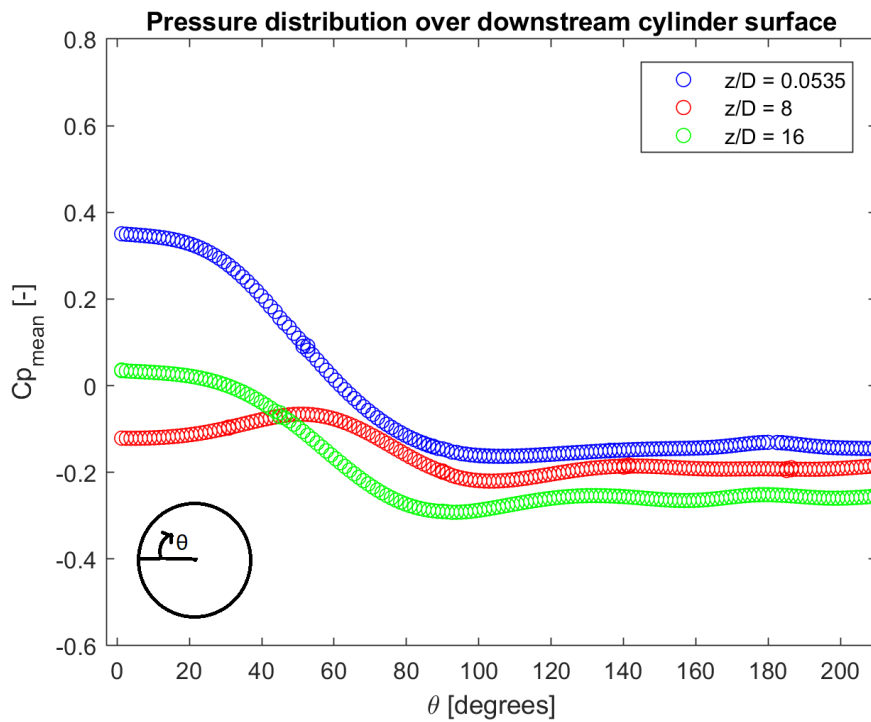
### 5.3 Pressure distribution

The distribution of pressure along both cylinder surfaces are plotted in figure 5.20. The figures show how the pressure varies along the surface of each cylinder at three different spanwise locations. The upstream cylinder in figure 5.20a show similarities with the pressure distribution for the single cylinder case in figure 2.15. The pressure distribution near the wall is lower than further away, and shows a more flattened curve at approximately  $100^\circ$ . This is mainly due to the friction from the wall, which is causing the flow to move towards the junction between the upstream cylinder and the wall, and contributes to forming the horseshoe vortex system. At  $z/D \approx 16$ , the pressure distribution show a maximum pressure coefficient of approximately 0.67, in front of the upstream cylinder, indicating a laminar separation of flow. Near the wall however, at  $z/D \approx 0.05$ , the maximum  $C_p$  is approximately 0.59, slightly lower compared to the other end of the upstream cylinder.

Figure 5.20b represents the pressure distribution for the downstream cylinder, who experience quite a different pressure distribution. The maximum pressure coefficient occurs near the wall at  $z/D \approx 0.05$ , with a value of  $C_p \approx 0.38$ . It shows a pressure distribution similar to the one of a single cylinder, but flattens out at approximately  $90^\circ$ . This indicate, in coherence with the streamlines



(a) Upstream

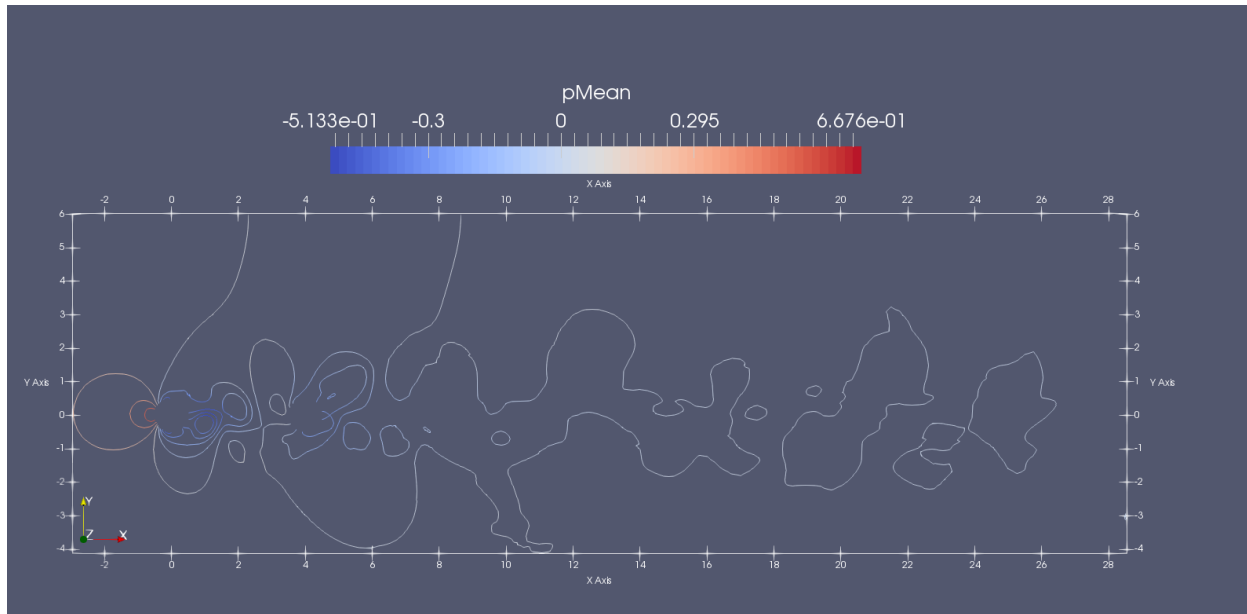


(b) Downstream

Figure 5.20: Pressure distribution over the two circular tandem cylinders

in figure 5.7, that the flow moves upwards in the wake due to the horseshoe-like vortex forming in front of the downstream cylinder. According to Igarashi (1981), the pressure distribution has this shape due to the separated shear layers rolling up in front of the downstream cylinder for a spacing  $S/D$  above the critical spacing of 3.5.

A similar, but less distinct curve is seen for  $z/D \approx 16$ , where  $C_p$  is close to 0. The pressure



(a) Viewing the whole range of contours, where  $x = -3$  to  $28.5$  and  $y = -4$  to  $6$ .



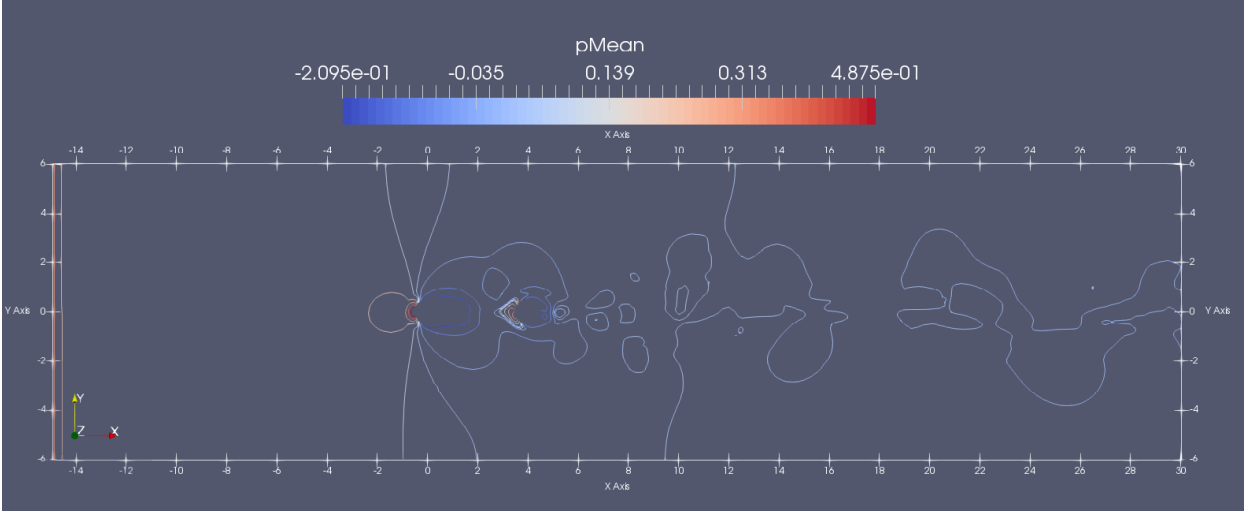
(b) Zoomed in on cylinders

Figure 5.21: Pressure contours at  $z/D \approx 16$

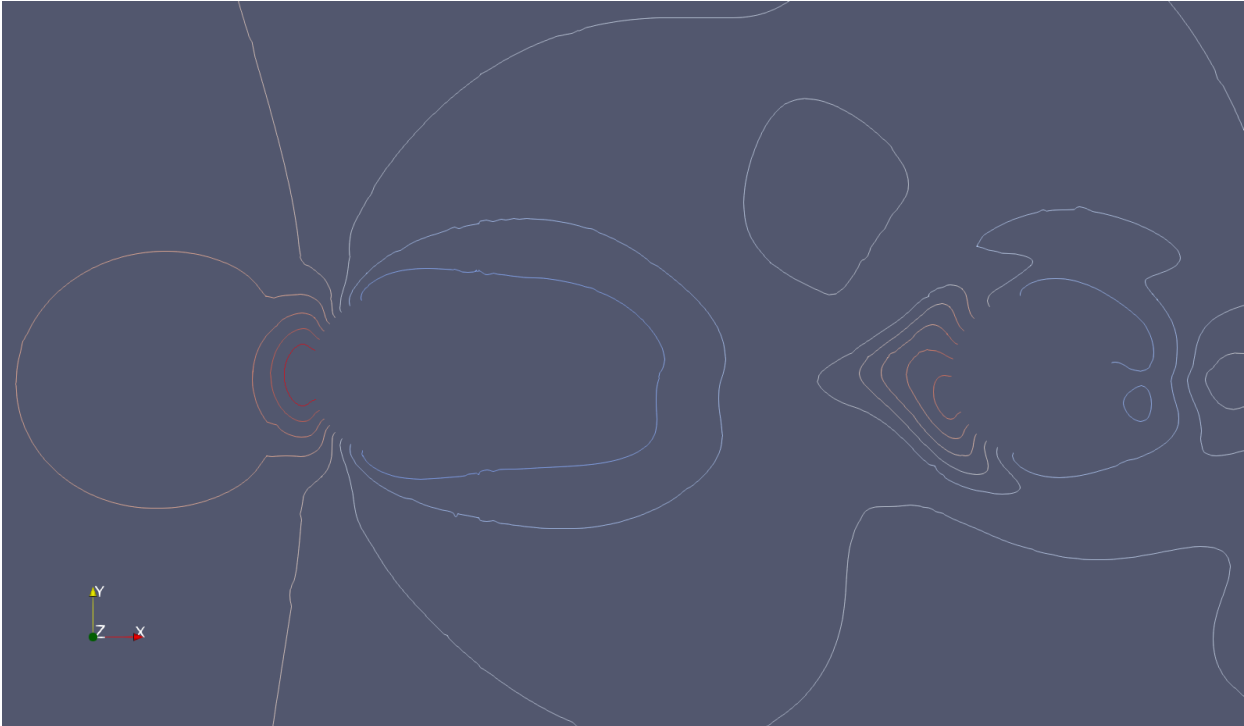
distribution at this location show compatible curves with [Igarashi \(1981\)](#) studies at a much higher Reynolds number. The shape of the curves are similar, and the current values of the pressure distributions for both the upstream and the downstream cylinders are slightly lower.

At  $z/D = 8$ , however, there is a slightly negative  $C_p$  of approximately  $-0.1$  near the front stagnation point of the downstream cylinder. The maximum  $C_p$  is found at approximately  $60^\circ$  with a value of  $-0.05$ , before the curve decreases and have a minimum at  $100^\circ$ . It may seem from the streamlines in figure [A.13](#) in the Appendix, that there is a reattachment flow onto the downstream cylinder. This may explain the pressure distribution according to [Igarashi \(1981\)](#), who observed for spacing's lower than the critical spacing, that the downstream pressure distribution had a more

distinct curve than the distribution at  $z/D = 8$  in this case. Igarashi (1981) also observed for a spacing of 1.03, that no sign of a reattachment peak was present, which indicate that the shear layers do not reattach onto the downstream cylinder. The peak of the curve for  $z/D = 8$  is not very high, so this might be an effect due to the upflow coming from the presence of the wall. At  $100^\circ$ , the flow in figure A.3 seem to separate from the downstream cylinder, which is indicated by the minimum pressure here.



(a) Viewing the whole range of contours, where  $x = -15$  to  $30$  and  $y = -6$  to  $6$ .



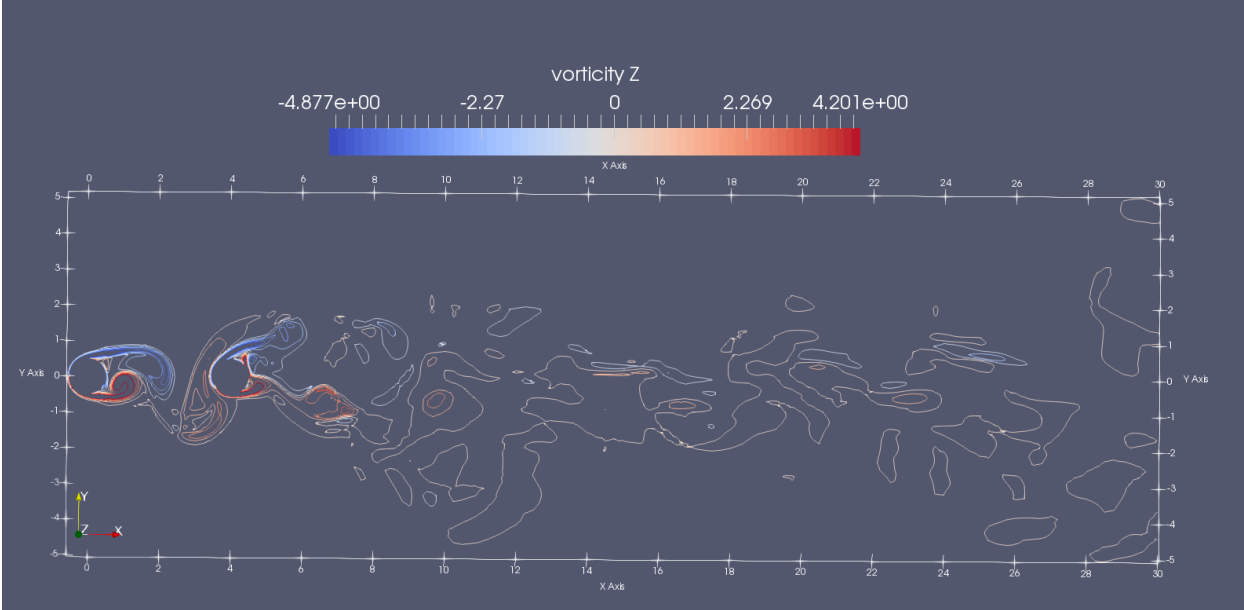
(b) Zoomed in on cylinders

Figure 5.22: Pressure contours at  $z/D = 0.0515$

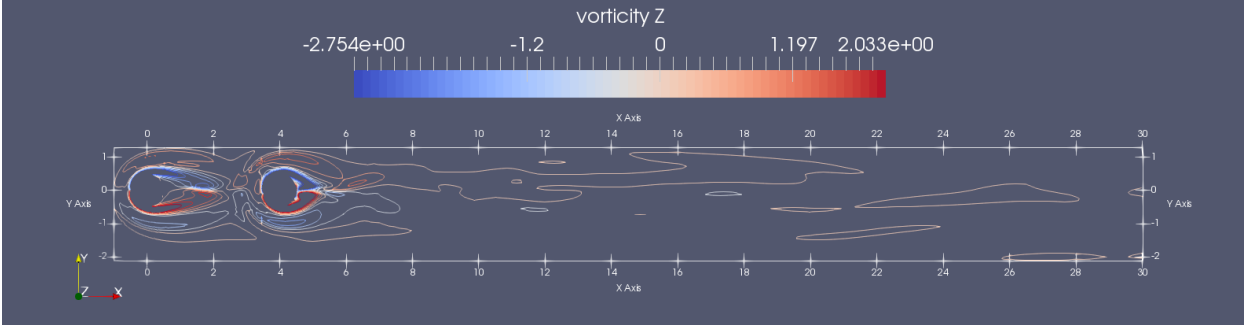
There are not many results available for the distribution of pressure along the downstream cylinder. The author of this thesis has not been able to find suitable literature with comparable results for flow around wall-mounted tandem cylinders at low Reynolds numbers, so the results are merely compared to single cylinder cases.

The pressure contours in figure 5.22 show good symmetry and lines, indicating that the grid is sufficiently refined close to the wall and near the cylinders. However, from figures A.8 in the

Appendix, further down the cylinder length, the lines show some disturbance. For  $z/D = 8$ , the symmetry in the contours is good, but the outer wake between the cylinders and in front of the upstream cylinder, some small disturbances in the contours are present. This is likely to be caused by defined grid lines in the domain, and the fact that the mesh is getting coarser towards the end of the cylinders. Further down the cylinder, at  $z/D \approx 16$ , the mesh is much coarser than near the wall, and the contours show some disturbance in the outer wake between the cylinders, as shown in figure 5.21. However, there is still quite good symmetry on the contours at this level.



(a)  $z/D \approx 16$ , where  $x = -1.3$  to  $30$  and  $y = -5.1$  to  $5.1$ .



(b)  $z/D = 0.0515$ , where  $x = -1.6$  to  $30$  and  $y = -2.1$  to  $1.2$ .

Figure 5.23: Vorticity contours at two spanwise locations

Vortices shed from the cylinders travels down the wake before they blend in with the free flow some distance away from the obstacle. In the pressure contours above, areas of minimum pressure indicate a vortex being present. The pressure contours for  $z/D \approx 16$  show an area of minimum pressure around  $x/D = 2 - 4$ , which is verified through vorticity contours in figure 5.23a. There is more vorticity present at  $z/D = 15.868$  than near the wall, indicating the suppression of vortices here, as mentioned earlier. There is some contours showing minimum pressure regions for  $z/D = 0.0515$ , which is seen in the vorticity contours in figure 5.23b. However, the intensity of the contours are far less than further down the cylinders.

## 5.4 Forces

The time history of the force coefficients are shown in figures 5.24 and 5.25 for both cylinders. As seen from the lift coefficient in figure 5.24, there are large variations of the lift coefficients in time. This clearly show the importance of having simulations with a long duration, in order to get sufficient time-averaged results. With time averaging, the large variations in the amplitudes will fade out.

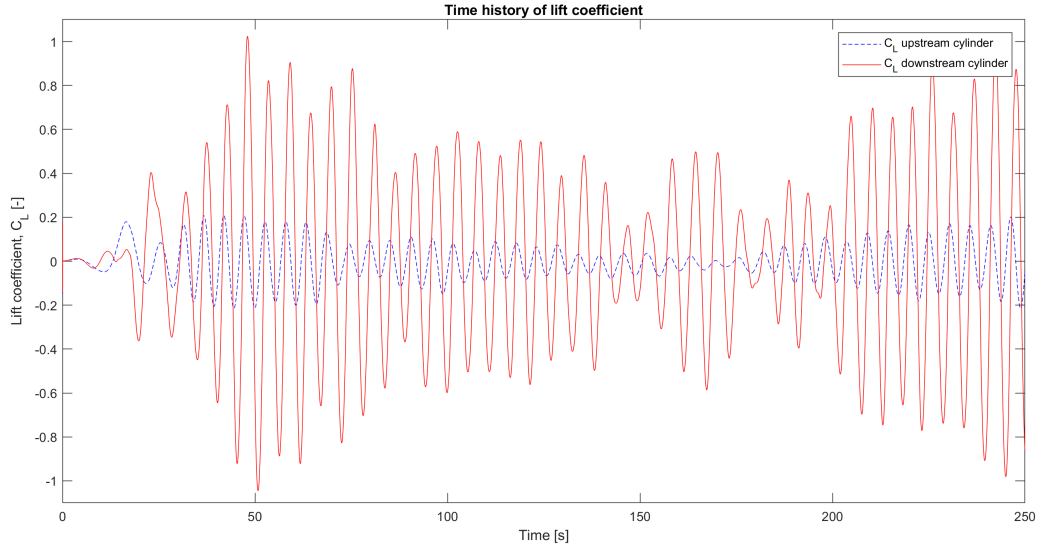


Figure 5.24: Time history of lift coefficient,  $C_L$ . Blue line: Upstream. Red line: Downstream.

The time history of the lift coefficient for the upstream and downstream cylinders in figure 5.24, show how the lift force oscillate periodically with a varying amplitude. Both cylinders have a lift coefficient oscillating around 0, coinciding with basic theory of flow around a single cylinder in chapter 2.2. However, the oscillating amplitude is much larger for the downstream cylinders compared to the upstream one. From table 5.2, the RMS value of the lift coefficient for the downstream cylinder is observed to be almost four times the RMS value of the upstream one. This is due to the more disturbed flow onto the downstream cylinder compared to the laminar flow onto the upstream cylinder. As mentioned in chapter 5.1, the impingement upon the downstream cylinder from the upstream one, in addition to the synchronized vortex shedding, cause the large forces acting on the downstream cylinder (Zdravkovich, 1996).

The time history of the drag coefficient for both cylinders is shown in figure 5.25. It is observed that the drag coefficient for the downstream cylinder have a huge drop in value, compared to the upstream drag coefficient. The upstream cylinder oscillates periodically around a mean value of 1.0096, while the downstream cylinder oscillates around 0.4057. The drop in value is mainly due to the presence of the downstream cylinder, and the effect is reported for tandem cylinders in infinite fluid as well, e.g. Kitagawa and Ohta (2008) and Cao and Wan (2010).

In addition to the huge drop in the mean value, the downstream cylinder experiences a larger amplitude. Cao and Wan (2010) seems to coincide with the present results, where the upstream cylinder experience a larger mean drag value and a huge drop for the downstream cylinder. The RMS of the lift coefficients also agrees well, where the upstream cylinder have a much smaller amplitude than the downstream one. This is also reported by Kitagawa and Ohta (2008) for a spacing  $L/D$  of 4, where the fluctuations of lift and drag coefficients were larger than for smaller spacings, due to the fact that the center-to-center spacing was large enough for vortices to be shed from the upstream cylinder. It also seems like the presence of the wall interferes with the drag

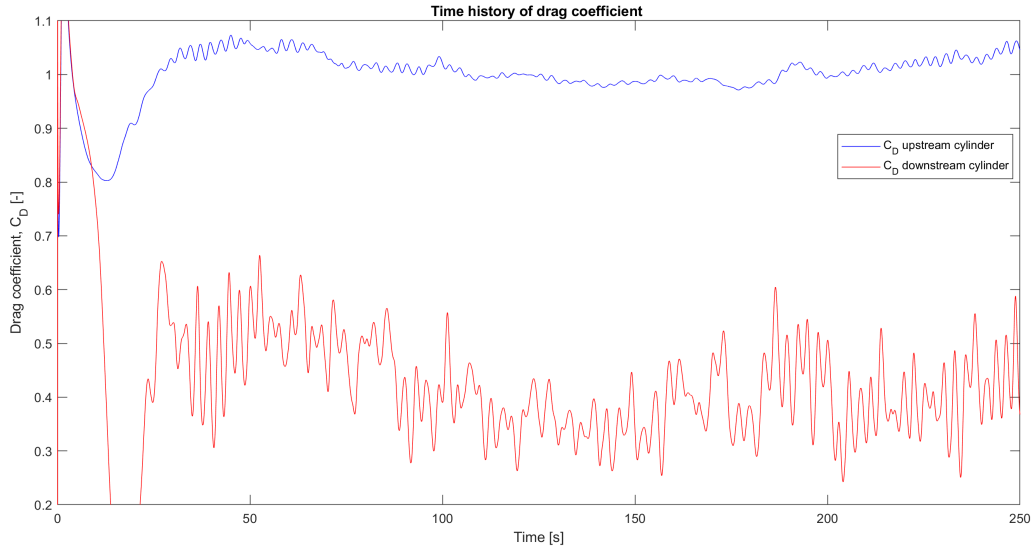


Figure 5.25: Time history of drag coefficient,  $C_D$ . Blue line: Upstream. Red line: Downstream.

and lift coefficients, as the value of the downstream cylinder is much smaller than for the case of tandem cylinders in free flow from [Cao and Wan \(2010\)](#) and [Kitagawa and Ohta \(2008\)](#).

The mean values and RMS of the drag and lift coefficients are presented in table 5.2. The present study is presented together with results from other studies regarding two tandem cylinders in free flow, and a single cylinder fixed to a plate. Not many studies have focused on the forces acting on the cylinders, hence the comparison with cases similar in one way or another to the present study.



Table 5.2: Mean and RMS of drag and lift for different studies

Study	$Re$	$\bar{C}_D$	$C_D^{RMS}$	$C_L^{RMS}$
Satpathy et al. (2011) - Single wall-mounted	200	1.45	-	$\pm 0.67$
Aarnes et al. (2018) - Single wall-mounted	350	1.47	-	-
Present study - Single wall-mounted	500	1.178	0.0248	0.1841
Cao and Wan (2010) - Tandem	300			
Upstream		0.9757	-	0.0163
Downstream		-0.1125	-	0.3896
Igarashi (1981) - Tandem	$3.55 \cdot 10^4$			
Upstream		1.3	-	-
Downstream		0.45	-	-
Kalvig (2015) - Tandem	13100			
Upstream		1.1615	-	0.49
Downstream		0.48	-	0.98
Kitagawa and Ohta (2008) - Tandem	$2.2 \cdot 10^4$			
Upstream		1.2	0.09	0.5
Downstream		0.45	0.34	1.25
Prsic (2016) - Tandem close to plane wall, $G/D = 0.6$	$1.31 \cdot 10^4$			
Upstream		1.07	-	0.47
Downstream		0.53	-	0.4
<b>Present study</b> - Tandem wall-mounted	500			
Upstream		1.0096	0.0211	0.0883
Downstream		0.4057	0.0682	0.4474

## 5.5 Strouhal number

To find the Strouhal number, a probe is placed in the vortex shedding region, writing out results for  $u$ ,  $v$ ,  $w$  and  $p$  at this location for all time steps. With two cylinders, the Strouhal number is found behind both the upstream and the downstream cylinder. Fast Fourier Transform (FFT) is used on the signal from the  $v$ -component of the velocity in the wake behind both cylinders to find the frequency. The probes are located at the coordinates (1, 0.3) and (8, 0.3) in the  $x$ - $y$ -plane, as seen in figure 5.26. The Strouhal number is found at different locations along the cylinder,  $z$ -direction, both at mid-span of the cylinder and close to the wall, as seen in figure 5.27.

The results derived from the FFT-analysis show a clear peak at around 0.08 for the upstream cylinder and around 0.077 for the downstream cylinder. Suppression of the vortex shedding is shown through analyzing the power spectrum sampled along the spanwise length of the cylinder. Earlier, it is shown that the length of the cylinders is very important and that the wall induces

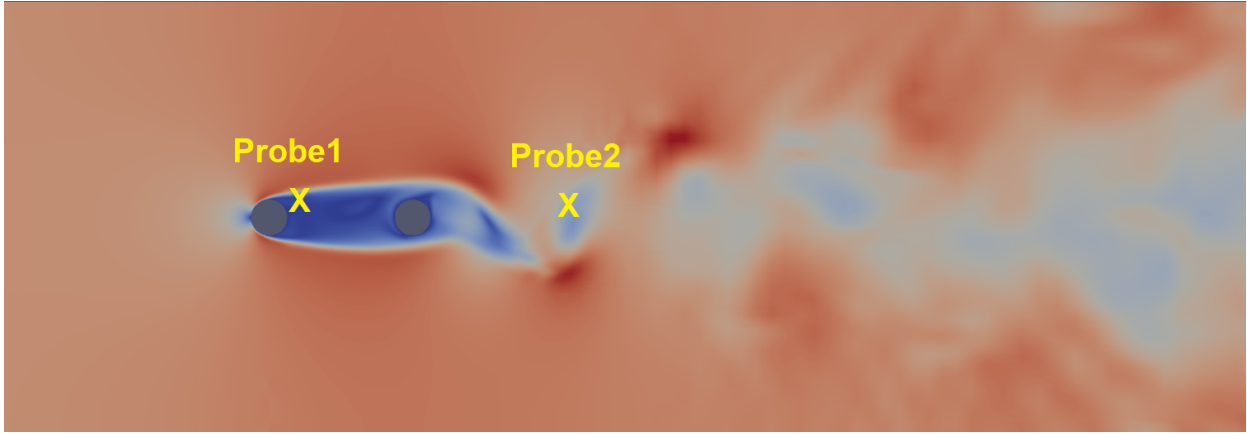


Figure 5.26: Locations of the two probes in the computational domain in the x-y-plane, here visualized with velocity  $U$  magnitude

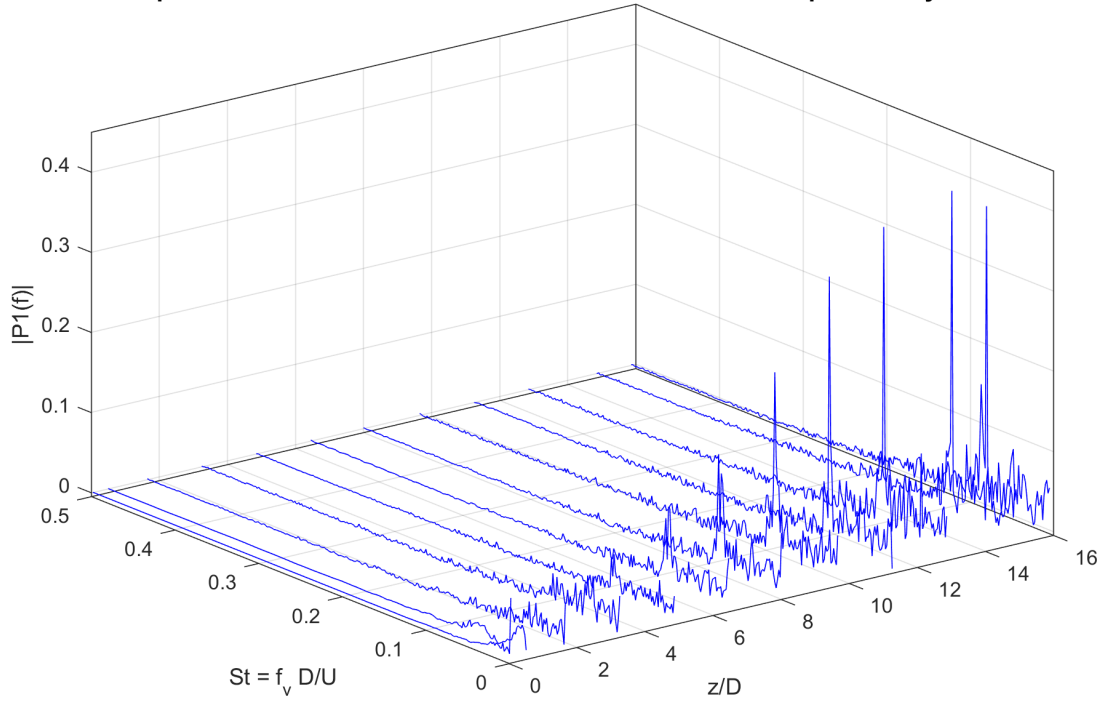
additional effects on the flow around the two cylinders. For both the upstream and downstream cylinder, the amplitudes of the energy spectra in figure 5.27 show a decrease in value, indicating that the vortices shed are influenced by the upflow in the gap between the cylinders. The downstream cylinder also experience lower peaks in general, as the incoming flow on the downstream cylinder is much more disturbed than for the upstream one. It is observed that the signal of the v-component of the velocity for the downstream cylinder show more disturbance compared the upstream cylinder. This is also observed in the power spectrum in figures 5.27, and by the iso-surfaces in figure 5.2.

Along the downstream cylinder, it is also observed that at several  $z/D$ -levels, there are two peaks present, located close to each other. This might indicate an overlap between two different modes of eddy shedding in this region (Zdravkovich, 1996). This further vindicate that the downstream wake is much more chaotic than the upstream one, where only one single peak is present.

Compared with the Strouhal numbers for a single cylinder fastened to an end wall in figure 2.18, the value of the Strouhal number is lower, indicating a decrease in the strength of the vortical structure in the wake of the tandem cylinders. Corresponding with results obtained by Cao and Wan (2010), the Strouhal number has decreased from 0.11 to 0.08. This is mainly due to the interference of having two circular tandem cylinders, but the presence of the end wall might also have an effect. It does however follow the same pattern with respect to the spanwise length of the cylinder, where vortex suppression happens close to the junction between the cylinders and the wall, and the end of the cylinder experience flow similar to free flow. In the single cylinder case, there are more clearly distinguishable peaks towards the free end of the cylinder, compared to the tandem case.

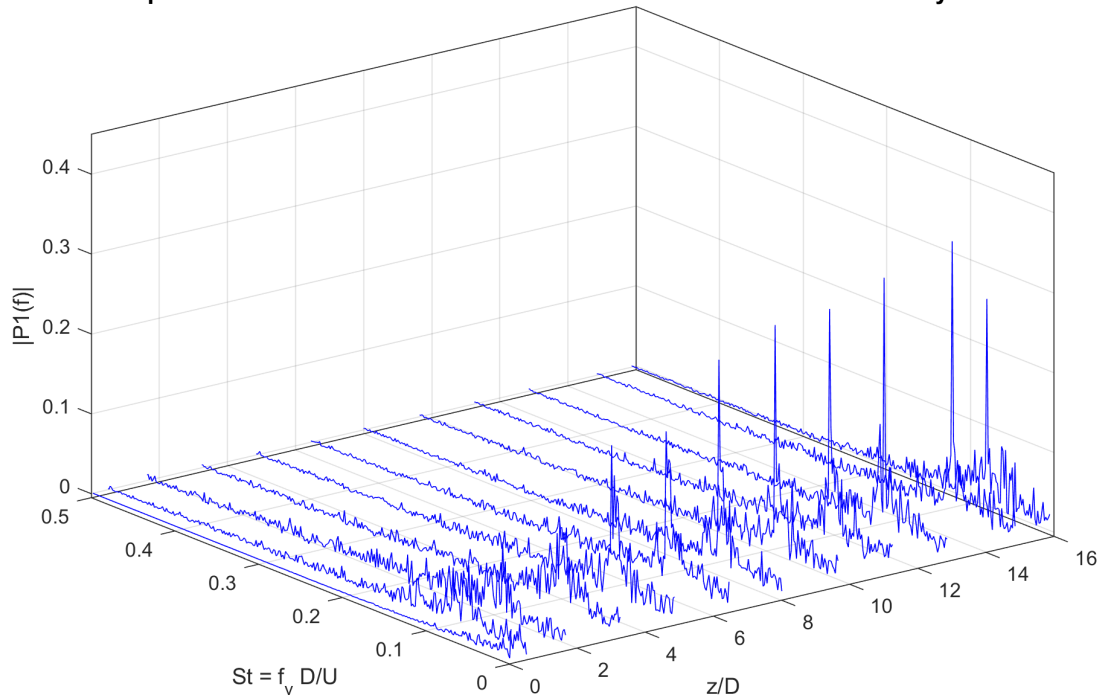
Ataie-Ashtiani and Aslani-Kordkandi (2013) also did a power-spectrum analysis, but for a higher range of Reynolds number from  $10^4 - 3 \cdot 10^4$ . In addition, the power spectrum was calculated using FFT of the auto-covariance function of velocity time-series data, where all three velocity components were taken in. The Strouhal number for the tandem cylinders close to the bed was found to be  $St = 0.116$ , while at mid-span it was found to be  $St = 0.154$ . By looking at figures 5.27a and 5.27b, the same shape as Ataie-Ashtiani and Aslani-Kordkandi (2013) applies to the present study. This means that closer to the wall, the peaks of the energy spectra becomes smaller, and indicate the vortex shedding becoming more and more suppressed, as shown earlier. However, there is a discrepancy for  $z/D = 16$ , where the peak drops a bit compared to  $z/D = 14.85$ . This could be explained by the boundary present here, which is defined as a free slip boundary condition in the computational domain, see chapter 4.2. The boundary is then not free to develop as the rest of the inner domain. It should be therefore noted, that the next grid line should be inspected, but in this case,  $z/D = 14.85$  is sufficient to show how the Strouhal number develops over the cylinder length.

Spanwise variation of normalized Strouhals number for upstream cylinder



(a) Upstream

Spanwise variation of normalized Strouhals number for downstream cylinder



(b) Downstream

Figure 5.27: Energy spectra for various spanwise locations along the cylinder

For the co-shedding regime, close to the wall, the two circular cylinder shed vortices at approximately the same frequency. There are some small differences in Strouhals number between the

Table 5.3: Strouhal number for both cylinders at a selection of spanwise locations

$z/D$	Upstream		Downstream	
	St	$P1(f)$	St	$P1(f)$
16	0.075	0.4	0.075	0.27
14.85	0.08	0.41	0.077	0.35
9.95	0.075	0.23	0.075	0.292
8	0.075	0.145	0.075	0.2
4.85	0.072	0.05	0.075	0.19
1.65	0.03535	0.02	0.075	0.01
0.05	0.01	0.019	0.01	0.22

upstream and downstream cylinders, but this is in coherence with i.e. [Cao and Wan \(2010\)](#) and [Igarashi \(1981\)](#). Closer to the wall, however, the upstream cylinder seems to have a slightly lower Strouhal number than the downstream cylinder for some levels, as seen in table 5.3. This could be explained by the downstream cylinder having a more disturbed incoming flow than the upstream cylinder, causing more chaos in the downstream cylinder wake. The difference between the two cylinders is expected to increase a bit with higher Reynolds numbers, based on theory of tandem circular cylinders in free flow ([Igarashi, 1981](#)).

## Chapter 6

# Discussion

Previous research regarding this topic is not extensive, and in the work with this thesis, finding literature has been an issue. It seems to the author of this thesis that no previous research have been done with the same geometry and flow parameters as this study. The studies that also have two circular cylinders in tandem configuration have been conducted with a much higher Reynolds number, in the turbulent regime, and belongs to the reattachment regime due to the spacing ratio,  $S/D$ , between the cylinders, i.e. [Palau-Salvador et al. \(2008\)](#) and [Ataie-Ashtiani and Aslani-Kordkandi \(2013\)](#). This makes the comparison of results quite hard, because the focus of these articles is mainly on the flow pattern and not the hydrodynamic forces acting on the cylinders. This might be due to the lack of research on the topic, as well as the flow being very interesting and having many new flow features compared to flow around a single cylinder. Many results obtained in this study are based on observations by the author and have been compared to cases regarding single cylinders mounted to a flat plate or two tandem cylinders in free flow.

The articles concerning the topic of this study does not coincide entirely. There are some differences that may explain the discrepancies of the results in the present study when compared to other articles. Both [Palau-Salvador et al. \(2008\)](#) and [Ataie-Ashtiani and Aslani-Kordkandi \(2013\)](#) have a center-to-center spacing ratio of less than the critical spacing defined by [Igarashi \(1981\)](#). This means that both studies belongs to the reattachment regime, while this present study have a larger spacing,  $S/D = 4$ , and belongs to the co-shedding regime. There are however some similarities to the reattachment regime for  $z/D = 8$ , where the streamlines in the x-y-plane show a flow pattern similar to reattachment, and the pressure distribution may seem to show a similar, but very gentle reattachment curve as seen by [Igarashi \(1981\)](#).

Compared to the single cylinder ending on a flat plate, the two tandem cylinders exhibit a very different flow picture. In front of the upstream cylinder a clear horseshoe vortex forms, in coherence with the vortical structure forming around the single cylinder. Around the downstream cylinder, however, a horseshoe-like vortex wraps around it, caused by the chaotic flow coming from the upstream cylinder. Vortices shed from the upstream cylinder impinges upon the downstream one, and the forces acting on the configuration show a big difference in magnitude. The amplitudes of the downstream cylinder of both drag and lift coefficient is much higher compared to the upstream cylinder, mainly due to the impingement of vortices and the synchronized vortex shedding. The pressure distribution for the upstream cylinder also exhibit a similar curve as the single cylinder does, but the downstream cylinder have a whole other distribution. This indicate the incoming disturbed flow, suggesting a change of flow regime between the three locations that are plotted.

The refinement of the mesh is shown in figure [5.1a](#), and due to computational time and memory available, the mesh grid contained 25.2 million elements. Due to the finer grid closer to wall, the elements further out suffered from having more unbalanced rectangular elements, resulting in a coarser distribution at the end of the cylinder domain. This is visualized through the pressure

contours in chapter 5.3, where some disturbances are present in the contour lines at the location of different grid lines. This indicates that the mesh can be further refined in this area, but in this investigation, the main focus was on the area near the wall, thus the mentioned refinement.

The range of Reynolds numbers in the literature study vary from 100 to  $10^5$ , which means that the flow goes from laminar to fully turbulent. Having a Reynolds number of 500 during this investigation, the results are hard to compare. However, some differences are seen for the experimental and numerical articles. The Reynolds number for the experimental studies in this work, show a higher range than for numerical studies. In experimental studies there are always some uncertainty in the measurement equipment, and often very hard to get a perfectly smooth surface. Some roughness will always be present on the model, creating disturbances in the flow, which needs to be taken into account at any Reynolds numbers. Instead, experimental studies often induce turbulence, and thereby run the analyses at higher  $Re$ , which is considered easier to handle in the post-processing of the data obtained, as the flow is already chaotic. CFD, when using the right boundary conditions and parameters, can give a more ideal model, which can be perfectly smooth. It is thereby easier to do an analysis at lower Reynolds numbers, such as in this present study.

The Strouhal number is, as mentioned in chapter 5.5, found by using probes at specific locations along the cylinder length. These have been placed in the vortex shedding region, but the presence of the wall induce different flow features along the cylinders, meaning that the vortex shedding will be changing at different locations. Vortex suppression close to the wall might require a different probe placement than vortex shedding from the mid-span. Having probes located along a straight line might cause interference in the results and not give a correct picture of the Strouhal number variation along the span of the cylinders. Ideally, one should place probes at different spanwise locations  $z/D$  to ensure that the probe is located where vortex shedding takes place. This could be a suggestion for further investigation of this problem.

Several articles argue that three-dimensional effects are important to consider to get the full flow picture. This is also found for tandem cylinders, where the three-dimensional effects are highly present for a Reynolds number above 190. For flow around a wall-mounted cylinder, [Sahin et al. \(2007\)](#) found three stagnation points in the flow, indicating the development of three different horseshoe vortices. This shows how important it is to measure the three-dimensional flow around the cylinder, as more than one vortex can occur around the junction. In this simulation, only one single primary vortex occurred in front of the upstream cylinder, due to the low Reynolds number. However, the flow picture changes over the cylinder length, and the downstream cylinder experiences a similar vortex to a horseshoe that needs proper 3D visualization. [Marakkos and Turner \(2006\)](#) argues the use of coloured representation, which highlights the influence of the pressure gradients on the flow, and thereby shows obvious advantages compared to a grey-scale representation. This has been important during the entire work, as a coloured representation of results makes it easier to distinguish between different levels of interesting attributes, e.g. pressure, velocity and vorticity.

## 6.1 Further investigations

Having two circular cylinders in tandem arrangement fixed to a flat wall, makes the flow even more complex than for the same configuration in free flow or having only a single cylinder mounted to a flat plate. The tandem arrangement is the basis of numerous investigations, making it possible to alter a wide range of parameters, such as including a wall at one end. The simplest configuration is chosen here, with a fixed diameter for both cylinders, mounted to a smooth and flat vertical wall. This has been a very good starting point for understanding the flow at low Reynolds numbers, but in reality this is not always the case. Below, some main points are listed as ideas for further investigation.

- **Increase the Reynolds number to get turbulent flow.** This thesis only focused on low

Reynolds numbers, and by increasing it, a more realistic picture of the flow in Bjørnafjorden would be provided. Increasing the Reynolds number in a numerical simulation also include choosing a turbulence model. One possibility is to test different turbulence models and see how they affect the results.

- **Change the spacing between the two cylinders.** A different kind of spacing can be used, based on the criteria described in the technical report for Bjørnafjorden (Team, 2016). It would be interesting to see how the spacing between the two cylinders affect the wake flow and the vortex structure that appear here. The flow is already quite complex having an end wall, so changing the spacing to see if this have any effect on the vortical structure in the wake is very intriguing.
- **Change the arrangement from tandem to staggered.** For a real case, the configuration will not be entirely fixed and straight, there will be some curve along the bridge span to avoid i.e. vortex induced vibrations (VIV). One possibility for further investigations is to change the configuration such that the cylinders are staggered. This will be the same as having an angle on the incoming flow in the x-direction on the present configuration. It would be very interesting to see how the flow now acts, and if there are disturbances present due to the staggered configuration.
- **Two different cylinder diameters.** The two cylinders will have a different size, like it often is in reality. The SFTB consists of two different sections with unequal diameter, and the effect of this would be interesting to see together with the tandem arrangement mounted to a wall.
- **Wall roughness.** An end wall in a fjord crossing in Norway often consists of different kind of rocks and a roughness will naturally be present. Investigating how roughness on the wall will affect the incoming flow on the two cylinders, will be very intriguing, instead of having a perfectly smooth surface.
- **Wall inclination.** In reality, the end wall in the fjord crossing will not be entirely flat due to the different rocks and the roughness. By including a wall inclination in the simulation, the uneven surface of the end wall can be investigated. It would be very interesting to see how an inclination on the wall have an effect on the incoming flow to the cylinders.
- **Logarithmic velocity profile at the inlet of the domain.** Having a logarithmic velocity profile at the inlet boundary instead of a uniform inlet velocity, will help decrease the inlet length of the domain and the overall size of the computational domain. It will also speed up the development of the boundary layer and makes it possible to refine the mesh grid even further close to the end wall and the cylinders.
- **Change front boundary condition.** The boundary condition along the front of the domain could be changed from a free-slip condition to i.e. a cyclic condition or some condition that better model the infinitely long cylinder. This may make it possible to induce an infinitely long cylinder and reduce the z-direction of the domain, and maintain or even increase the quality of the solution along the cylinders.
- **Convergence study.** Investigate the effect of the grid size and the time step of the solution. It would be interesting to find out how small the time step must be for the results to fully converge, and how small the domain can be to get good results.
- **Separation of flow.** Investigate how the separation of flow act along the span of the cylinders. How does the wall bounded streamlines distribute over the two cylinders? This would be a good indication of the chaos in the flow upon the downstream cylinder, and can be a good way of seeing how the horseshoe vortices forms along the cylinder surface.

# Chapter 7

## Conclusion

Numerical simulations of viscous flow around two circular tandem cylinder ending on a flat plate with a Reynolds number of 500 have been performed. The center-to-center spacing between the cylinders was set to  $S/D = 4$ , indicating a co-shedding regime. The investigation in this thesis mainly focused on the flow picture near the wall and how the pressure and forces act compared to further out. By reviewing the results of this work, the following conclusions can be drawn.

- Previous research regarding flow around two tandem cylinders mounted to a flat plate is not extensive, and the studies that concerns this topic, have not been performed with the same flow parameters or geometry as in the present study. A comparison with similar and simplified studies have therefore been performed, regarding tandem cylinders in free flow and one single cylinder mounted to a flat plate.
- The viscous flow around two circular tandem cylinder ending on a flat plate is found to be quite complex at low Reynolds numbers. A horseshoe vortex is found in front of the upstream cylinder, while a horseshoe-like vortex is found in front of the downstream one. Behind each cylinder, a similar upflow is found, but the flow around the downstream cylinder is much more chaotic and disturbed compared to the upstream one. The flow pattern was visualized through vorticity iso-surfaces and streamlines.
- The velocity distribution in the wake of each cylinder have been investigated, and reveals that the downstream cylinder experience a higher magnitude of both the u- and v-component of the velocity. The curves are similar to the single mounted cylinder-case, but the wake of the upstream cylinder is highly influenced by the second cylinder, especially regarding the u-component of the velocity.
- The pressure distribution of the upstream cylinder resemble the one of a single cylinder ending on a flat plate. The distribution show differences along the span of the cylinders, where  $C_p$  seems to be lower and have a more flattened curve near the upstream junction compared to further out on the cylinder. This is explained by the friction from the wall who contribute to flow separation and the horseshoe vortex system. The downstream cylinder, however, have higher pressure near the wall compared to at  $z/D \approx 16$ , but it may seem that around the mid-span of the cylinder, the flow regime changes from co-shedding to reattachment for a small region, based on streamlines and pressure.
- An FFT-analysis was run for the v-component of the velocity to find the Strouhal number in the wake of each cylinder. These were found to vary along the span of the cylinder, indicating vortex suppression near the wall and synchronized vortex shedding at the other end.
- In the post-processing of the data, it was found that the both the lift and drag coefficients for the downstream cylinder were much higher compared to the upstream one. This is explained



by the synchronized vortex shedding and the impingement of vortices shed from the upstream cylinder upon the downstream one.

The author believes that the study presented in this thesis helps to improve the understanding of flows with wake interference from having two cylinders and a wall present in the simulation. This can be very useful for future investigations of other aspects of such flows. Some suggestions for further investigations are mentioned in chapter [6.1](#).



# Nomenclature

## Abbreviations

2D	Two-dimensional
3D	Three-dimensional
ADV	Acoustic Doppler Velocimetry
AR	Aspect ratio
CFD	Computational Fluid Dynamics
CFL	Courant-Friedrich-Lewy condition
CV	Control Volume
DNS	Direct Numerical Simulation
FFT	Fast Fourier Transform
HPV	Hairpin vortex
HSV	Horseshoe Vortex
LIC	Line Integral Convolution
NPRA	Norwegian Public Road Administration
PIV	Particle Image Velocimetry
RMS	Root Mean Square
SFTB	Submerged Floating Tube Bridge
TLP	Tension Leg Platform
VIV	Vortex Induced Vibrations
VS	Vortex Structure

## Symbols

$\delta$	Boundary layer thickness
$\mu$	Dynamic viscosity
$\nu$	Kinematic viscosity
$\overline{C}_D$	Mean drag coefficient
$\overline{C}_L$	Mean lift coefficient
$\rho$	Density of fluid
$\vec{\omega}$	Vorticity

$C_D$	Drag coefficient
$C_L$	Lift coefficient
$D$	Diameter
$f_v$	Vortex shedding frequency
$F_x, F_y$	Force in x-(drag) and y-direction (lift)
$Fn$	Froude number
$p$	Pressure
$Re$	Reynolds number
$S/D$	Longitudinal spacing ratio
$St$	Strouhal number
$T_v$	Vortex shedding period
$U$	Inflow velocity of the free flow

# List of Figures

1.1	SFTB with pontoons. Illustration from Snøhetta/Statens Vegvesen . . . . .	2
1.2	SFTB anchored by tethers. Illustration by Snøhetta/Statens Vegvesen . . . . .	2
1.3	Principal sketch of tandem cylinders fixed to a vertical wall . . . . .	2
2.1	Principle sketch of separation of flow around a cylinder. . . . .	6
2.2	Pressure over the cylinder surface for potential and real flow. The real flow has $Re = 100$ . Blue line: real flow. Red line: potential flow. . . . .	6
2.3	Velocity profiles over the cylinder surface, at 3 locations for $Re = 100$ . $\theta$ given in degrees. . . . .	7
2.4	Vortex Shedding phenomenon, collected from Sumer and Fredsøe (2006) . . . . .	8
2.5	Time history of lift and drag coefficients for $Re = 300$ . Pink line: $C_D$ . Blue line: $C_L$ . . . . .	9
2.6	Vortex shedding from a cylinder (Sumer and Fredsøe, 2006) . . . . .	9
2.7	Iso-surfaces of z-vorticity ( $\omega_z$ ) at $Re = 300$ . . . . .	10
2.8	Interference of flow regions based on Zdravkovich (2003), where $L^*$ , $T^*$ denotes the streamwise (L/D) and transverse (T/D) separations between the cylinders. Modified and collected from Zhou and Mahbub Alam (2016) . . . . .	11
2.9	Classification of flow patterns, collected from Igarashi (1981). . . . .	12
2.10	Sketches of flow patterns. First published by Igarashi (1981), here collected from Sumner (2010). . . . .	13
2.11	Distribution of pressure from Igarashi (1981) . . . . .	14
2.12	Definition of flow around a circular cylinder placed on a bed in steady current. Collected from Roulund et al. (2005). . . . .	16
2.13	Vortex structures visualized by instantaneous iso-surfaces of the $\lambda_2$ -criterion for $Re = 500$ . . . . .	17
2.14	2D vorticity contours of $\omega_z$ for $Re = 500$ . . . . .	18
2.15	Mean pressure coefficient at three different spanwise locations, $z/D = 0.0515, 8$ and $\approx 16$ , for a cylinder of length $16D$ with $Re = 500$ . . . . .	19
2.16	Mean pressure contours at spanwise location, $z/D = 15.868$ , for a cylinder of length $16D$ with $Re = 500$ . . . . .	20
2.17	Mean pressure coefficient at spanwise location, $z/D = 0.0515$ , for a cylinder of length $16D$ with $Re = 500$ . . . . .	21
2.18	FFT-spectrum for different spanwise locations for a case with $Re = 500$ . . . . .	22
2.19	Time history of drag and lift coefficient for a single wall-mounted cylinder, at $Re = 500$ . . . . .	23
2.20	Vortex structures visualized by iso-surfaces of the $\lambda_2$ -criterion, for $Re = 500$ . . . . .	24
4.1	2D illustration of the mesh in the x-y-plane . . . . .	28
4.2	Computational domain definition sketch for tandem cylinders fixed to a wall. Uniform inflow velocity profile. For the present study, $D=1, S=4D$ . . . . .	29
4.3	Velocity profiles at three different locations along the cylinder surface . . . . .	31
4.4	Velocity profiles along the wall of $U_x$ , in front of the upstream cylinder . . . . .	32
5.1	The resolution of the mesh grid in the x-z-plane . . . . .	37

5.2	Instantaneous $\lambda_2 = 1$ iso-surfaces, viewed from above . . . . .	38
5.3	Instantaneous iso-surfaces for $\lambda_2 = 2$ in upstream of each cylinder . . . . .	38
5.4	Instantaneous vorticity distribution along the span of the cylinders, at the same time instant, visualized by the Q-criterion . . . . .	39
5.5	Streamlines of mean $u$ , by SurfaceLIC in x-y-plane for $z/D = 0.0515$ . . . . .	40
5.6	Streamlines of mean $v$ by SurfaceLIC in x-y-plane for $z/D = 0.0515$ . . . . .	41
5.7	Streamlines of mean $w$ by SurfaceLIC in x-y-plane for $z/D = 0.0515$ . . . . .	41
5.8	Streamlines of mean $u$ by SurfaceLIC in x-y-plane for $z/D = 15.868$ . . . . .	42
5.9	Streamlines of mean $v$ by SurfaceLIC in x-y-plane for $z/D = 15.868$ . . . . .	42
5.10	Streamlines of mean $w$ by SurfaceLIC in x-y-plane for $z/D = 15.868$ . . . . .	43
5.11	Streamlines by mean $u$ in the x-z-plane, zoomed in on the junction . . . . .	43
5.12	Streamlines by mean $v$ in the x-z-plane, zoomed in on the junction . . . . .	44
5.13	Streamlines by $w$ in the x-z-plane, zoomed in on the junction . . . . .	44
5.14	Magnification of the flow feature upstream of each cylinder, coloured by mean u-component of $U$ . . . . .	45
5.15	Normalized velocity profiles of mean $u$ at $z/D \approx 16$ . . . . .	46
5.16	Normalized velocity profiles of mean $u$ at $z/D = 0.0515$ . . . . .	47
5.17	Normalized velocity profiles of mean $u$ in the wake behind the cylinders for $z/D \approx 16$ . . . . .	47
5.18	Normalized velocity profiles of mean $u$ in the wake behind the cylinders for $z/D = 0.0515$ . . . . .	48
5.19	Illustration of the location of the sampling lines for the mean velocity in x-y-plane, $0.6D$ from the cylinder center . . . . .	49
5.20	Pressure distribution over the two circular tandem cylinders . . . . .	50
5.21	Pressure contours at $z/D \approx 16$ . . . . .	51
5.22	Pressure contours at $z/D = 0.0515$ . . . . .	52
5.23	Vorticity contours at two spanwise locations . . . . .	53
5.24	Time history of lift coefficient, $C_L$ . Blue line: Upstream. Red line: Downstream. . . . .	54
5.25	Time history of drag coefficient, $C_D$ . Blue line: Upstream. Red line: Downstream. . . . .	55
5.26	Locations of the two probes in the computational domain in the x-y-plane, here visualized with velocity $U$ magnitude . . . . .	57
5.27	Energy spectra for various spanwise locations along the cylinder . . . . .	58
A.1	Pressure contours for $z/D = 8$ . . . . .	II
A.2	2D vorticity contours of $\omega_z$ at $z/D = 8$ , where $x = -0.5$ to $12.5$ and $y = -3.3$ to $2.8$ . . . . .	III
A.3	Streamlines for velocity $U$ magnitude, showing the influence of cylinder length $8D$ . . . . .	IV
A.4	Streamlines for mean $u$ , showing influence of cylinder length $12D$ . . . . .	IV
A.5	Streamlines for mean $u$ , showing influence of cylinder length $16D$ . . . . .	IV
A.6	Strouhal number for different spanwise locations, $z/D = 0.5, 4, 8$ and $16$ . . . . .	V
A.7	Iso-surface of $\lambda_2$ and $Q$ from simulations with $Re = 500$ . . . . .	VI
A.8	Pressure contours for $z/D = 8$ . . . . .	VII
A.9	Normalized velocity profiles of mean $v$ in the wake behind the cylinders for $z/D = 0.0515$ . . . . .	VIII
A.10	Normalized velocity profiles of $v$ in the wake behind the cylinders for $z/D \approx 16$ . . . . .	IX
A.11	Illustration of the location of the sampling lines for the mean $v$ -velocity in x-y-plane . . . . .	X
A.12	Velocity contours in x-z-plane, zoomed in near the wall, coloured by mean $u$ -velocity. . . . .	XI
A.13	Streamlines of mean $u$ by SurfaceLIC in x-y-plane for $z/D = 8$ . . . . .	XI
A.14	Streamlines of mean $v$ by SurfaceLIC in x-y-plane for $z/D = 8$ . . . . .	XII
A.15	Streamlines of mean $w$ by SurfaceLIC in x-y-plane for $z/D = 8$ . . . . .	XII
A.16	Velocity vectors in the x-z-plane, zoomed in near the wall . . . . .	XIII

# List of Tables

2.1	Strouhal number for different single cylinder studies . . . . .	22
4.1	Overview of different boundary conditions applied in the domain . . . . .	30
5.1	Details of simulation . . . . .	36
5.2	Mean and RMS of drag and lift for different studies . . . . .	56
5.3	Strouhal number for both cylinders at a selection of spanwise locations . . . . .	59

# Bibliography

- J. R. Aarnes, H. I. Andersson, and N. E. L. Haugen. Numerical investigation of free-stream turbulence effects on the transition-in-wake state of flow past a circular cylinder. *Journal of Turbulence*, 19(3):252–273, Mar. 2018.
- B. Ataie-Ashtiani and A. Aslani-Kordkandi. Flow field around single and tandem piers. *Flow Turbulence And Combustion*, 90(3):471–490, April 2013. ISSN 1386-6184.
- U. Ayachit. The ParaView Guide Community Edition. Kitware Inc., Nov. 2016.
- D. Barkley and R. Henderson. Three-dimensional floquet stability analysis of the wake of a circular cylinder. *Journal Of Fluid Mechanics*, 322:215–241, September 1996. ISSN 0022-1120.
- H. Cao and D. Wan. Application of OpenFOAM to simulate three-dimensional flows past a single and two tandem circular cylinders. *Proceedings of the International Offshore and Polar Engineering Conference*, 3:702–709, June 2010.
- B. Carmo and J. Meneghini. Numerical investigation of the flow around two circular cylinders in tandem. *Journal of Fluids and Structures*, 22(6-7):979–988, August 2006. ISSN 0889-9746. URL <http://search.proquest.com/docview/29286834/>.
- J. M. Cimbala and Y. A. Cengel. *Fluid Mechanics Fundamentals and Applications*. McGraw-Hill Professional, 2013.
- B. Dargahi. The turbulent flow field around a circular cylinder. *Experiments in Fluids*, 8(1):1–12, October 1989. ISSN 0723-4864.
- C. Escauriaza and F. Sotiropoulos. Reynolds number effects on the coherent dynamics of the turbulent horseshoe vortex system. *Flow, Turbulence and Combustion*, 86(2):231–262, Mar 2011. ISSN 1573-1987. doi: 10.1007/s10494-010-9315-y. URL <https://doi.org/10.1007/s10494-010-9315-y>.
- O. M. Faltinsen. *Sea Loads on Ships and Offshore Structures*. Cambridge University Press, 1998.
- J. Fröhlich and W. Rodi. LES of the flow around a circular cylinder of finite height. *International Journal of Heat and Fluid Flow*, 25(3):537–548, 2004. ISSN 0142-727X.
- C. J. Greenshields. OpenFOAM Foundation: User Guide version 5.0, July 2017.
- R. F. Huang, C. M. Hsu, and W. C. Lin. Flow characteristics around juncture of a circular cylinder mounted normal to a flat plate. *Experimental Thermal and Fluid Science*, 55:187–199, May 2014. ISSN 0894-1777.
- Z. Huang, H. I. Andersson, and W. Cui. End-wall effects on vortex shedding in planar shear flow over a circular cylinder. *Computers and Fluids*, 42(1):102–107, 2011. ISSN 0045-7930.
- T. Igarashi. Characteristics of the flow around two circular cylinders arranged in tandem: 1st report. *Bulletin of JSME*, 24(188):323–331, 1981.



- J. Jeong and F. Hussain. On the identification of a vortex. *Journal of Fluid Mechanics*, 285:69–94, 1995.
- R. B. H. Kalvig. Numerical investigation of 3D flow around two tandem cylinders. Master’s thesis, Norwegian University of Science and Technology, 2015.
- T. Kitagawa and H. Ohta. Numerical investigation on flow around circular cylinders in tandem arrangement at a subcritical Reynolds number. *Journal of Fluids and Structures*, 24(5):680–699, July 2008. ISSN 0889-9746. URL <http://search.proquest.com/docview/33884908/>.
- N. Kondo and D. Matsukuma. Numerical simulation for flow around two circular cylinders in tandem. *International Journal of Computational Fluid Dynamics*, 19(4):277–288, May 2005. ISSN 1061-8562.
- K. Marakkos and J. T. Turner. Vortex generation in the cross-flow around a cylinder attached to an end-wall. *Optics and Laser Technology*, 38(4):277–285, 2006. ISSN 0030-3992.
- F. Moukalled, L. Mangani, and M. Darwish. *The Finite Volume Method in Computational Fluid Dynamics: An Advanced Introduction with OpenFOAM® and Matlab*. Springer International Publishing, Cham, 2016.
- R. Paciorri, A. Bonfiglioli, A. Di Mascio, and B. Favini. RANS simulations of a junction flow. *International Journal of Computational Fluid Dynamics*, 19(2):179–189, February 2005. ISSN 1061-8562.
- G. Palau-Salvador, T. Stoesser, and W. Rodi. LES of the flow around two cylinders in tandem. *Journal of Fluids and Structures*, 24(8):1304–1312, 2008. ISSN 0889-9746.
- G. V. Papaioannou, D. K. P. Yue, M. S. Triantafyllou, and G. E. Karniadakis. Three-dimensionality effects in flow around two tandem cylinders. *Journal of Fluid Mechanics*, 558:387–413, July 2006. ISSN 0022-1120.
- B. Pettersen. *Marin Teknikk 3 - Hydrodynamikk*. Akademika Forlag, 2014.
- M. A. Prsic. *Numerical simulations of the flow around single and tandem circular cylinders close to a plane wall*. PhD thesis, Norwegian University of Science and Technology, 2016. Chapters 2, 4 and 5.
- A. Roulund, B. M. Sumer, J. Fredsøe, and J. Michelsen. Numerical and experimental investigation of flow and scour around a circular pile. *Journal of Fluid Mechanics*, 534:351–401, July 2005. ISSN 0022-1120.
- B. Sahin and N. A. Ozturk. Behaviour of flow at the junction of cylinder and base plate in deep water. *Measurement*, 42(2):225 – 240, 2009. ISSN 0263-2241. doi: <https://doi.org/10.1016/j.measurement.2008.06.003>. URL <http://www.sciencedirect.com/science/article/pii/S0263224108001012>.
- B. Sahin, N. A. Ozturk, and H. Akilli. Horseshoe vortex system in the vicinity of the vertical cylinder mounted on a flat plate. *Flow Measurement and Instrumentation*, 18(2):57–68, 2007. ISSN 0955-5986.
- K. Satpathy, K. Velusamy, B. S. V. Patnaik, and P. Chellapandi. Numerical investigation of vortex shedding past a finite circular cylinder mounted on a flat plate. *Numerical Heat Transfer, Part A: Applications*, 59(11):882–909, June 2011. ISSN 1040-7782.
- R. L. Simpson. Junction flows. *Annual Review of Fluid Mechanics*, 33(1):415–433, 2001.
- B. M. Sumer and J. Fredsøe. *Hydrodynamics Around Cylindrical Structures : (Revised Edition)*, volume 26. WORLD SCIENTIFIC, September 2006. ISBN 9789812700391.

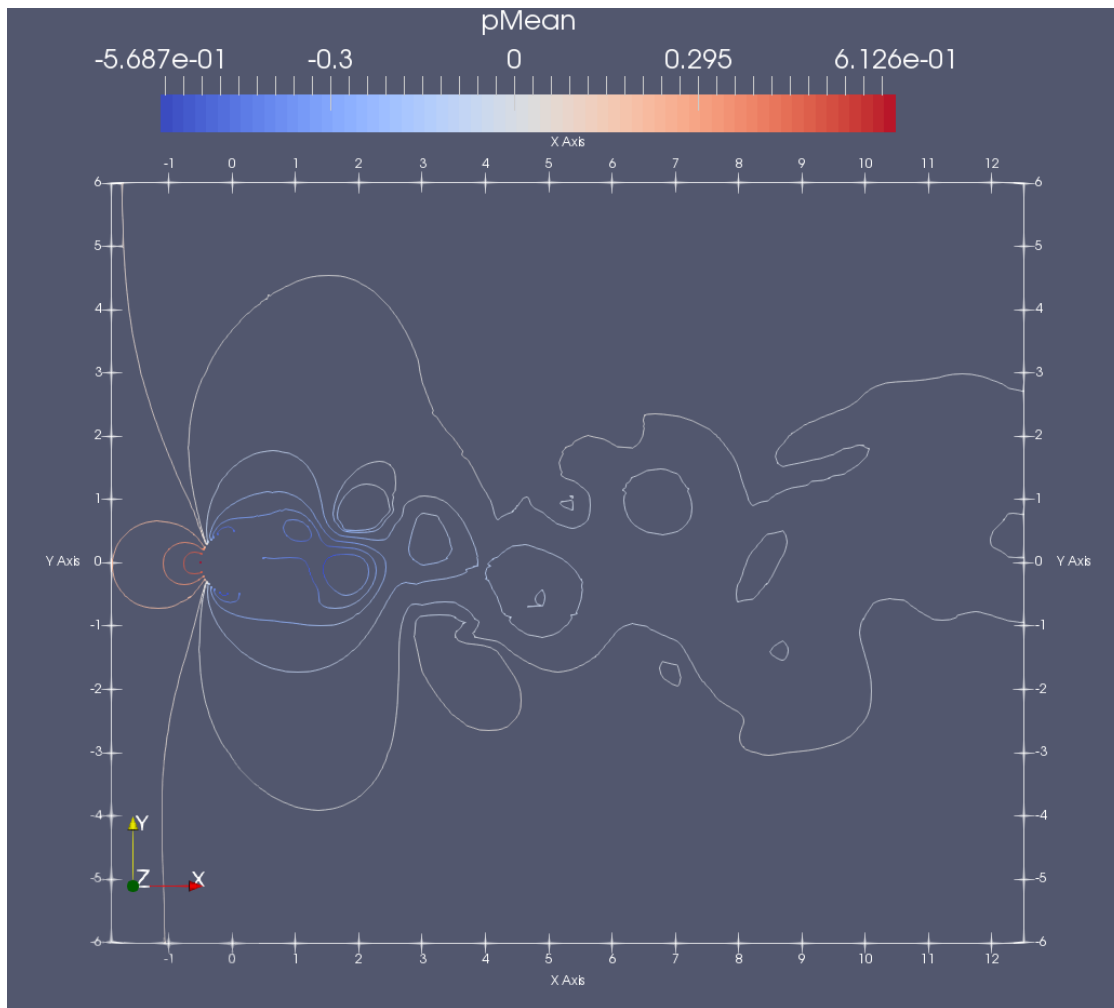
- D. Sumner. Two circular cylinders in cross-flow: A review. *Journal of Fluids and Structures*, 26 (6):849–899, 2010. ISSN 0889-9746.
- P. Team. Bjørnafjord Submerged Floating Tube Bridge - K3/K4 Technical Report. Technical report, Statens Vegvesen, 2016.
- A. Vakil and S. I. Green. Numerical study of two-dimensional circular cylinders in tandem at moderate Reynolds numbers. *Journal of Fluids Engineering, Transactions of the ASME*, 135 (7), 2013. ISSN 00982202.
- M. R. Visbal. Structure of laminar junction flows. *AIAA Journal*, 29(8):1273–1282, Aug. 1991.
- H. Vu, J. Ahn, and J. Hwang. Numerical simulation of flow past two circular cylinders in tandem and side-by-side arrangement at low Reynolds numbers. *KSCE Journal of Civil Engineering*, 20 (4):1594–1604, May 2016. URL <http://search.proquest.com/docview/1781526527/>.
- F. M. White. *Viscous fluid flow*. McGraw-hill Education - Europe, 2005.
- C. Williamson. Vortex dynamics in the cylinder wake. *Annual Review of Fluid Mechanics*, 28: 477–539, 1996. ISSN 00664189.
- M. Zdravkovich. Different modes of vortex shedding: An overview. *Journal of Fluids and Structures*, 10(5):427 – 437, 1996. ISSN 0889-9746. doi: <https://doi.org/10.1006/jfls.1996.0029>. URL <http://www.sciencedirect.com/science/article/pii/S0889974696900298>.
- M. Zdravkovich. *Flow around circular cylinders : a comprehensive guide through flow phenomena, experiments, applications, mathematical models, and computer simulations : Vol. 2 : [Applications]*, volume Vol. 2. Oxford University Press, Oxford, 2003. ISBN 9780198565611.
- H. Zhang and W. Melbourne. Interference between two circular cylinders in tandem in turbulent flow. *Journal of Wind Engineering & Industrial Aerodynamics*, 41(1-3):589–600, October 1992. ISSN 0167-6105.
- Y. Zhou and M. Mahbub Alam. Wake of two interacting circular cylinders: A review. *International Journal of Heat and Fluid Flow*, 62:510–537, December 2016. ISSN 0142-727X.

# Appendix A

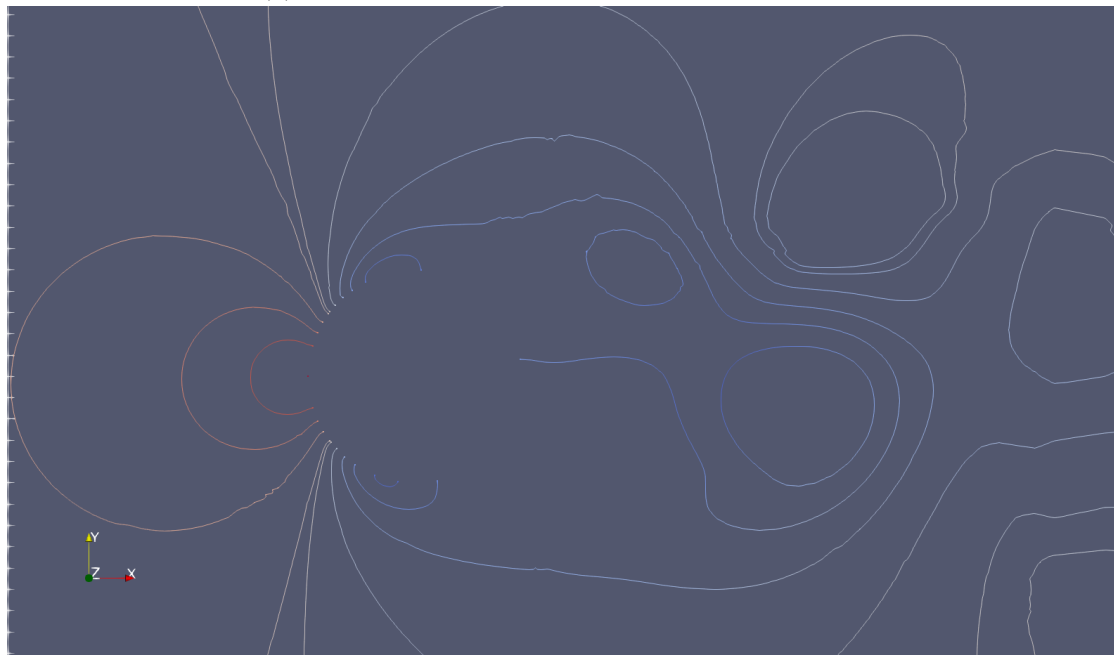
## Visualization

### A.1 Single cylinder fixed to wall

Pressure contours



(a) Full size, where  $x = -2$  to  $12.5$  and  $y = -6$  to  $6$ .



(b) Zoomed in

Figure A.1: Pressure contours for  $z/D = 8$

# Vorticity contours

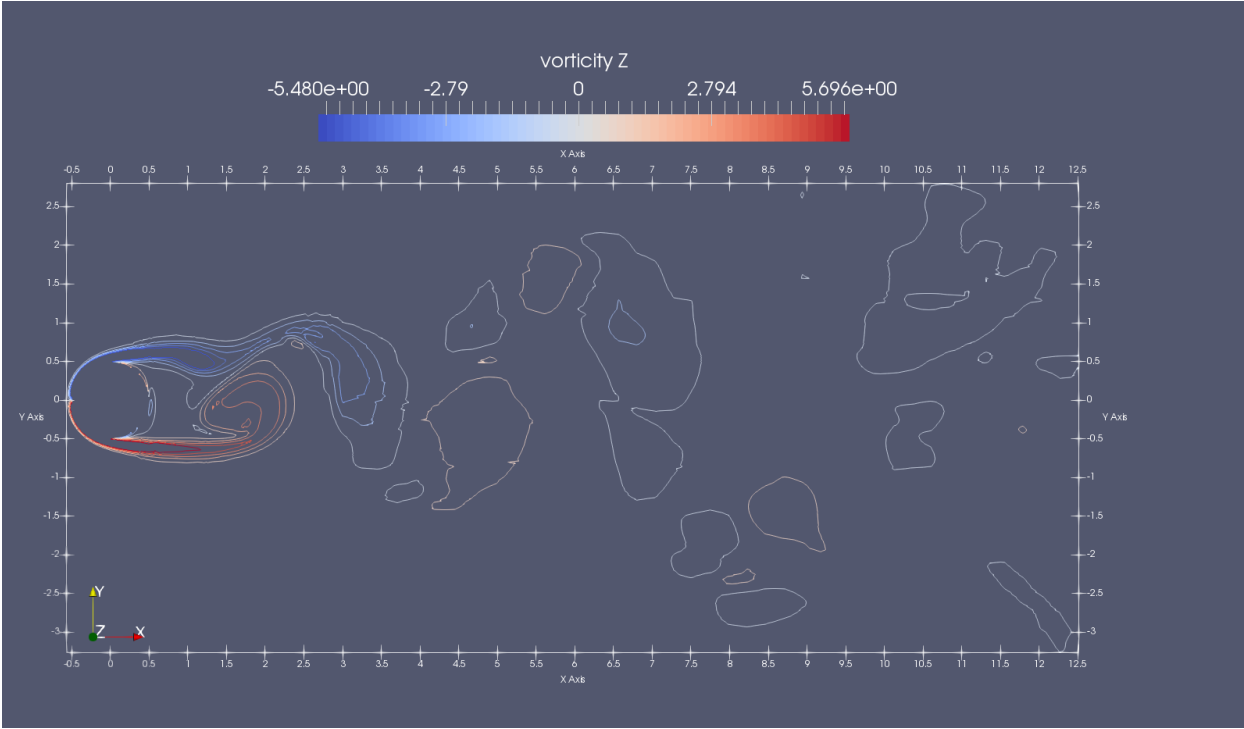


Figure A.2: 2D vorticity contours of  $\omega_z$  at  $z/D = 8$ , where  $x = -0.5$  to  $12.5$  and  $y = -3.3$  to  $2.8$ .

### Streamlines along cylinder length with UMean.

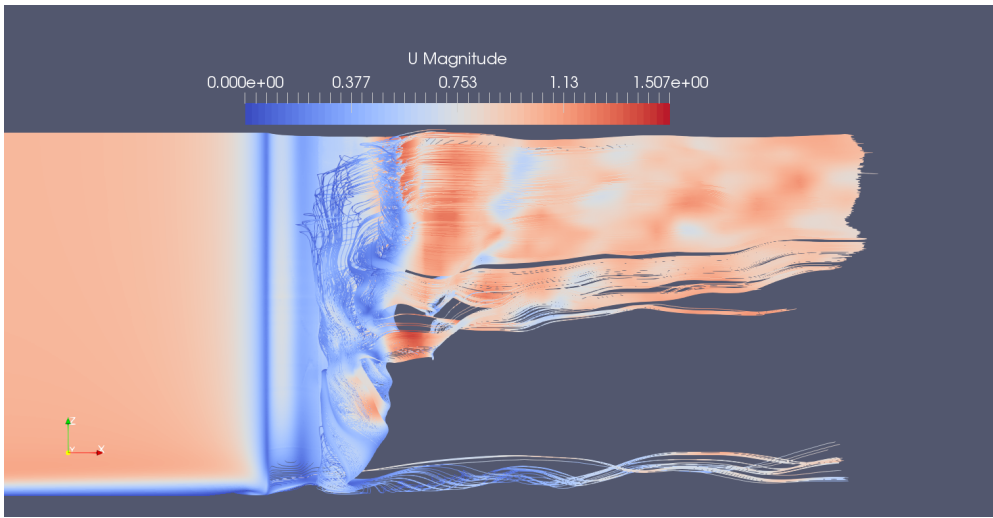


Figure A.3: Streamlines for velocity U magnitude, showing the influence of cylinder length 8D

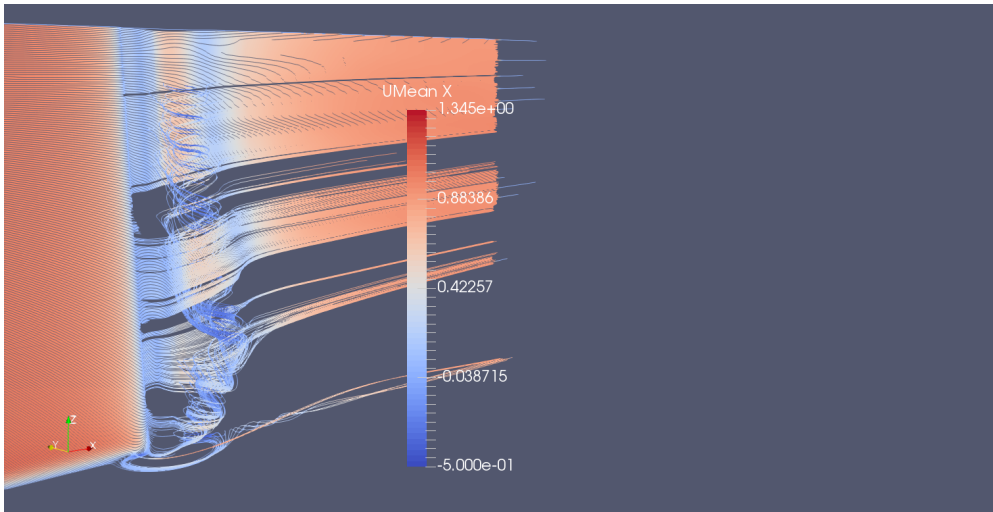


Figure A.4: Streamlines for mean u, showing influence of cylinder length 12D

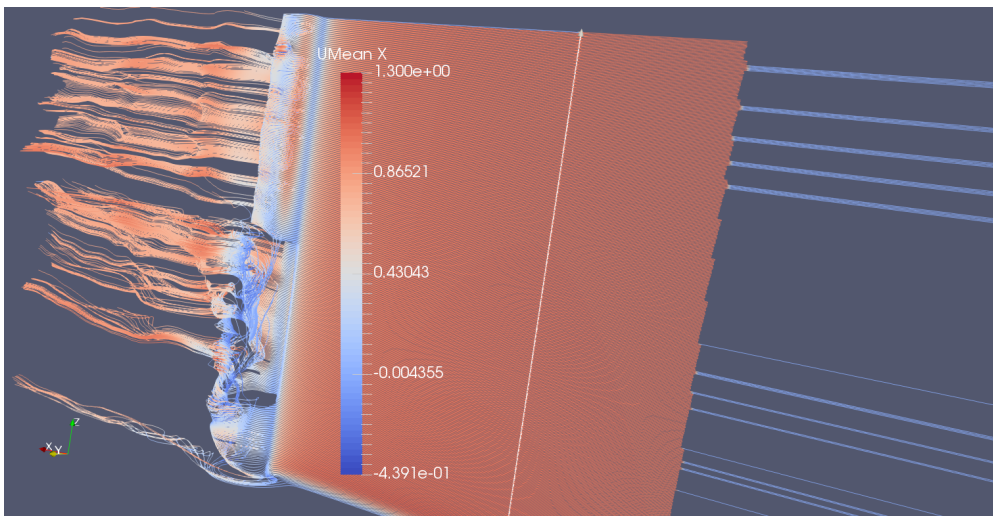


Figure A.5: Streamlines for mean u, showing influence of cylinder length 16D

# Strouhal number for single wall-mounted cylinder

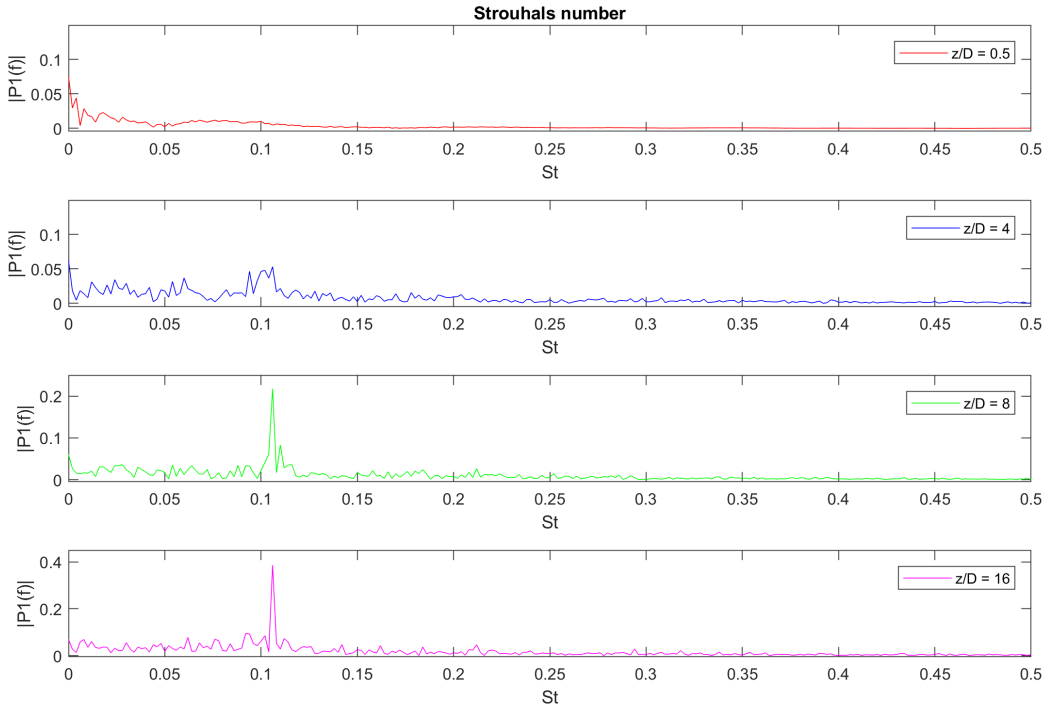
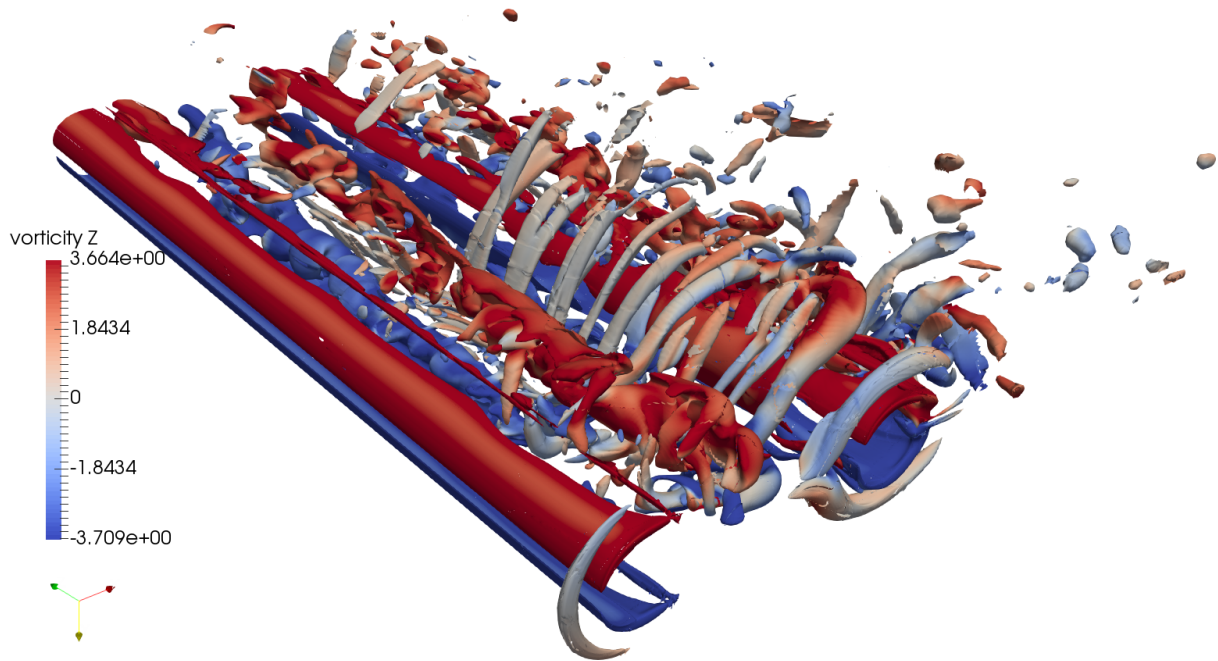


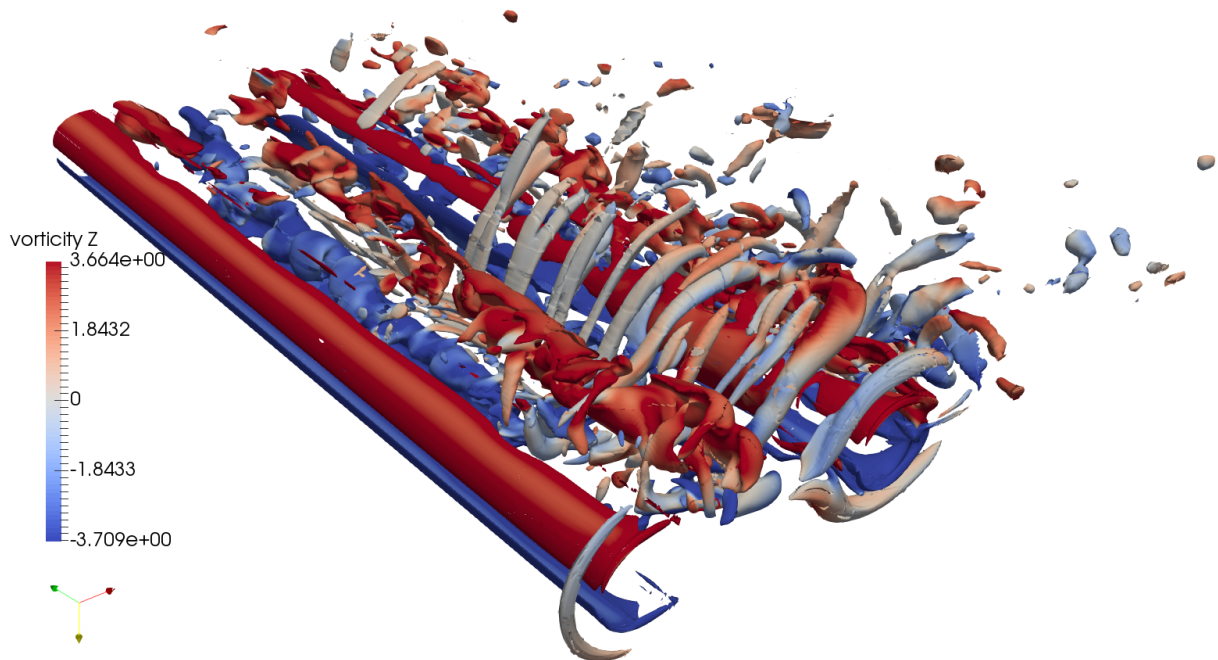
Figure A.6: Strouhal number for different spanwise locations,  $z/D = 0.5, 4, 8$  and  $16$ .

## A.2 Tandem cylinders fixed to wall

### Vorticity



(a) Instantaneous  $Q = 2$  iso-surface coloured by z-vorticity

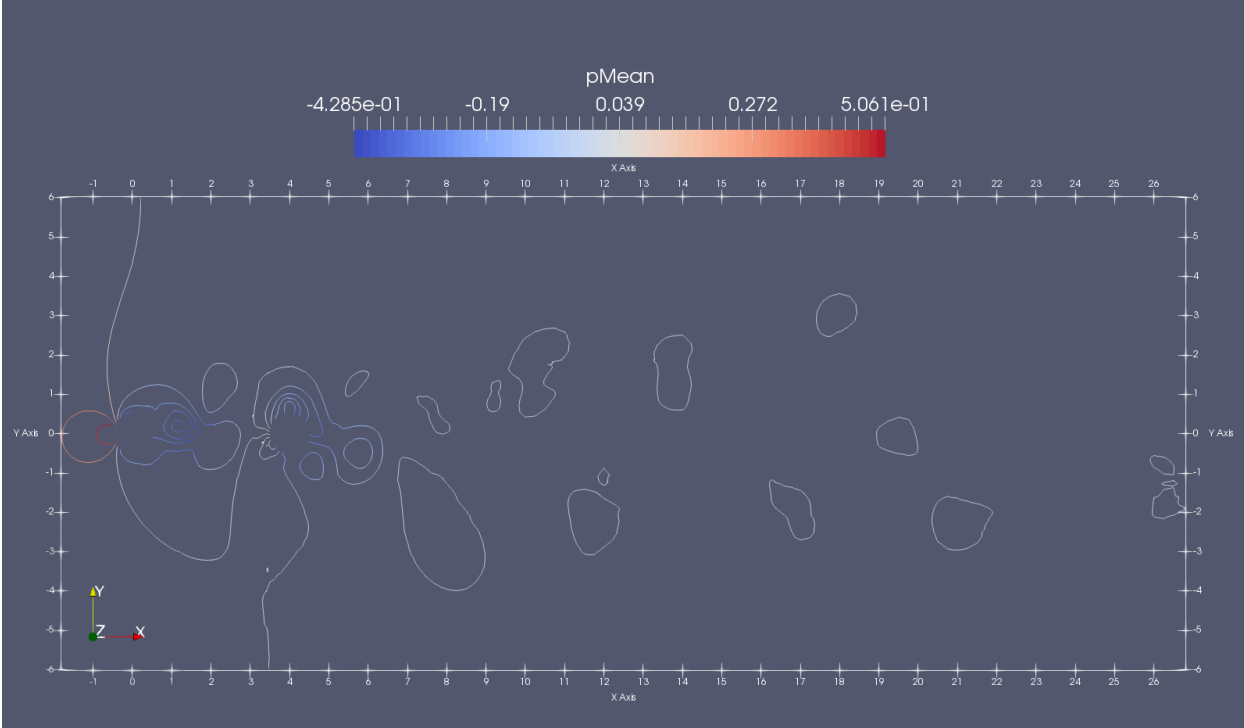


(b) Instantaneous  $\lambda_2 = 2$  coloured by z-vorticity

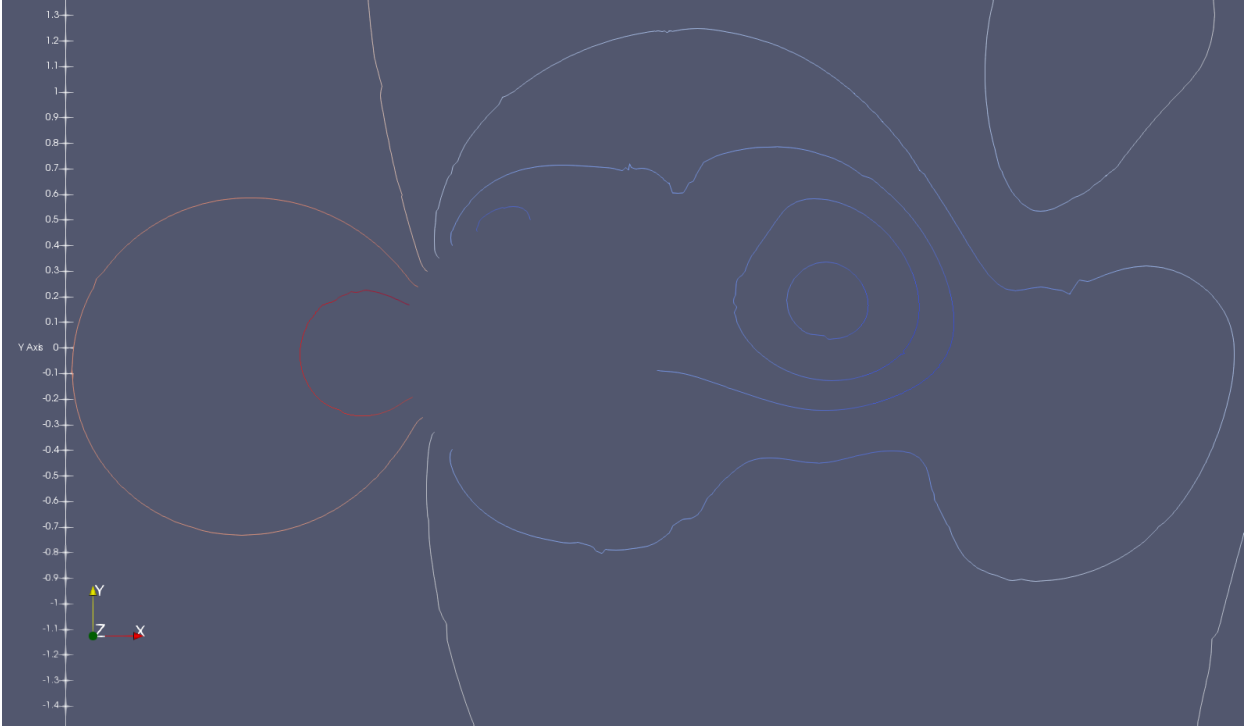
Figure A.7: Iso-surface of  $\lambda_2$  and  $Q$  from simulations with  $Re = 500$



Pressure contours



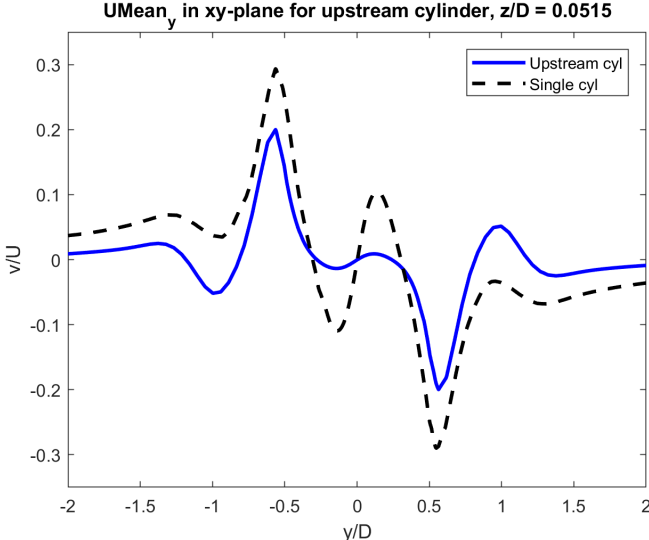
(a) Full size, where  $x = -2$  to  $27$  and  $y = 0$  to  $2$ .



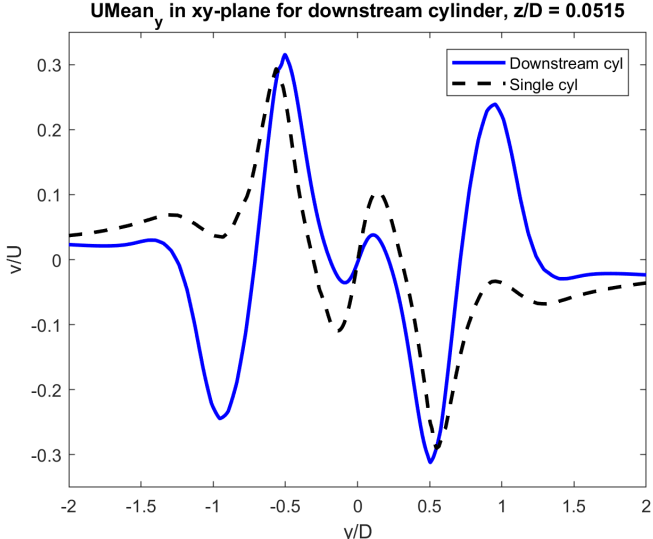
(b) Zoomed in

Figure A.8: Pressure contours for  $z/D = 8$

Normalized  $v/U$  velocity in the wake of each cylinder

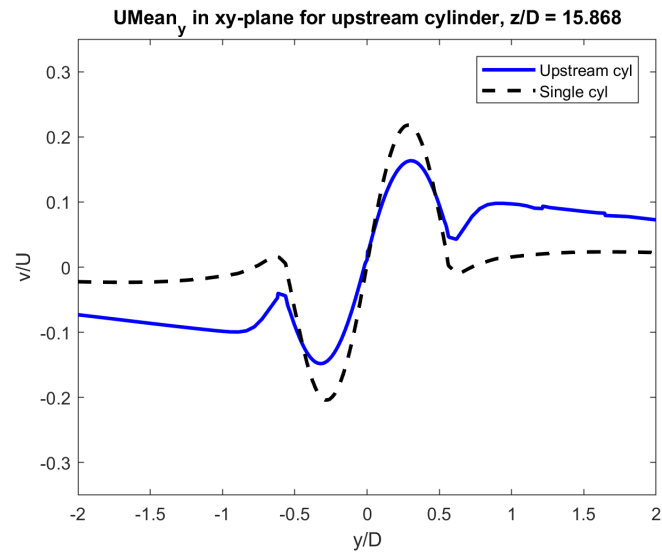


(a) Upstream

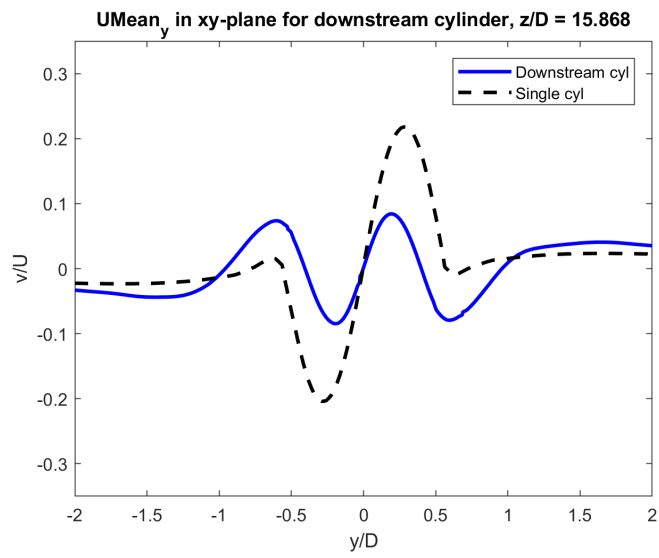


(b) Downstream

Figure A.9: Normalized velocity profiles of mean  $v$  in the wake behind the cylinders for  $z/D = 0.0515$

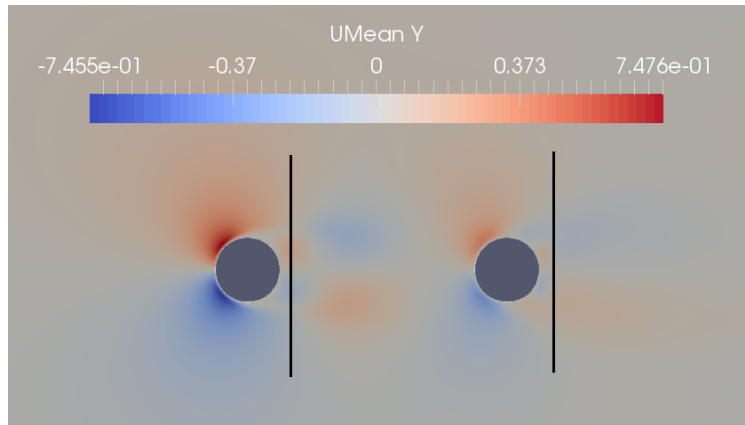


(a) Upstream

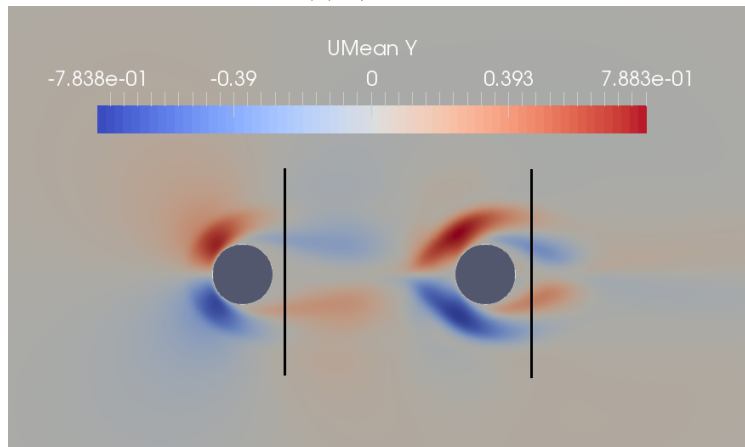


(b) Downstream

Figure A.10: Normalized velocity profiles of  $v$  in the wake behind the cylinders for  $z/D \approx 16$



(a)  $z/D \approx 16$



(b)  $z/D = 0.0515$

Figure A.11: Illustration of the location of the sampling lines for the mean v-velocity in x-y-plane

### Velocity plots

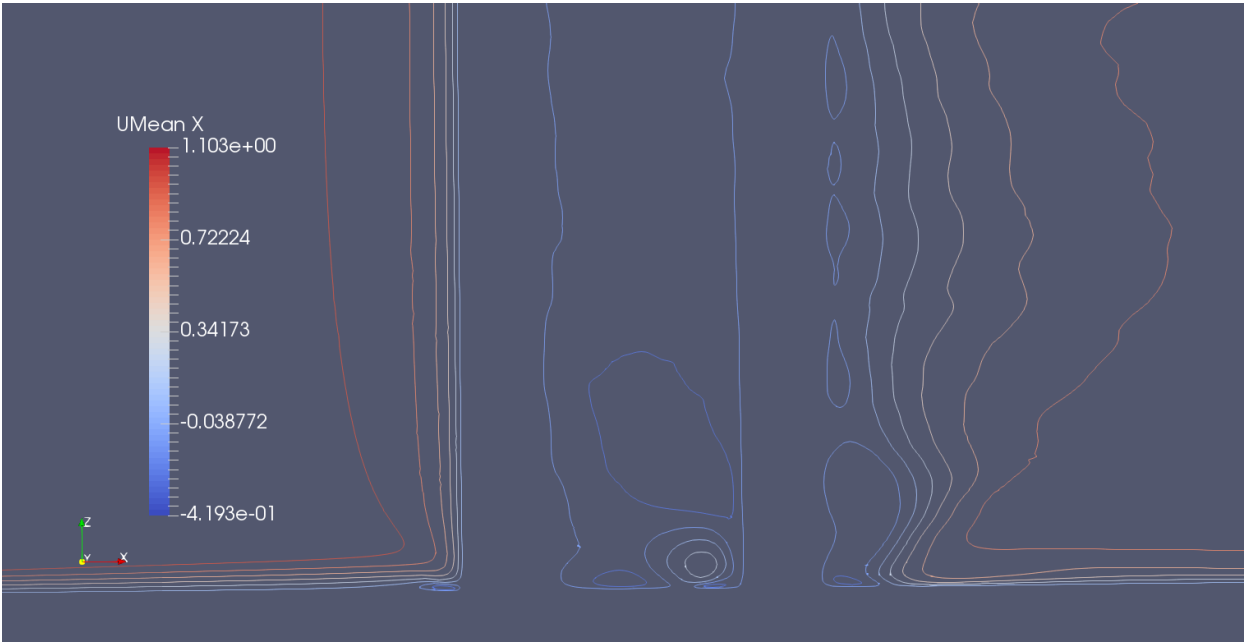


Figure A.12: Velocity contours in x-z-plane, zoomed in near the wall, coloured by mean u-velocity.

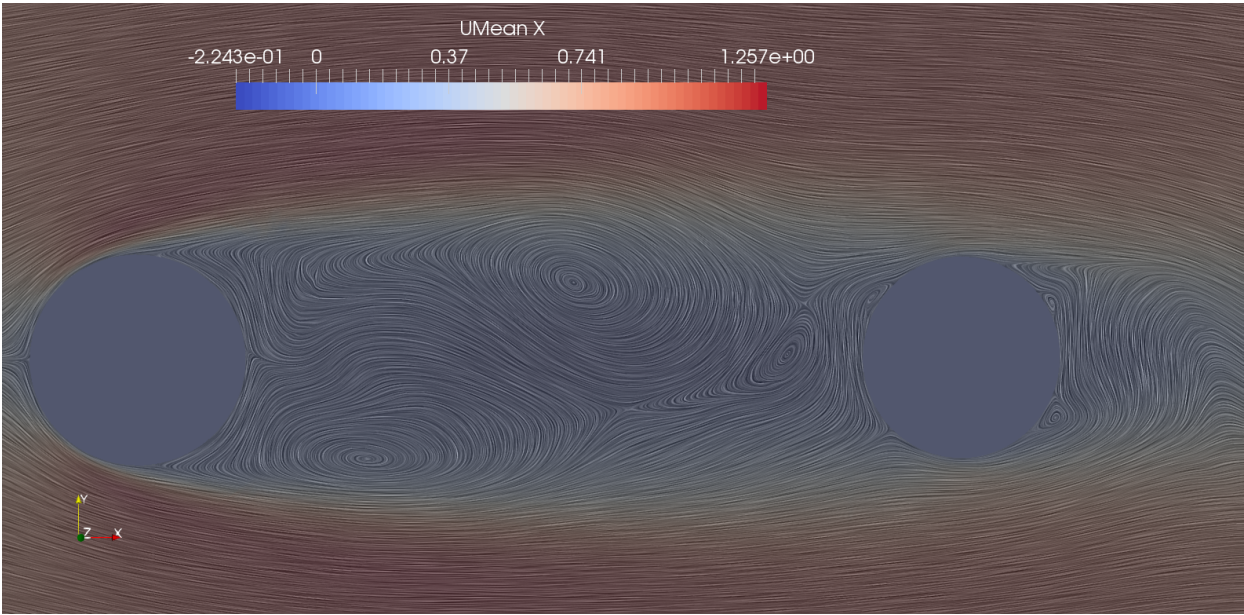


Figure A.13: Streamlines of mean  $u$  by SurfaceLIC in x-y-plane for  $z/D = 8$

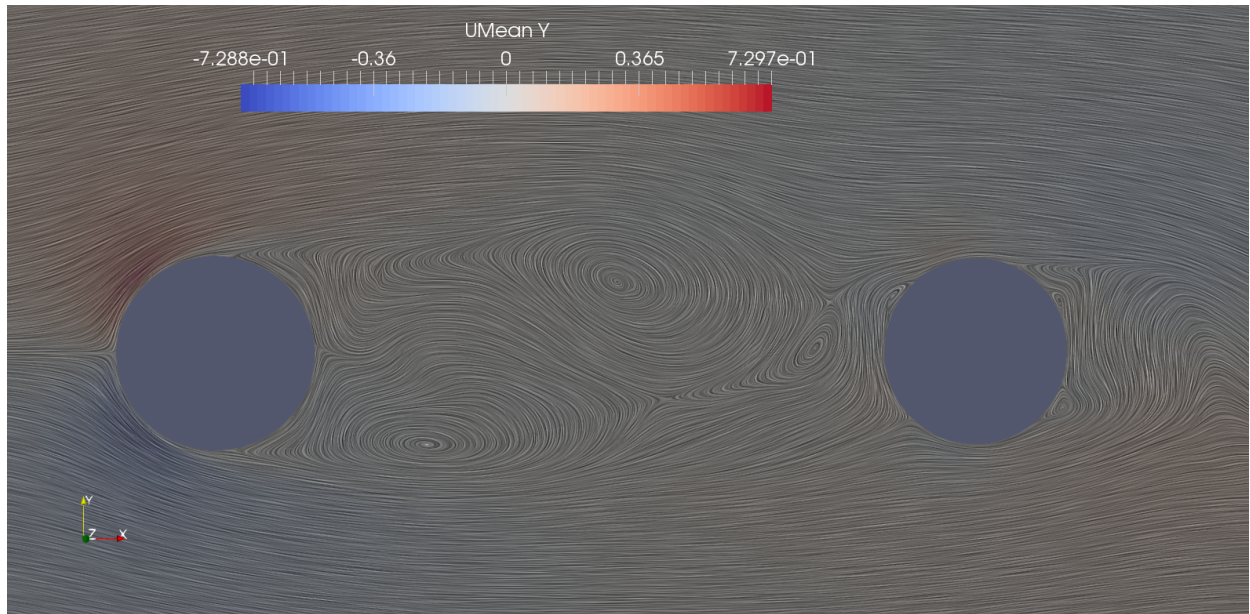


Figure A.14: Streamlines of mean  $v$  by SurfaceLIC in  $x$ - $y$ -plane for  $z/D = 8$

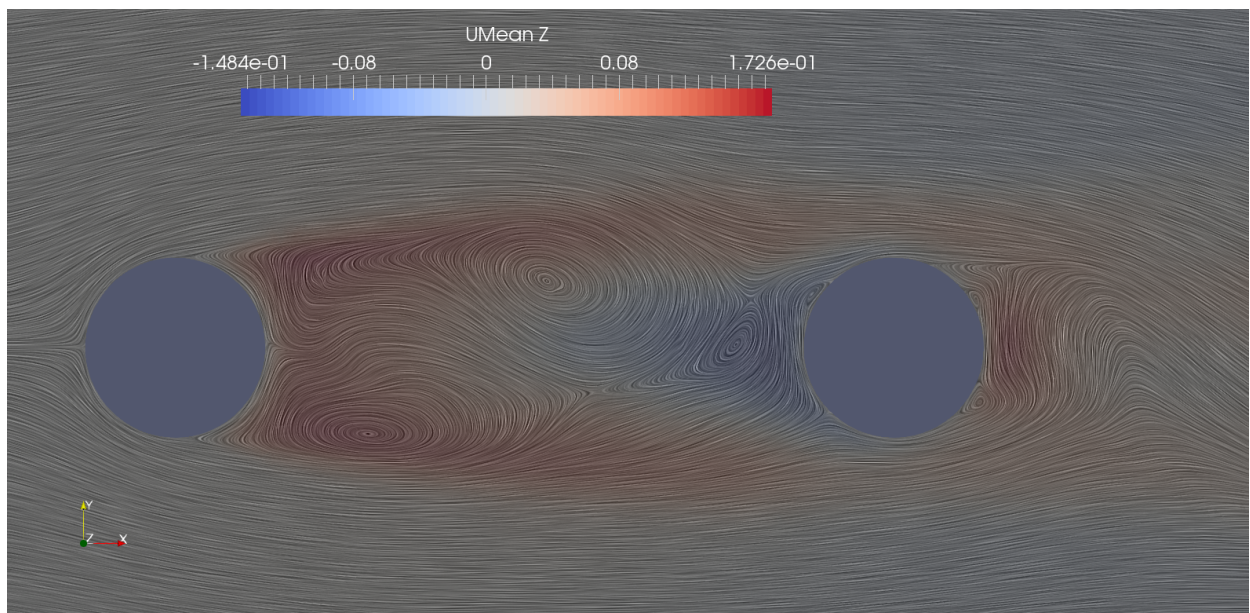


Figure A.15: Streamlines of mean  $w$  by SurfaceLIC in  $x$ - $y$ -plane for  $z/D = 8$

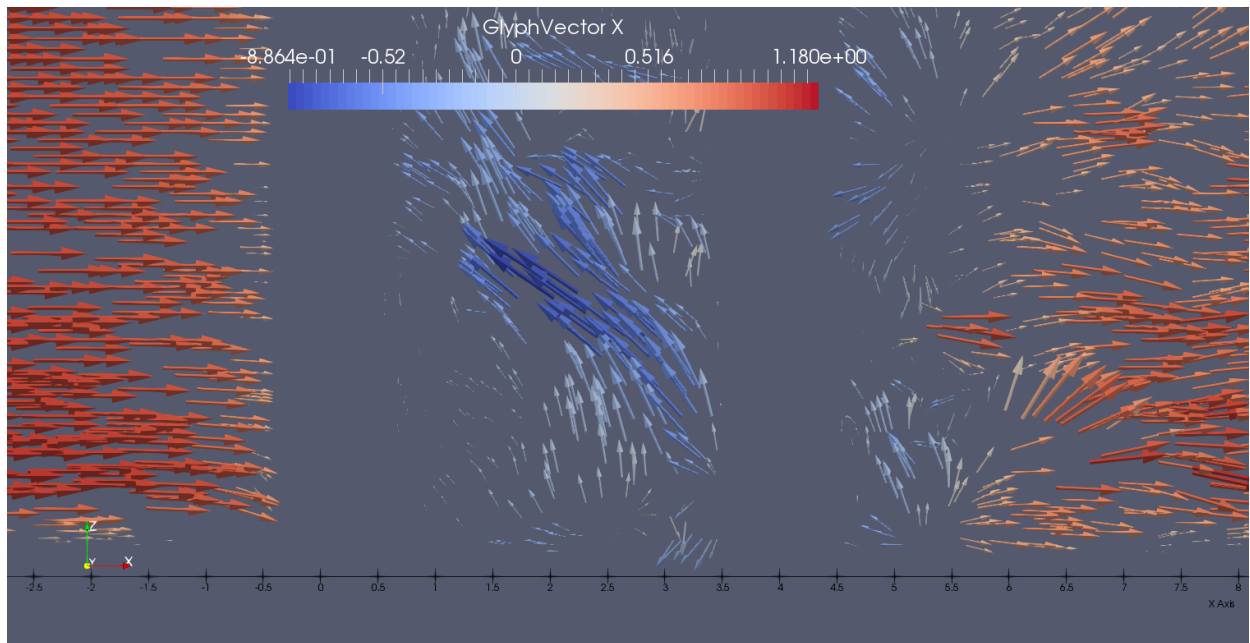


Figure A.16: Velocity vectors in the x-z-plane, zoomed in near the wall

# Appendix B

## OpenFOAM

### B.1 controlDict

```
/*-----* C++ *-----*\
/ ===== /
/ \\ / Field / OpenFOAM: The Open Source CFD Toolbox /
/ \\ / Operation / Version: 4.1 /
/ \\ / And / Web: www.OpenFOAM.org /
/ \\ / Manipulation /
\*-----*/
FoamFile
{
    version 2.0;
    format ascii;
    class dictionary;
    location "system";
    object controlDict;
}
// *****

application pisoFoam;

startFrom latestTime;

startTime 0;

stopAt endTime;

endTime 250.0;

deltaT 0.004;

writeControl timeStep;

writeInterval 10;

purgeWrite 2;
```



```

writeFormat      ascii;

writePrecision   6;

writeCompression off;

timeFormat       general;

timePrecision    6;

runTimeModifiable no;

functions
{

    fieldAverage1
    {
        // Type of functionObject
        type          fieldAverage;

        // Where to load it from (if not already in solver)
        functionObjectLibs ("libfieldFunctionObjects.so");

        // Function object enabled flag
        enabled        true;

        // When to output the average fields
        writeControl    writeTime;

        // Region option
        //region rotor;

        // Reset on output
        //resetOnOutput true;

        // Fields to be averaged - runTime modifiable
        fields
        (
            U
            {
                mean          on;
                prime2Mean    on;
                base           time;
            }

            p
            {
                mean          on;
                prime2Mean    on;
            }
        )
    }
}

```

```

        base      time;

    }

);
}

forceCoeffs1
{
    type          forceCoeffs;
    functionObjectLibs ( "libforces.so" );
    writeControl  timeStep;
    writeInterval 1;
    patches       ( cyl1 );
    pName         p;
    UName         U;
    rho           rhoInf;
    rhoInf        1000;
    magUInf       1.00;
    log           true;
    liftDir       (0 1 0);    //direction of lift
    dragDir       (1 0 0);    //direction of drag
    CofR          (0 0 0);
    pitchAxis     (0 0 0);
    lRef          16;         //reference length
    Aref          16;         //reference projection of impact area (D*1)
}

forceCoeffs2
{
    type          forceCoeffs;
    functionObjectLibs ( "libforces.so" );
    writeControl  timeStep;
    writeInterval 1;
    patches       ( cyl2 );
    pName         p;
    UName         U;
    rho           rhoInf;
    rhoInf        1000;
    magUInf       1.00;
    log           true;
    liftDir       (0 1 0);    //direction of lift
    dragDir       (1 0 0);    //direction of drag
    CofR          (4 0 0);    //center of radius??
    pitchAxis     (0 0 0);
    lRef          16;         //reference length
    Aref          16;         //reference projection of impact area (D*1)
}

#includeFunc probes

```

```

#includeFunc residuals
#includeFunc Q
#includeFunc vorticity
#includeFunc Lambda2

```

```

// ***** //

```

## B.2 fvSchemes

```

/*-----* C++ *-----*\
|=====|
| \\ / Field | OpenFOAM: The Open Source CFD Toolbox |
| \\ / Operation | Version: 4.1 |
| \\ / And | Web: www.OpenFOAM.org |
| \\ / Manipulation |
\*-----*/

```

```

FoamFile

```

```

{
    version      2.0;
    format       ascii;
    class        dictionary;
    location     "system";
    object       fvSchemes;
}

```

```

// ***** //

```

```

ddtSchemes

```

```

{
    default      CrankNicolson 0.9;
}

```

```

gradSchemes

```

```

{
    default      Gauss linear;
    grad(p)      Gauss linear;
}

```

```

divSchemes

```

```

{
    default      none;
    div(phi,U)   Gauss linear;
    div((nuEff*dev2(T(grad(U)))) Gauss linear;
}

```

```

laplacianSchemes

```

```

{
    default      Gauss linear corrected;
}

```

```

interpolationSchemes
{
    default          linear;
}

```

```

snGradSchemes
{
    default          corrected;
}

```

```

// ***** //

```

### B.3 fvSolution

```

/*-----*- C++ -*-----*\
| ===== |
| \\ / Field | OpenFOAM: The Open Source CFD Toolbox |
| \\ / Operation | Version: 4.1 |
| \\ / And | Web: www.OpenFOAM.org |
| \\ / Manipulation |
\*-----*/

```

```

FoamFile
{
    version      2.0;
    format       ascii;
    class        dictionary;
    location     "system";
    object       fvSolution;
}

```

```

// ***** //

```

```

solvers
{
    p
    {
        solver          PCG;
        tolerance       1e-06;
        relTol          0.05;
        preconditioner
        {
            preconditioner  GAMG;
            tolerance       1e-05;
            relTol          0.10;
            smoother        DICGaussSeidel;
            nPreSweeps      0;
            nPostSweeps     2;
            cacheAgglomeration true;
            nCellsInCoarsestLevel 512;
            agglomerator    faceAreaPair;
            mergeLevels     1;
        }
    }
}

```

```

    }
}

pFinal
{
    $p;
    relTol          0.00;
}

U
{
    solver          smoothSolver;
    smoother        GaussSeidel;
    tolerance       1e-05;
    relTol          0.05;
}

UFinal
{
    $U;
    relTol          0.00;
}

"(k/epsilon/omega/R/nuTilda)"
{
    solver          smoothSolver;
    smoother        GaussSeidel;
    tolerance       1e-05;
    relTol          0.00;
}
}

PISO
{
    nCorrectors     2;
    nNonOrthogonalCorrectors 1;
    pRefCell        0;
    pRefValue       0;
}

// ***** //

```

## B.4 probes

```
/*-----*- C++ -*-----*\
| ===== |
| \\ / Field | OpenFOAM: The Open Source CFD Toolbox |
| \\ / Operation | Version: 2.1.x |
| \\ / And | Web: www.OpenFOAM.org |
| \\ / Manipulation |
|-----*\
```

```
probes
{
// Where to load it from
functionObjectLibs ( "libsampling.so" );

type probes;

// Name of the directory for probe data
name probes;

// Fields to be probed
fields (
    P
    U
);

probeLocations
(
    // sampling along upstream cylinder axis (z-axis)
    ( 1.0 0.3 0.05 )
    ( 1.0 0.3 1.65 )
    ( 1.0 0.3 3.25 )
    ( 1.0 0.3 4.85 )
    ( 1.0 0.3 6.45 )
    ( 1.0 0.3 8.00 )
    ( 1.0 0.3 9.65 )
    ( 1.0 0.3 11.25 )
    ( 1.0 0.3 12.85 )
    ( 1.0 0.3 14.85 )
    ( 1.0 0.3 16.0 )

    // sampling along downstream cylinder axis (z axis)
    ( 8.0 0.3 0.05 )
    ( 8.0 0.3 1.65 )
    ( 8.0 0.3 3.25 )
    ( 8.0 0.3 4.85 )
    ( 8.0 0.3 6.45 )
    ( 8.0 0.3 8.00 )
    ( 8.0 0.3 9.65 )
    ( 8.0 0.3 11.25 )
    ( 8.0 0.3 12.85 )
    ( 8.0 0.3 14.85 )
)
```

( 8.0 0.3 16.0 )

);

}

// \*\*\*\*\* //